

# The Paton Welding Journal

05  
2022

International Scientific-Technical and Production Journal ♦ Founded in January 2000 (12 Issues Per Year)

## EDITORIAL BOARD

### Editor-in-Chief

I.V. Krivtsun E.O. Paton Electric Welding Institute, Kyiv, Ukraine

### Deputy Editor-in-Chief

S.V. Akhonin E.O. Paton Electric Welding Institute, Kyiv, Ukraine

### Deputy Editor-in-Chief

L.M. Lobanov E.O. Paton Electric Welding Institute, Kyiv, Ukraine

### Editorial Board Members

O.M. Berdnikova	E.O. Paton Electric Welding Institute, Kyiv, Ukraine
Chang Yunlong	School of Materials Science and Engineering, Shenyang University of Technology, Shenyang, China
V.V. Dmitrik	NTUU «Kharkiv Polytechnic Institute», Kharkiv, Ukraine
Dong Chunlin	China-Ukraine Institute of Welding of Guangdong Academy of Sciences, Guangzhou, China
M. Gasik	Aalto University Foundation, Finland
A. Gumenyuk	Bundesanstalt für Materialforschung und –prüfung (BAM), Berlin, Germany
V.V. Knysh	E.O. Paton Electric Welding Institute, Kyiv, Ukraine
V.M. Korzhyk	E.O. Paton Electric Welding Institute, Kyiv, Ukraine
V.V. Kvasnytskyi	NTUU «Igor Sikorsky Kyiv Polytechnic Institute», Kyiv, Ukraine
Yu.M. Lankin	E.O. Paton Electric Welding Institute, Kyiv, Ukraine
S.Yu. Maksymov	E.O. Paton Electric Welding Institute, Kyiv, Ukraine
Yupiter HP Manurung	Smart Manufacturing Research Institute, Universiti Teknologi MARA, Shah Alam, Malaysia
M.O. Pashchin	E.O. Paton Electric Welding Institute, Kyiv, Ukraine
Ya. Pilarczyk	Welding Institute, Gliwice, Poland
V.D. Poznyakov	E.O. Paton Electric Welding Institute, Kyiv, Ukraine
U. Reisgen	Welding and Joining Institute, Aachen, Germany
I.O. Ryabtsev	E.O. Paton Electric Welding Institute, Kyiv, Ukraine
V.M. Uchanin	Karpenko Physico-Mechanical Institute, Lviv, Ukraine
Yang Yongqiang	South China University of Technology, Guangzhou, China

### Managing Editor

O.T. Zelnichenko International Association «Welding», Kyiv, Ukraine

### Address of Editorial Board

E.O. Paton Electric Welding Institute, 11 Kazymyr Malevych Str. (former Bozhenko), 03150, Kyiv, Ukraine  
Tel./Fax: (38044) 205 23 90, E-mail: [journal@paton.kiev.ua](mailto:journal@paton.kiev.ua)  
<https://patonpublishinghouse.com/eng/journals/tpwj>

**State Registration Certificate** 24933-14873 ПП from 13.08.2021

ISSN 0957-798X, DOI: <http://dx.doi.org/10.37434/tpwj>

**Subscriptions**, 12 issues per year:

\$384 — annual subscription for the printed (hard copy) version, air postage and packaging included;

\$312 — annual subscription for the electronic version (sending issues in pdf format or providing access to IP addresses).

### Representative Office of «The Paton Welding Journal» in China:

China-Ukraine Institute of Welding, Guangdong Academy of Sciences  
Address: Room 210, No. 363 Changxing Road, Tianhe, Guangzhou, 510650, China.  
Zhang Yupeng, Tel: +86-20-61086791, E-mail: [patonjournal@ghi.gd.cn](mailto:patonjournal@ghi.gd.cn)

The content of the journal includes articles received from authors from around the world in the field of welding, metallurgy, material science and selectively includes translations into English of articles from the following journals, published by PWI in Ukrainian:

- Automatic Welding (<https://patonpublishinghouse.com/eng/journals/as>);
- Technical Diagnostics & Nondestructive Testing (<https://patonpublishinghouse.com/eng/journals/tdnk>);
- Electrometallurgy Today (<https://patonpublishinghouse.com/eng/journals/sem>).

# CONTENTS

## ORIGINAL ARTICLES

**O.A. Gaivoronskyi, V.D. Poznyakov, Yu.V. Demchenko, A.M. Denysenko, A.V. Zavdoveev, V.A. Kostin, T.G. Solomiychuk**  
INFLUENCE OF PULSED-ARC WELDING MODES ON THE STRUCTURE AND MECHANICAL PROPERTIES OF WELDS AND HAZ METAL OF WELDED JOINTS OF 30Kh2N2MDF STEEL\* ..... 3

**I.O. Ryabtsev, A.A. Babinets, I.P. Lentugov, I.L. Bogaychuk, A.I. Panfilov**  
ELECTRIC ARC SURFACING OF WEAR-RESISTANT IRON- AND NICKEL-BASED ALLOYS ON COPPER\* ..... 10

**V.M. Korzhyk, V.Yu. Khaskin, S.I. Peleshenko, A.A. Grynyuk, Dong Chunlin, E.V. Illyashenko, Yuhui Yao**  
SELECTION OF PARAMETERS OF LASER WELDING OF THIN-WALLED ITEMS FROM LIGHT ALLOYS WITH NONTHROUGH THICKNESS PENETRATION\* ..... 16

**S.V. Akhonin, V.Yu. Bilous, R.V. Selin, I.K. Petrychenko, L.M. Radchenko, S.B. Rukhanskyi**  
ARGON-ARC WELDING OF HIGH-TEMPERATURE TITANIUM ALLOY DOPED BY SILICON\* ..... 26

**S.V. Maksymova, P.V. Kovalchuk, V.V. Voronov**  
FEATURES OF THE STRUCTURE OF MOLYBDENUM–COVAR BRAZED JOINTS\* ..... 33

**I.V. Protokovilov, V.O. Shapovalov, V.B. Porokhonko, S.G. Hrygorenko**  
STRUCTURE AND PROPERTIES OF ELECTROSLAG WELDED JOINTS OF VT6 TITANIUM ALLOY\*\* ..... 40

**V.M. Uchanin**  
STUDY OF EDDY CURRENT FLAW DETECTOR BASED ON DOUBLE-CIRCUIT SELF-GENERATOR OPERATED IN INTERMITTENT OSCILLATING MODE\*\*\* ..... 46

\*Translated Article(s) from «Automatic Welding», No. 5, 2022.

\*\*Translated Article(s) from «Electrometallurgy Today», No. 2, 2022.

\*\*\*Translated Article(s) from «Technical Diagnostics & Nondestructive Testing», No. 2, 2022.

# INFLUENCE OF PULSED-ARC WELDING MODES ON THE STRUCTURE AND MECHANICAL PROPERTIES OF WELDS AND HAZ METAL OF WELDED JOINTS OF 30Kh2N2MDF STEEL

**O.A. Gaivoronskyi, V.D. Poznyakov, Yu.V. Demchenko, A.M. Denysenko, A.V. Zavdoveev, V.A. Kostin, T.G. Solomiychuk**

E.O. Paton Electric Welding Institute of the NASU  
11 Kazymyr Malevych Str., 03150, Kyiv, Ukraine

## ABSTRACT

The technological concept of welding high-strength steels with the yield strength over 1200 MPa is proposed and scientifically substantiated, which consists in combination of pulsed-arc MIG welding and application of a high-alloy wire of Cr–Ni–Mn alloying system. The structured information on the peculiarities of the thermal cycle and its influence on the structural transformations in HAZ and weld metal was obtained. The notion of the course of physical and metallurgical welding processes depending on basic parameters of standard and forced welding modes was developed. Their positive effect on mechanical properties of welded joints was established.

**KEYWORDS:** pulsed-arc welding, high-strength steels, properties, structure, heat-affected zone, austenitic welding material

## INTRODUCTION

Recently, to implement projects on light armored tanks (LAT) of a new generation, modern heat-strengthened armored steels of high strength and hardness with a yield limit of over 1200 MPa are used. These are widely known domestic steel of 30Kh2NMDF grade [1] and steels of foreign production ARMSTAL 500, Mii-lux Protection 500, HB 500 MOD, RAMOR 500 and ARMOX 500S. To provide service properties, sheet rolled metal of mentioned steels of 6–20 mm thickness is hardened with the following low tempering. In the final heat-treated state in the structure of steel, tempering martensite is formed, due to which high values of static and dynamic strength are achieved, as well as high service characteristics. However, due to various reasons, technological properties are unsatisfactory for the successful use of high-performance processes associated with repeated heating, such as welding, surfacing, etc. A limited weldability is caused by both initial condition as well as high carbon content (> 0.3 %). Namely, the main problem of stationary arc welding (SAW) of armored steels is the change in the properties of metal in the heat-affected zone (HAZ) of welded joints [2]. The most significant changes occur both on the overheating area as well as on the area of HAZ tempering. Structural and phase transformations on the overheating area are characterized by an increase in the size of austenitic grain and development of a high-temperature chemical microheterogeneity and by lamellar martensite formation during the further cooling. This results in an increased risk of cold

crack formation under the action of residual welding stresses. In turn, structural and phase transformations in the area of HAZ tempering do not have significant changes in morphology and grain sizes but lead to softening, which is caused by a whole number of factors, such as annihilation of dislocations, growth or dissolution of carbides, etc. [3, 4].

Another cause for the deteriorated weldability of armored steels is the formation of a brittle martensite interlayer or carbide ridge in the area of fusion, where the level of alloying is reduced to the level of the base metal [5].

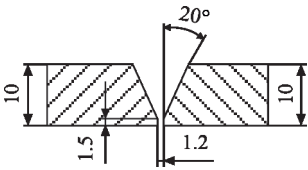
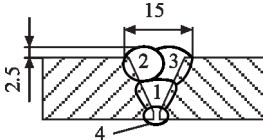
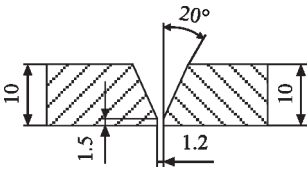
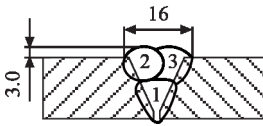
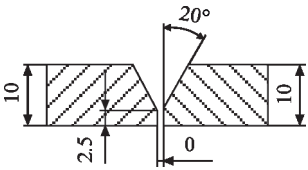
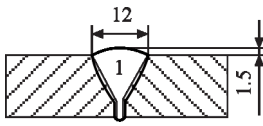
The mentioned features of formation of structure and properties of welded joints require performing welding in reduced modes, which leads to a decrease in the efficiency of manufacturing LAT products. This motivates a search for new welding technologies that will ensure a high efficiency and quality of products.

To solve this problem, we propose the following technological concept, which consists in applying the modern high-efficiency process of pulsed-arc welding (PAW).

The PAW process is qualitatively different from the traditional SAW in shielding gases. This is explained by the fact that in PAW the abilities to control the thermal cycle of welding and the processes of melting and electrode metal transfer in different spatial positions are expanded [6].

Since welding is characterized by physical and metallurgical processes that combine the concepts and a whole range of complex phenomena occurring

**Table 1.** Welded joint of 30Kh2N2MDF steel for investigations

Specimen number	Structural elements of preparation (mm, deg)	Welded joint
No. 1 Stationary process		
No. 2 PAW on a standard mode		
No. 3 PAW on a forced mode		

in molten metal and HAZ metal under the action of thermal cycle of welding (TCW), then the main factor that affects the entire course of the process is TCW [7–11]. It is characterized by such parameters as maximum temperature, heating and cooling rates, duration of metal staying above the specified temperatures at which heating occurs, melting of base metal and filler metal, formation of welding pool and metal of weld and HAZ, subsequent cooling and solidification as well as structural condition in different zones of welded joint is formed, technological strength (resistance to cold and hot crack formation), and physical and mechanical properties (strength, hardness, ductility, toughness, etc.) are provided. It is possible to control TCW by changing PAW modes, namely the main components: current and voltage of welding, frequency and duty cycle, welding speed.

In view of the abovementioned, in the work for the first time the study of the effect of PAW modes in MIG welding of the austenitic material on the structure of the weld and HAZ metal and the mechanical properties of the deposited metal of welded joints of steel 30Kh2N2MDF was performed.

**PROCEDURE OF EXPERIMENT**

To determine the effect of PAW modes on the structure, the mechanical properties of welded joints of

armored steels of high hardness, the domestic armored steel of 30Kh2N2MDF grade of the following chemical composition was used, wt.%: 0.30 C, 1.1 Si, 0.73 Mn, 1.67 Cr, 2.28 Ni, 0.26 Mo, 0.21 V. In a hardened state (normalization and cooling in water) after a low-temperature tempering at 230 °C, the armored steel has ultimate strength and hardness at the level of 1500 and 5000 MPa respectively.

Considering that in the EWM Phoenix 501 plus power source during operation in a pulsed mode, welding parameters, namely, pulsed current  $I_{\text{pulse}}$ , pause current  $I_{\text{pause}}$ , frequency  $f$  and duty cycle  $\delta$  are programmed by the manufacturer, to determine their impact on the structure and mechanical properties of the joints of steel of 30Kh2N2MDF grade in the selected welding modes, the average welding current ( $I_{\text{av}}$ ) was used [12, 13]. To do that, welding of butt joints of the specimens of 71 steel of 10 mm thickness was performed. The dimensions of the structural elements of preparations of the specimens Nos 1–3 and welded joints are given in Table 1, and the modes of their welding are in Table 2. The welding of the specimens was performed by the wire of HORDA 307 grade (alloying system 08Kh20N9G7T) in the shielding mixture of gases 82 % Ar + 18 % CO<sub>2</sub>. The electrode wire stickout in all cases was  $L_s = 15$  mm. The general

**Table 2.** Method and modes of welding joints of 30Kh2N2MDF steel when performing investigations

Specimen number	Method of welding	Welding mode				Input energy, kJ/cm
		$I_{\text{av}}$ , A	$U_{\text{a}}$ , V	$v_{\text{w}}$ , m/h	$V_{\text{f}}$ , m/min	
1*	Stationary process — mechanized arc welding	180	24–26	18–21	5.6	7.5–6.4
2**	PAW on a standard mode	180	27	18–21	6.6	7.8–6.7
3**	PAW on a forced mode	300	29.4	24	10.4	10.6

Note. \*Backup welding from the back surface of the specimen. \*\*Without backup welding.



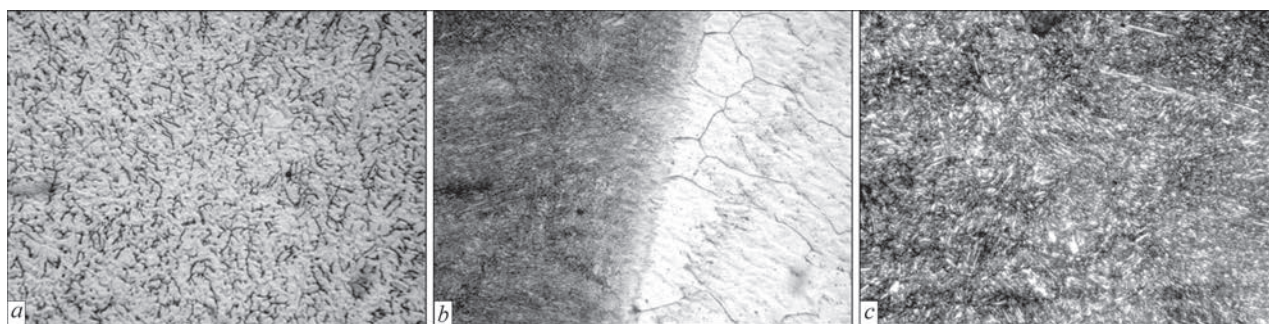


**Figure 1.** Microstructure ( $\times 500$ ) of joint of 30Kh2N2MDF steel in mechanized welding on a stationary mode: *a* — weld; *b* — fusion line; *c* — coarse grain HAZ area

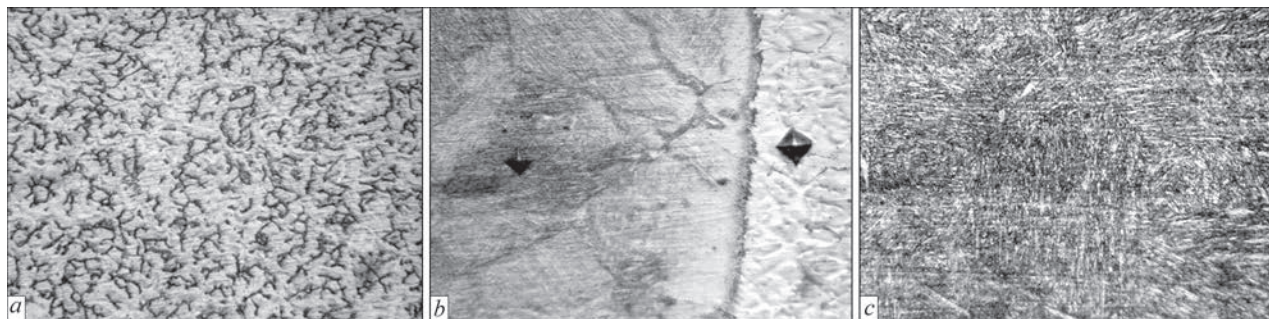


**Figure 2.** Microstructure ( $\times 500$ ) of joint of 30Kh2N2MDF steel in PAW on a standard mode: *a* — weld; *b* — fusion line; *c* — coarse grain HAZ area

appearance of the specimens of steel 30Kh2N2MDF after PAW is shown in Figures 1 and 2.

The structure of welded joints was investigated by standard methods of optical metallography. Figures 3–5 show a typical microstructure of the weld metal, the fusion zone and areas of coarse grain of HAZ of welded joints of steel of 30Kh2N2MDF grade, produced by different methods of welding.

## RESULTS AND DISCUSSION

It was found that the structure of deposited metal of welds of the specimens made by mechanized welding and PAW on a standard mode is austenitic with the microhardness ( $HV_{0.1}$ ) 2540 and 2920 MPa respectively (Figure 1, *a*, Figure 2, *a* and Figure 4, *a*). The content of  $\delta$ -ferrite in the deposited metal decreases from the weld root to the surface from 4 to 0.6 %. Microstructure of the weld metal of the specimen made by PAW on a forced mode (specimen No. 3) is signifi-

cantly different from the microstructure of the metal of welds of the specimens Nos 1 and 2, namely, near austenite, martensite with a specific fraction of up to 19 % (Figure 3, *a*) appeared. This composite structure was obtained by mixing the weld metal with the base metal due to the effect of Marangoni convection [7]. This provided an increase in microhardness of the weld metal to ( $HV_{0.1}$ ) 3450–4010 MPa. Along the fusion line, the areas of martensite are also observed (Figure 3, *b*, Figure 4, *b*).

The structure of the HAZ coarse grain area of the joint made by mechanized welding on a stationary mode (No. 1) consists of a mixture of lower bainite and martensite with the hardness ( $HV_{0.1}$ ) 4100 MPa. During the transition to the pulsed mode (specimen No. 2), a mixture of bainite and martensite is also observed, but with a lower hardness value ( $HV_{0.1}$ ) 4000 MPa). It is necessary to note that along the fusion line of the specimen No. 2, sometimes light pre-



**Figure 3.** Microstructure ( $\times 500$ ) of joint of 30Kh2N2MDF steel in PAW on a forced mode: *a* — weld; *b* — fusion line; *c* — coarse grain HAZ area

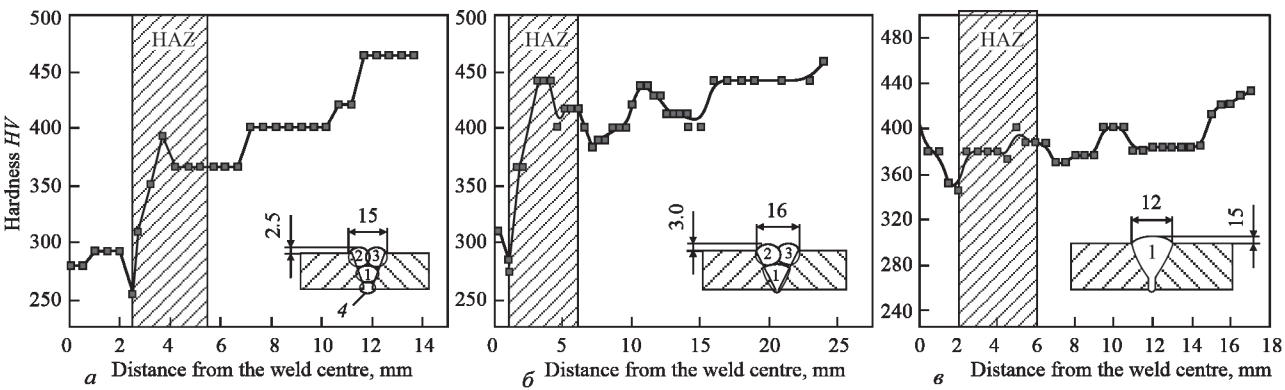


**Figure 4.** Distribution of hardness in the metal of welded joints of 30Kh2N2MDF steel: *a* — stationary mode; *b* — PAW on a standard mode; *c* — PAW on a forced mode

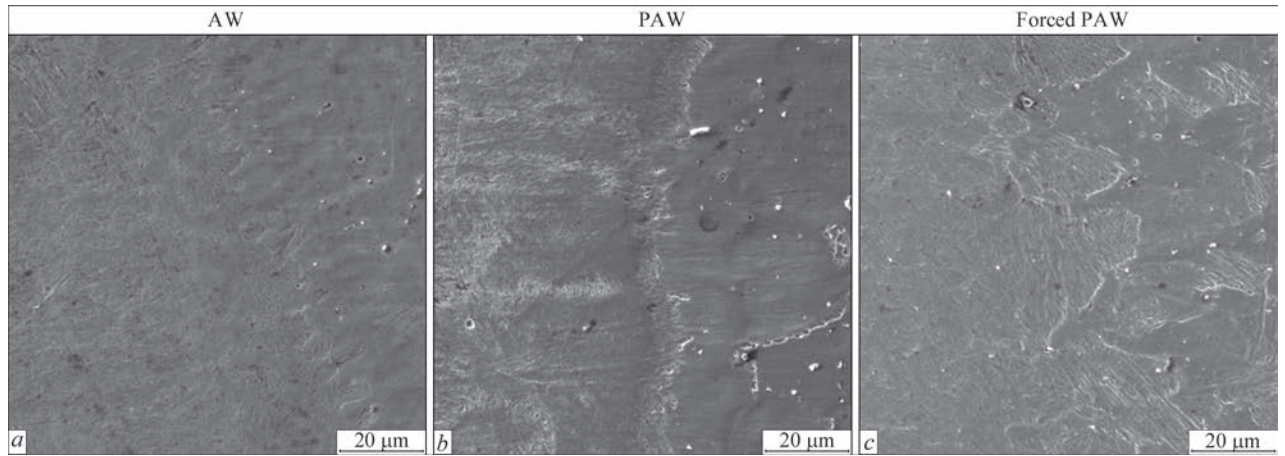


**Figure 5.** Microstructure of the fusion line in the area in the lower part of welded joint

precipitations can be seen, probably of the carbide phase. When moving from the area of HAZ coarse grain (specimen No. 2), the specific fraction of lower bainite increases, as a result of which, the hardness of this zone increases to 4420 MPa.

For the specimen produced on a forced mode in the metal of the HAZ coarse and fine grain area (No. 3), the structure of the mixture of bainite and martensite with the microhardness of components in the range of 3660–3800 MPa (Figure 4, *c*) is also observed. It should be noted that the base metal has a hardened martensitic structure with a microhardness of martensite of 4590–4640 MPa.

According to the changes in the structure, the mechanical properties of the deposited metal of welded joints, which were determined during tests at static tension and impact of standard specimens, respectively according to GOST 6996–66 and GOST 9454–78,

**Table 3.** Mechanical properties of deposited weld metal of welded joints of 30Kh2N2MDF steel

Specimen number	$\sigma_t$ , MPa	$\sigma_{0.2}$ , MPa	$\delta_5$ , %	$\psi$ , %	KCU, J/cm <sup>2</sup>	
					20 °C	–40 °C
1	631	354	39	43	112	78
2	642	362	30	44	105	62
3	913	340	23	30	66	56

are also changed in the structure. The generalized test results are given in Table 3.

Since special attention in our studies is attracted by the structure formed on the fusion line, which subsequently determines the structurally independent mechanical properties of the whole welded joint, to perform a detailed study, the capabilities of optical microscopy with  $\times 1000$  resolution are not sufficient. In this regard, scanning microscopy was additionally used. For the analysis, three areas on the fusion line were selected: in the lower, middle and upper part of the welded joint. For element analysis, a linear scanning of 1 mm length perpendicular to the fusion line was performed. This allowed analyzing the distribution of chemical elements of the main alloying system, namely Cr, Ni, Mn and revealing the features of their redistribution between the weld and the base metal.

While studying fusion line at a high resolution capacity (at magnifications  $\times 2000$ , Figures 5–7), it was revealed that in stationary arc welding, a toothed morphology of the shore on the interface austenitic weld — base metal is formed.

In the weld root, during PAW a smooth transition from austenitic material to alloyed one is formed. And on a forced mode of PAW, the morphology changes



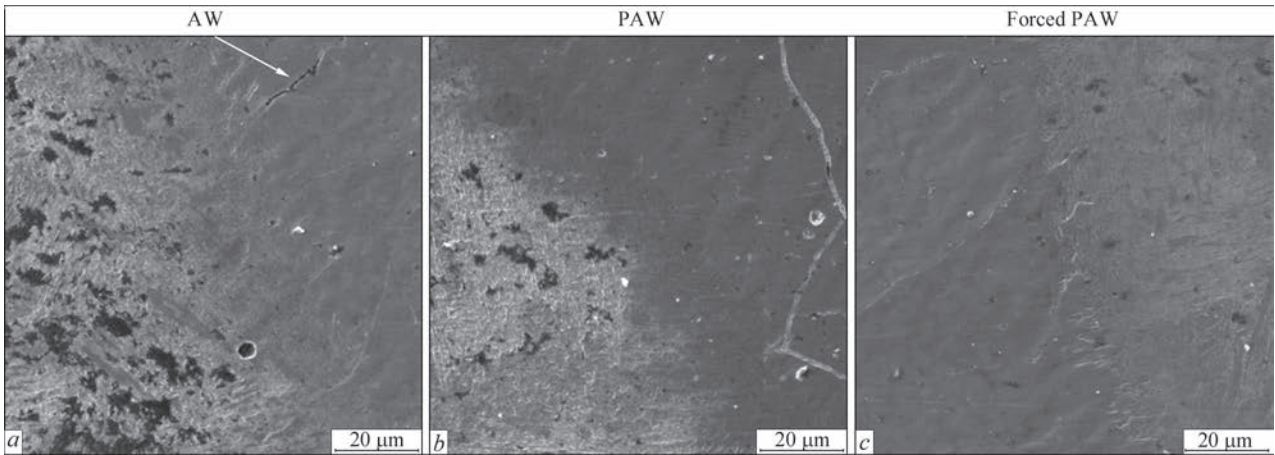


**Figure 6.** Microstructure of fusion line in the area in the middle part of welded joint

radically, a qualitative mixing of austenitic and base metal with the formation of mixed austenitic-martensitic structure is observed. In the middle of the weld, for PAW and a forced mode, the situation is the same as in the root, and for AW, the morphology of the shores changes, namely, a wide area of the martensitic-bainitic structure appears, and on the side of the austenitic weld, a discontinuity with a length of about 15  $\mu\text{m}$  appears, which can potentially be the nucleus of a cold crack. In the upper part of the weld at the fusion line, a smooth transition from one to another material is also observed for PAW and a forced mode, and for AW an area with pronounced carbide inclusions is present.

All the mentioned changes in the structure and chemical inhomogeneities of the blocks and grains, caused by the change in the cooling rate, exert a significant influence on the properties of the weld metal in general, including such indices as impact toughness, etc. As a rule, the fracture of metals, including brittle one, occurs only after a certain amount of plastic deformation. When encountering an obstacle in the sliding plane, for example, slag inclusions, block boundary, boundary intersection of three grains, a series of  $n$ -dislocations of the same sign is formed,

which exerts a pressure on this obstacle that is  $n$ -times higher than the applied stress. This growing stress concentration can lead to one of two consequences: the further propagation of a shear into the neighboring grain or the formation of a microcrack, which is in a good agreement with the results of microscopic analysis obtained in the work.

The analysis of the redistribution of chemical elements along the fusion line made it possible to find that on a forced mode of PAW, an active mass transfer is observed, caused by mixing in the transition zone austenitic weld-base metal, which, as was mentioned earlier, is predetermined by the Marangoni effect.

The change in the content of the alloying element in the fusion zone of these dissimilar materials depends on the method of welding and the heat input of welding. The type of fusion of dissimilar steels depends on the welding mode. Its change causes a redistribution of the elements included in the composition of the welded metal, especially those, having a high diffusion coefficient. In the modes that increase the time when the fusion zone of the welded metal stays in the region of high temperatures, diffusion processes intensify in it, as a result of which an accumulation of elements occur, that form easily melting or brittle

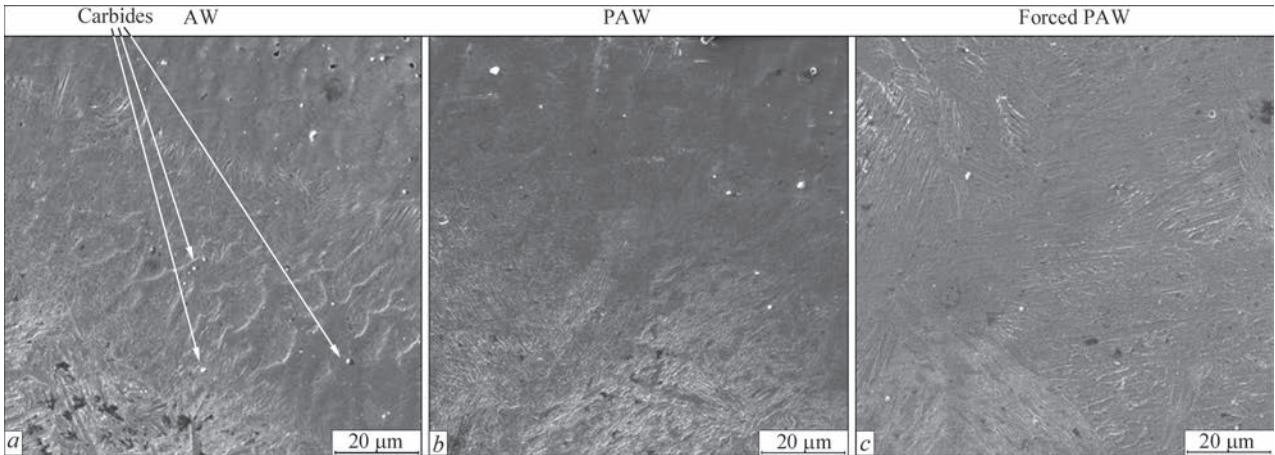


**Figure 7.** Microstructure of fusion line in the area in the upper part of welded joint

compounds at the grain boundaries. The presence of such compounds at the grain boundaries leads to the formation of an alloy from wedging of the deposited metal into the base one in the form of islands/peninsulas. This wedging is repeated so often that the fusion zone acquires the appearance of a fringe. Microscopic studies also confirm that in this case the fusion boundary acquires a wavy shape.

Fusion of dissimilar steels with wedging of the weld metal into the base metal can also occur in this case, if the latter has a chemical composition, at which interlayers are formed between the grains prone to embrittlement. The stresses arising during welding cause cracks in these interlayers, into which the liquid metal of the welding pool penetrates during further formation of the welded joint, and in the case when the metal does not flow into, they are the nucleus of cold cracks.

It can be assumed that the formation of islands and peninsulas in the fusion zone is determined by the conditions of mixing the liquid metal of the welding pool in a thin layer directly adjacent to the fusion boundary. The islands and peninsulas are formed if the liquid metal, for some reason, is not sufficiently mixed. This is evidenced by the fact that the fusion border of the base and deposited metal directly near the islands has a zigzag shape, where the «teeth» of the base metal, penetrating into the fused metal, lose the sharpness of their contours as they blur. In the case of good mixing, the borders acquire clear outlines. A number of islands observed in the fusion zone, as well as the probability of their appearance, depend on the mode and method of welding.

As we can see, at the transition from stationary arc welding to a pulsed mode and an increase in the current to 300 A lead to an increase in the yield limit of the deposited metal by up to 30 %, while maintaining a sufficiently high level of plastic and impact toughness characteristics at low temperatures. Such effect can be explained by more intense mixing of electrode and base metals in the welding pool and a specific form of «keyhole» penetration in pulsed-arc welding on forced modes (effect of Marangoni convection).

The microstructure of the weld metal of the specimens produced in the stationary and pulsed modes (Nos 1, 2) is austenitic with a hardness of ( $HV_{0.1}$ ) 254 and ( $HV_{0.1}$ ) 292 MPa, respectively. The content of  $\delta$ -ferrite decreases from the weld root to the surface from 4 to 0.6 %. The microstructure of the weld metal of the specimen produced on a forced mode (No. 3) is significantly different from the microstructure of the weld metal of the specimens No. 1 and 2, namely, in the structure of the weld metal of the specimen No. 3, near austenite, martensite appeared with a spe-

cific fraction of up to 19 %. This composite structure was obtained due to mixing of the weld metal with the base metal provided by the effect of Marangoni convection. This allowed increasing the hardness of the weld metal to ( $HV_{0.1}$ ) 345–401 MPa. Along the fusion line, areas of martensite are also observed.

Thus, it was shown that applying pulsed-arc welding on a forced mode, it is possible to obtain a composite austenitic-martensitic structure of the weld metal, a minimum scattering of hardness values in the HAZ metal and during transition to the base metal, which provides a significant improvement in the mechanical properties of the welded joint as a whole.

## CONCLUSIONS

The impact of pulsed-arc welding modes on the structure, mechanical properties of welded joints of high hardness armored steels, and on their resistance to the formation of cold and hot cracks was studied. The following was established.

1. During pulsed-arc welding in stationary mode (average current is 180 A) using a high-alloy wire of the alloying system 08Kh20N9G7T, the structure of the deposited metal, as compared to conventional mechanized welding, almost does not change and remains austenitic with a microhardness of up to ( $HV_{0.1}$ ) 2920 MPa. The content of  $\delta$ -ferrite in the deposited metal decreases from the weld root to the surface from 4 to 0.6 %.

2. In pulsed-arc welding on a forced mode (average current is 300 A), in the deposited metal significant changes occur, namely, in the austenite structure martensite areas are formed, their total specific fraction is up to 19 %. This promotes an increase in the microhardness of the deposited metal to ( $HV_{0.1}$ ) 3450–4010 MPa. This composite structure was obtained due to intensive mixing of the weld metal with the base metal due to the effect of Marangoni convection. In the near-weld metal of the HAZ joints on this welding mode, the microhardness decreases from 4100 to 3800 MPa.

3. In accordance with changes in the structure, the mechanical properties of the deposited metal of welded joints of armored steels also change. In pulsed-arc welding on a forced mode, the tensile strength of the deposited metal increases to 30 % while maintaining a sufficiently high level of plastic and impact toughness characteristics.

## REFERENCES

1. TU U 27.1-14313056-001–2009: *Steel sheets of special purpose of steel grade 71 and 72. Specifications* [in Russian].
2. Poznyakov, V.D., Gaivoronskyi, A.A., Kostin, V.A. (2017) Peculiarities of austenite transformation and mechanical properties of metal in heat-affected zone of joints of steel



- grade 71 in arc welding. *Mekhanika ta Mashynobuduvannia*, **1**, 254–260 [in Russian].
3. Efimenko, M.G., Radzivilova, N.O. (2003) *Physical metallurgy and heat treatment of welded joints*. Kharkivska Drukarnia [in Ukrainian].
  4. Grabin, V.F., Denisenko, A.V. (1978) *Physical metallurgy of welding of low- and medium-alloy steels*. Kyiv, Naukova Dumka [in Russian].
  5. Gotalsky, Yu.N. (1982) *Welding of pearlite steels by austenitic materials*. Kyiv, Naukova Dumka [in Russian].
  6. Zhernosekov, A.M., Andreev, V.V. (2007) Pulsed metal arc welding (Review). *The Paton Welding J.*, **10**, 40–43.
  7. Kovalenko, D.V., Krivtsun, I.V., Demchenko, V.F., Kovalenko, I.V. (2010) Peculiarities of thermal and hydrodynamic processes occurring in TIG and A-TIG welding of stainless steel. *The Paton Welding J.*, **12**, 2–5.
  8. Gaivoronskyi, A.A., Poznyakov, V.D., Klapatyuk, A.V. et al. (2012) Formation of cold cracks in welded joints of armoured steels of high strength and hardness of domestic and foreign production. *Mekhanika ta Mashynobuduvannia*, **1**, 221–227 [in Russian].
  9. Papsheva, N.D., Mladentseva, O.A., Baranov, S.A. (2017) Application of preliminary and concurrent heating to improve the characteristics of welded joint. *Vysokie Tekhnologii v Mashinostroenii*, 30–32 [in Russian].
  10. Gaivoronskyi, A.A. (2014) Resistance to cold crack formation of HAZ metal of welded joints on high-strength carbon steels. *The Paton Welding J.*, **2**, 2–11.
  11. OSTV3-15.010-85. *The procedure for the introduction of new welding materials and technological processes of arc welding in the mass production of armored steel bulletproof structures for military tracked and wheeled vehicles*.
  12. Poznyakov, V.D., Zavidoveev, A.V., Gaivoronsky, O.A. et al. (2018) Effect of pulsed-arc welding modes on the change of weld metal and HAZ parameters of welded joints produced with Sv-08Kh20N9G7T wire. *The Paton Welding J.*, **9**, 7–12.
  13. Zavidoveev, A.V., Poznyakov, V.D., Gaivoronskyi, O.A. et al. (2021) Optimization by calculation method of pulsed-arc welding modes using high alloy welding material. *The Paton Welding J.*, **4**, 9–13. DOI: <https://doi.org/10.37434/tpwj2021.04.02>

#### ORCID

O.A. Gaivoronskyi: 0000-0002-5922-5541,  
V.D. Poznyakov: 0000-0001-8581-3526,  
A.V. Zavidoveev: 0000-0003-2811-0765,  
V.A. Kostin: 0000-0002-2677-4667,  
T.G. Solomiychuk: 0000-0002-3038-8291

#### CONFLICT OF INTEREST

The Authors declare no conflict of interest

#### CORRESPONDING AUTHOR

A.V. Zavidoveev  
E.O. Paton Electric Welding Institute of the NASU  
11 Kazymyr Malevych Str., 03150, Kyiv, Ukraine.  
E-mail: avzavidoveev@gmail.com

#### SUGGESTED CITATION

O.A. Gaivoronskyi, V.D. Poznyakov,  
Yu.V. Demchenko, A.M. Denysenko,  
A.V. Zavidoveev, V.A. Kostin,  
T.G. Solomiychuk (2022) Influence of pulsed-arc  
welding modes on the structure and mechanical  
properties of welds and HAZ metal of welded joints  
of 30Kh2N2MDF steel. *The Paton Welding J.*, **5**,  
3–9.

#### JOURNAL HOME PAGE

<https://pwj.com.ua/en>

Received: 24.02.2022

Accepted: 08.08.2022

<https://doi.org/10.37434/tpwj2022.05.02>

# ELECTRIC ARC SURFACING OF WEAR-RESISTANT IRON- AND NICKEL-BASED ALLOYS ON COPPER

**I.O. Ryabtsev<sup>1</sup>, A.A. Babinets<sup>1</sup>, I.P. Lentugov<sup>1</sup>, I.L. Bogaychuk<sup>1</sup>, A.I. Panfilov<sup>2</sup>**

<sup>1</sup>E.O. Paton Electric Welding Institute of the NASU  
11 Kazymyr Malevych Str., 03150, Kyiv, Ukraine  
<sup>2</sup>WSC «Steel Work»  
50 Myru Prosp., 50000, Kryvyi Rih, Ukraine

## ABSTRACT

The results of studying the formation of welded joint in electric arc surfacing on copper by the wires, providing a deposited metal based on iron and nickel, which according to the authors and publications in the technical literature, have a high resistance to different types of wear at elevated temperatures. The modes were selected and technologies of arc surfacing on a copper base by selected wires were developed, which provide a satisfactory formation of the deposited metal and its fusion with the base metal. According to the results of experiments on electric arc surfacing on copper, as well as the study of macro- and microstructure of deposited specimens, it was shown that the best results in terms of welding and technological properties are provided by the use of the nickel-based wire. The admissibility of individual defects that were found in the deposited metal and on the fusion line of the base and deposited metals during studies will be determined by the operating conditions of specific parts.

**KEYWORDS:** surfacing on copper, wear-resistant alloys, electric arc surfacing, copper, weldability, fusion zone

## INTRODUCTION

Copper, having a high electrical and thermal conductivity, ductility and corrosion stability, is widely used in various industries in manufacture of molds, tuyeres, heat exchangers, pipelines, parts of chemical equipment, cable and electric contact products, etc. [1].

At the same time, a low wear resistance and heat resistance of copper leads to the fact that some copper parts, in particular, molds, tuyeres and other parts, which are operated in contact with molten metal, high-temperature gas flows and abrasives of different hardness, quickly come out of order and require replacement.

One of the possible ways of improving service properties of copper parts can be surfacing of layers with high wear resistant properties on their worn out surfaces.

However, during surfacing of wear resistant alloys of various systems of alloying on copper, in particular, based on iron and nickel, large difficulties arise due to the fact that the latter have a higher melting point and much lower electrical and thermal conductivity, as well as the coefficient of thermal expansion (CTE) than copper (Table).

The abovementioned differences in thermophysical properties can affect the weldability of iron- and nickel-based alloys with copper:

- high thermal conductivity of copper leads to high cooling rates and the need in using sources of welding heating with a high heat input or the use of preliminary and accompanying heating of copper parts, and sometimes both;
- a relatively low melting point of copper, which in arc surfacing of iron- and nickel-based alloys on copper can lead to a significant penetration of a copper base;
- a short time of welding pool staying in a liquid state due to a high thermal conductivity of copper limits the possibilities of its metallurgical treatment and requires the use of active deoxidizers;
- a high CTE of copper, which in surfacing of wear-resistant steels and alloys on copper parts can lead to high residual stresses and large deformations;
- high fluidity of copper, which in some cases can deteriorate the formation of deposited metal;
- light oxidability of copper in a molten state, which leads to the formation of low-melting eutectics, which reduce the resistance of copper to the formation of crystallization cracks [3].

Thermophysical properties of copper, iron and nickel [2]

Index	Copper	Iron	Nickel
Atomic mass	63.54	55.85	58.69
Melting point, °C	1083	1535	1453
CTE at 1 °C, 10 <sup>-6</sup>	17.06	12.15	13.6
Thermal conductivity, W/(m·K)	413	94	107
Specific heat capacity, J/(kg·K)	385	449	500
Specific resistance, Ohm·m, ·10 <sup>-8</sup>	1.68	10.0	6.99
Density, kg/m <sup>3</sup>	8930	7850	8900

Among these problems, arising in surfacing of wear-resistant iron- and nickel-based alloys on copper, the main ones are the lower melting point of copper and its higher thermal conductivity (see Table). As a result, during surfacing on copper, the welding pool quickly loses heat, which leads to a sharp decrease in its fluidity and, as a result, to a poor formation of deposited beads or even to the absence of their formation and fusion with the base metal.

Moreover, due to a high rate of crystallization of the welding pool, in the deposited metal the inclusions of copper may occur, which can reduce its service properties [3].

**Aim of the research:** Based on the abovementioned facts and available practical experience, to develop the technologies of electric arc surfacing of iron- and nickel-based layers, having high wear resistant properties at different types of wear at elevated temperatures, on a copper base.

## **MATERIALS AND PROCEDURES FOR CONDUCTING EXPERIMENTS ON ELECTRIC ARC SURFACING ON A COPPER BASE**

Experiments on electric arc surfacing on a copper base by the wires that provide producing the deposited metal based on iron or nickel, having high wear resistant properties at elevated temperatures [4].

The wires of these types were selected for research based on the following considerations and with taking into account the requirements for the abovementioned service properties of copper parts [4–6]:

- semi-heat- and heat-resistant steels, complex-alloyed with chromium, molybdenum, nickel, etc.;
- high-chromium cast iron (alloys of the type sormite);
- nickel-based alloys.

The flux-cored wires, providing producing of the deposited metal of the type of semi-heat- and heat-resistant steels of the alloying system Fe–C–Cr–Mo–V are widely used to strengthen the parts of metallurgical equipment, operating in the conditions of cyclic heat changes, high dynamic loads in combination with friction of metal against metal without or with the abrasive interlayer. Steels with a high content of tungsten have the highest hardness and heat resistance at high temperatures, however, thermal stability and impact toughness of such steels is relatively low [4]. Replacement of tungsten by molybdenum (full or partial) reduces the heat resistance of steel, but significantly increases its thermal stability. In surfacing, the steels of this class are prone to crack formation, for this reason, surfacing is conducted with a preliminary and sometimes with an accompanying heating. Hereinafter in the article, the flux-cored wire of this

type used in the investigations, for brevity is called the wire No. 1.

The flux-cored wires or strips that provide producing the deposited metal of the type of high-chromium cast iron with carbon and chromium content of up to 5 and 30 %, respectively, are used for surfacing parts, operating in intensive abrasive or gas-abrasive wear at high temperatures (up to 1000 °C). For surfacing of these materials, different methods can be used, but surfacing technology is associated with considerable difficulties because of their high tendency to crack formation [4]. Further, the flux-cored wire of this type for brevity is called the wire No. 2.

The wires that provide producing the deposited metal on a nickel base, have high heat resistance, good resistance to thermal fatigue, high resistance to different types of corrosion and little prone to crack formation in surfacing. One of the most common grades of alloys of this type is the alloys of the Inconel alloying systems of the type Ni–Cr–Mo–Nb [4]. According to numerous studies [5–8, etc.], the use of nickel-based materials allows producing metal with better indices on weldability, corrosion and wear resistance. Further, the flux-cored wire of this type for brevity is called the wire No. 3.

With the use of the wires that provide producing the deposited metal of the types mentioned above, the experiments on practicing the technology and technique of arc surfacing on plane billets of M1 copper with the sizes (8–10)×100×100 mm were carried out.

Satisfactory results in electric arc surfacing on copper plates by the flux-cored wire No. 1 of 1.6 mm diameter under the flux AN-26P, which provides producing the deposited metal of the type of semi-heat-resistant tool steel 25Kh5FMS were achieved on the following modes: current — 280–300 A; voltage — 28–30 V; deposition rate — 15 m/h; bead overlapping — 15–20 %. However, the external inspection indicated that in surfacing on the mentioned modes, beads are produced very narrow. An increase in voltage to 32 V significantly improved the formation of deposited beads.

In arc surfacing on a copper plate by the self-shielding flux-cored wire No. 2 of 1.6 mm diameter, which provides producing the deposited metal of the type of high-chromium cast iron 400Kh25GSM, the following mode was selected, in which the process of surfacing was satisfactory, and the formation was quite well — 200–250 A, voltage — 24–26 V, deposition rate — 12–18 m/h; bead overlapping — 45–50 %.

The experiments were carried out on arc surfacing on copper in inert gas by the solid wire No. 3 of 1.6 mm diameter which provides producing the deposited metal of the type Inconel N65Kh25M11B4.



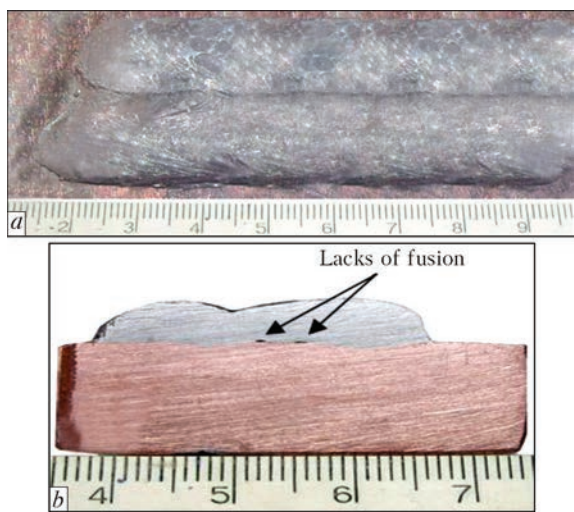


**Figure 1.** Appearance of beads deposited on the specimen of M1 copper by the flux-cored wire No. 1 (type of deposited metal 25Kh5FMS) (a) and macrosection of their cross-section (b)



**Figure 2.** Microstructure ( $\times 200$ ) of copper used as a base metal

Surfacing was performed by single beads without and with bead overlapping by 40–50 %. The surfacing mode, which provides a good formation of deposited beads, is the following: current — 190–200 A; voltage — 25–26 V; deposition rate — 15–18 m/h; shielding gas consumption — 15 l/min.

While practicing the technology of surfacing by three wires to prevent crack formation in deposited beads, a preliminary heating of deposited specimens was used.

### RESULTS OF EXPERIMENTS AND THEIR DISCUSSION

The appearance of the beads deposited on a copper plate by the flux-cored wire No. 1 on the abovementioned modes is shown in Figure 1, a, and the macrosection of their cross-section is in Figure 1, b. A fairly high quality of fusion of steel 25Kh5FMS with a copper base is observed, although the presence of small lacks of fusion, located along the fusion line, is noted. The hardness of the deposited metal is HRC 46–50.

The microstructure of the specimen, deposited by the flux-cored wire No. 1 was investigated. A copper base near the fusion line has a coarse-grained structure (Figure 2), the hardness of a copper base is HV1 — 822 MPa. The fusion line in the specimen has a wavy shape (Figure 3, a), along the boundaries, lacks of fusion in the base and deposited metals (Figure 3, b) and single pores with a diameter of 70–150  $\mu\text{m}$  (Figure 3, c) were detected. The hardness of the base metal (copper) at a distance  $\approx 150 \mu\text{m}$  from the fusion line is

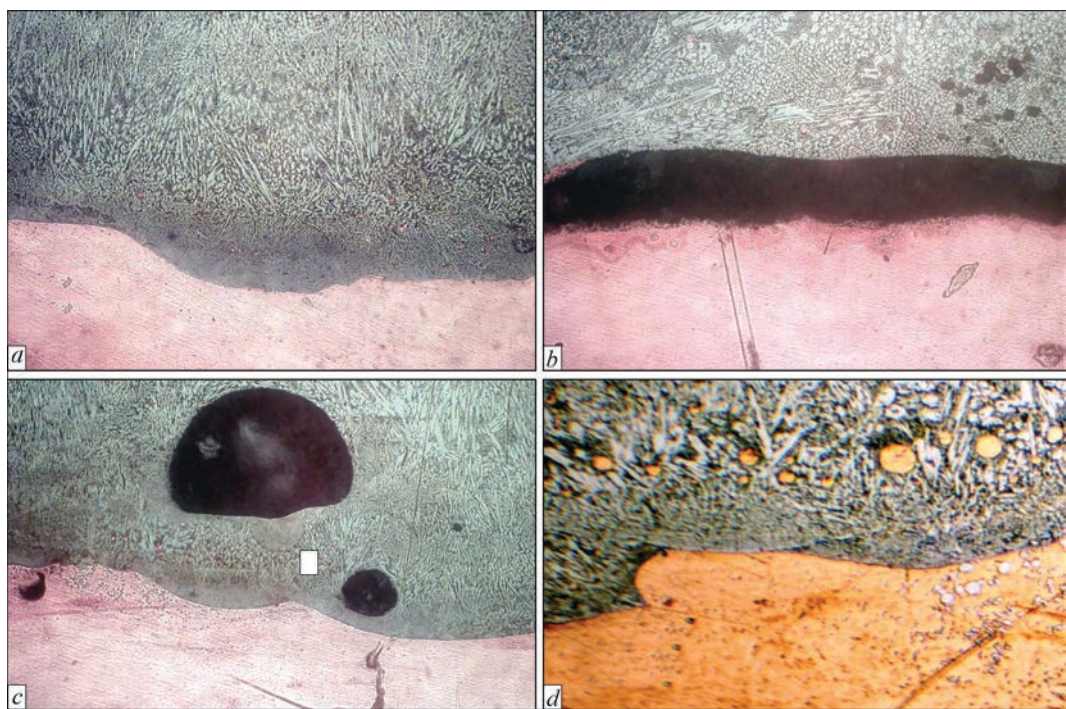


**Figure 3.** Microstructure of the fusion zone of the specimen, deposited by the flux-cored wire No. 1 (type of deposited metal 25Kh5FMS): a — in the fusion zone; b — lack of fusion area; c — pores in the fusion area; d — area of mutual diffusion steel-copper: a–c —  $\times 200$ ; e —  $\times 320$



at the level of the base metal  $HV1$  — 840 MPa, and near the fusion line it is  $HV1$  — 1050 MPa, which is caused by diffusion processes at the steel-copper interface.

In the deposited metal along the fusion line at a distance of 30–80  $\mu\text{m}$ , an area with a dispersed structure is located, which has a hardness of 5420 MPa. In the volumes of the metal adjacent to it, precipitation of carbides in the form of plates and needles with a higher hardness  $HV1$  — 6130 MPa is observed. In this area, also small inclusions of copper of a globular shape were also detected (Figure 3, *d*).

In the central part of the deposited metal, a significant coarsening of the structure occurs (Figure 4). In the solid solution based on iron, carbides of different morphology — hexagonal, laminar and lanceolate are precipitated, having a maximum size of 150  $\mu\text{m}$  and the hardness  $HV1$  — 10180–11870 MPa, as well as eutectic formations with the hardness  $HV1$  6810–7240 MPa.

The deposited metal also contains inclusions of copper of a globular shape with the hardness  $HV1$  — 1030–2540 MPa (Figure 4). In the direct vicinity of these inclusions, the hardness of deposited metal is reduced ( $HV1$  — 6060 MPa) as compared to the hardness of matrix  $HV1$  — 6810–7240 MPa.

The appearance of the copper specimen, deposited by the wire No. 2, is shown in Figure 5, *a*, and the macrosection of its cross-section is in Figure 5, *b*. A fairly high quality of fusion of the deposited metal of the type of high-chromium cast iron with a cop-

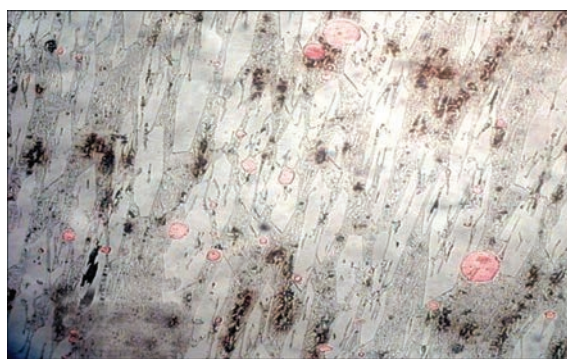


**Figure 4.** Microstructure ( $\times 200$ ) of the central part of the metal, deposited by the flux-cored wire No. 1 (type of deposited metal 25Kh5FMS)

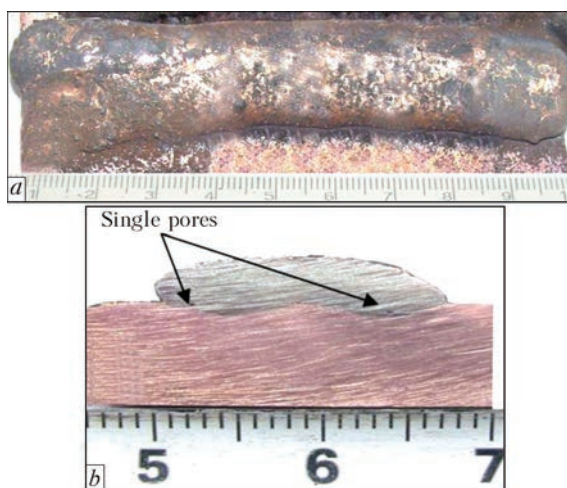


**Figure 5.** Appearance of beads, deposited on the specimen of M1 copper by the self-shielding flux-cored wire No.2 (type of deposited metal 400Kh25GSM) (*a*) and macrosection of their cross-section (*b*)

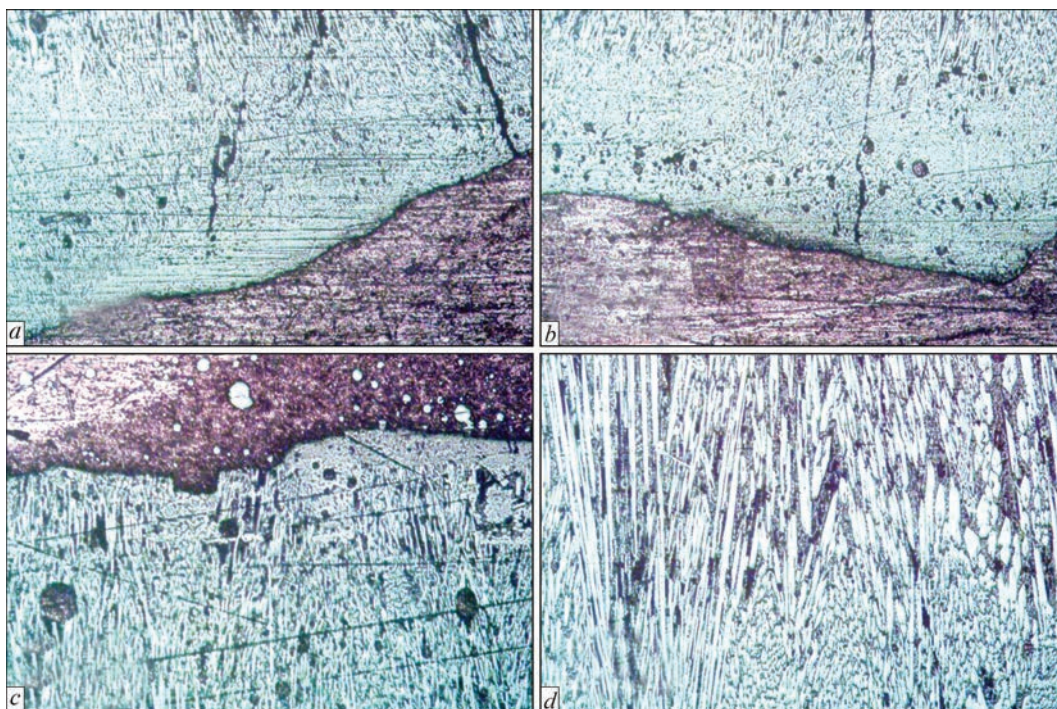


**Figure 6.** Microstructure ( $\times 100$ ) of metal, deposited by electric arc method by the self-shielding wire No. 2 (type of deposited metal 400Kh25GSM): *a*, *b* — fusion line; *c* — upper edge of deposited layer with the interlayer of copper; *d* — center of the deposited layer



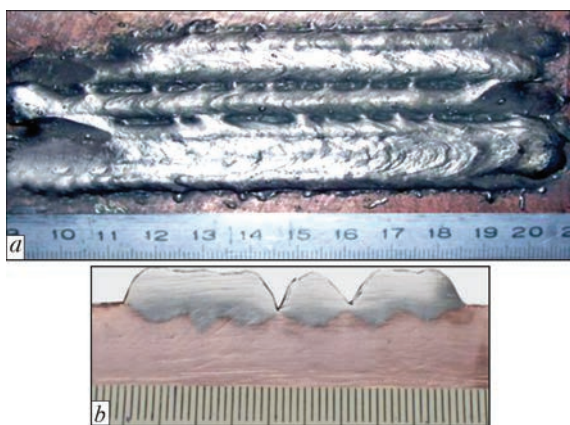


**Figure 7.** Appearance of beads, deposited on the specimen of M1 copper by the solid wire No. 3 (type of deposited metal N65Kh25M11B4) (a) and macrosection of their cross-section (b)

per base is observed, although the presence of single small pores located near the fusion line is noted. The hardness of deposited metal is *HRC* 56–60.

The study of the microstructure of the specimen, deposited by the wire No. 2, showed that the fusion line in it is quite pronounced, moreover, in the deposited layer cracks are present, some of which go out to the surface (Figure 6, a, b). Cracks of this type, characteristic of deposited metal of the type of high-chromium cast irons and, for example, in surfacing of wear-resistant bimetallic sheets, are not a sign of rejection [4].

In the given specimen, the presence of interlayer of cast copper in the upper part of the deposited layer with inclusions of wear-resistant metal is noted (Figure 6, c). Crystallization of deposited metal has a directional character (Figure 6, d).

The appearance of the specimen, deposited by the wire No. 3, is shown in Figure 7, a, and the macrosection of its cross-section is in Figure 7, b. A good formation of deposited beads and a high quality of fusion of the deposited nickel-based metal with copper should be noted, which has no defects in the deposited metal and on the fusion line. The hardness of the deposited metal is *HB* 245.

The microstructure of the fusion zone and a central part of the metal, deposited by the wire No. 3, are shown in Figure 8, a, b.

The study of the microstructure of this specimen showed the absence of defects both in the deposited metal as well as near the fusion line. It was found that the structure of the deposited metal is quite homogeneous. The nature of the fusion line of the base and deposited metals has a pronounced wavy shape, which is clearly visible at large magnifications (Figure 8, a).

The microstructure in the center of the deposited layer is quite homogeneous, it does not contain defects in the form of pores, inclusions, cracks, etc. (Figure 8, b). It represents a solid solution of chromium, molyb-

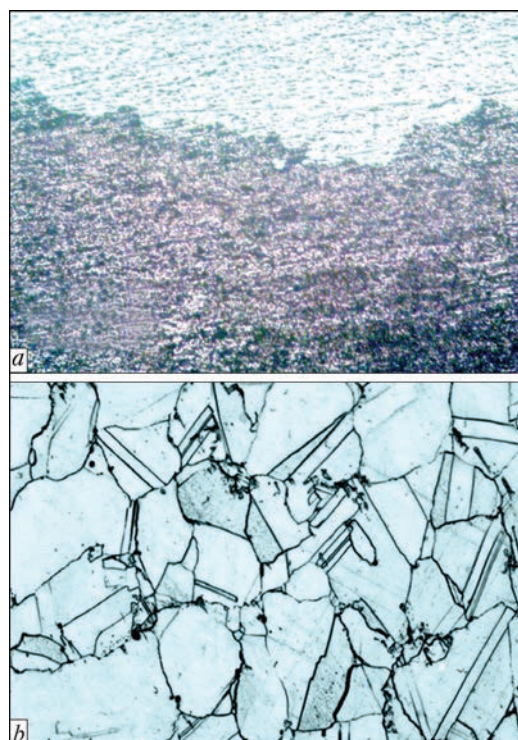


**Figure 8.** Microstructure of metal, deposited by the wire No. 3 (type of deposited metal N65Kh25M11B4): a — fusion line; b — central part of the metal of deposited layer.  $\times 100$  (a),  $\times 320$  (b)

denum, niobium and other alloying elements in nickel and has the appearance of a rather uniform mixture of coarse and fine grains, intersected by twin boundaries (Figure 8, b). The average grain size is in the range of 30–50  $\mu\text{m}$ .

## CONCLUSIONS

1. According to the results of experiments on electric arc surfacing by three wires that provide producing a wear-resistant deposited metal based on iron and nickel, on M1 copper, the modes were selected and technologies of arc surfacing by these wires were developed, which provide a satisfactory formation of deposited metal and its fusion with the base metal. In this case, from the point of view of welding and technological properties, the best results are provided by the use of the nickel-based wire.

2. While using the flux-cored wires, that provide producing the iron-based deposited metal (semi-heat-resistant steel and high-chromium cast iron), some defects in the deposited metal and on the fusion line were detected, whose admissibility will be determined by the conditions of operation of specific parts. The latter also refers to the nickel-based wire.

## REFERENCES

1. Gurevich, S.M. (1990) Nonferrous metal welding guide. Kyiv, Naukova Dumka [in Russian].
2. Lide, D.R., Haynes, W. (2018) *CRC Handbook of chemistry and physics: A ready-reference book of chemical and physical data*. Boca Raton, Taylor and Francis.



3. Babinets, A.A., Ryabtsev, I.O., Lentuyugov, I.P. et al. (2020) Problems and prospects of surfacing of copper and copper parts by wear-resistant layers (Review). *The Paton Welding J.*, **5**, 15–23. <https://doi.org/10.37434/tpwj2020.05.03>
4. Rjabcev, I.A., Senchenkov, I.K., Turyk, Je.V. (2015) Surfacing: Materials, technologies, mathematical modeling. Gliwice, Wydawnictwo Politechniki Slaskiej [in Russian].
5. Pereplyotchikov, E.F. (2004) Plasma-powder cladding of wear- and corrosion-resistant alloys in valve manufacturing. *The Paton Welding J.*, **10**, 31–37.
6. Pereplyotchikov, E.F. (2015) Plasma-powder cladding of nickel and cobalt alloys on copper and its alloys. *The Paton Welding J.*, **5-6**, 10–13. DOI:10.15407/tpwj2015.06.02
7. Silva, C.C., de Miranda, E.C., Motta, M.F. et al. (2012) Dilution control of weld overlay superalloys using Taguchi method. In: *Proc. of the ASME 31<sup>st</sup> Int. Conf. on Ocean, Offshore and Arctic Engineering*, **6**, 289–299.
8. Robert, W. Messler (2019) *A Practical Guide to Welding Solutions: Overcoming Technical and Material-Specific Issues*. Wiley-VCH Verlag GmbH & Co. KGaA. <https://doi.org/10.1002/9783527818815>

**ORCID**

I.O. Ryabtsev: 0000-0001-7180-7782,

A.A. Babinets:0000-0003-4432-8879,  
I.P. Lentuyugov: 0000-0001-8474-6819

**CONFLICT OF INTEREST**

The Authors declare no conflict of interest

**CORRESPONDING AUTHOR**

I.O. Ryabtsev

E.O. Paton Electric Welding Institute of the NASU  
11 Kazymyr Malevych Str., 03150, Kyiv, Ukraine  
E-mail: ryabtsev39@gmail.com

**SUGGESTED CITATION**

I.O. Ryabtsev, A.A. Babinets, I.P. Lentuyugov,  
I.L. Bogaychuk, A.I. Panfilov (2022) Electric arc  
surfacing of wear-resistant iron- and nickel-based  
alloys on copper. *The Paton  
Welding J.*, **3**, 10–15.

**JOURNAL HOME PAGE**

<https://pwj.com.ua/en>

Received: 19.04.2022

Accepted: 08.08.2022

# SELECTION OF PARAMETERS OF LASER WELDING OF THIN-WALLED ITEMS FROM LIGHT ALLOYS WITH NONTHROUGH THICKNESS PENETRATION

**V.M. Korzhyk<sup>1,2</sup>, V.Yu. Khaskin<sup>1,2</sup>, S.I. Peleshenko<sup>2</sup>, A.A. Grynyuk<sup>3</sup>, Dong Chunlin<sup>1</sup>, E.V. Ilyashenko<sup>2</sup>, Yuhui Yao<sup>4</sup>**

<sup>1</sup>China-Ukraine Institute of Welding, Guangdong Academy of Sciences, Guangdong Provincial Key Laboratory of Advanced Welding Technology, Guangzhou, 510650, China

<sup>2</sup>E.O. Paton Electric Welding Institute of the NASU  
11 Kazymyr Malevych Str., 03150, Kyiv, Ukraine

<sup>3</sup>National Technical University of Ukraine «Igor Sikorsky Kyiv Polytechnic Institute»  
37 Peremohy Ave., 03056, Kyiv, Ukraine

<sup>4</sup>Shenzhen Hanzhizi Technology Co., Ltd.

6<sup>th</sup> Floor, Building B, Bantian International Center, 5 Huancheng South Road, Longgang District, Shenzhen, Guangdong, China

## ABSTRACT

Light metal alloys (in particular, beryllium and aluminium) are applied in different engineering fields, for instance for fabrication of rocket and aircraft elements. When designing such engineering elements, there is the need to produce welded joints with different types of welds. Laser welding with nonthrough thickness penetration welds can be used for item sealing, welding-on flanges and welding thin-walled structures of up to 2–3 mm thickness. Toxic fumes form in welding beryllium alloys. Such a peculiarity requires reducing the number of technological experiments, aimed at selection of mode parameters. An up-to-date approach to solving the problem of light alloy welding is performance of preliminary calculated determination of mode parameters with their further experimental verification. Technological verification can be performed on high-strength aluminium alloys close by their physico-mechanical characteristics to beryllium alloys. Therefore, this work is devoted to preliminary determination of mode parameters of laser welding by a sealing weld with nonthrough thickness penetration of thin-walled flanges of cylindrical parts and box-shaped items from light metals and alloys based on Be and Al, taking into account the temperature of postweld heating. A procedure of preliminary calculated determination of mode parameters of laser welding of parts from a beryllium-based alloy is proposed in the work, which is suitable for both through-thickness and nonthrough-thickness penetration. Nonthrough-thickness penetration can be applied for welding-on flanges by a sealing weld. Experimental verification on samples from alloys of Al–Zn–Mg–Cu system and comparison with published data on beryllium alloy welding showed that the error of the proposed procedure is in the range of up to 15–20 %.

**KEYWORDS:** laser welding, light alloys, penetration, mode parameters, error, pores, cracks

## INTRODUCTION

Light metal alloys (beryllium, aluminium and magnesium) are applied in different engineering fields. In particular, they are used for manufacture of rocket and aircraft elements. When designing such engineering elements, it is necessary to produce welded joints. Welds of different types are used when making such joints. In particular, welds with nonthrough thickness penetration can be used for item sealing (for instance, welding flanges) and welding thin-walled structures up to 2–3 mm thick. In this case, it is necessary to apply highly efficient welding technologies, which allow achieving a guaranteed penetration depth in combination with minimizing residual welding deformations. This result is the easiest to achieve by applying welding with increased localization of thermal impact on the base metal. Laser welding is an example of one of the most acceptable welding processes [1].

A feature of welding structures, containing beryllium (actually, beryllium, beryllium-based alloys and aluminium-beryllium alloys), is toxicity of fumes, formed in the process. Such a feature requires reducing the number of preliminary technological experiments, aimed at selection of mode parameters. A similar approach is desirable also for selection of parameters of welding other light alloys (based on aluminium and magnesium). Therefore, a relevant approach to solving this problem is performance of preliminary calculation-based determination of mode parameters with further experimental verification. Preliminary technological verification can be performed on high-strength aluminium alloys close to beryllium ones by their physico-mechanical characteristics.

## ANALYSIS OF PUBLISHED DATA AND PROBLEM DEFINITION

Studying the features of welding parts from high-strength beryllium and aluminium alloys, for in-

stance, alloy of Be–AlSi system, showed that the weld strength largely depends on the structure geometry, penetration and presence of defects, and to a much smaller extent — on residual stresses [2]. Therefore, it is rational to base selection of laser welding parameters on certain geometry of penetration. One of the main defects of laser welding of the above-mentioned light alloys is pore formation that is largely related to the features of existence of the vapour-gas channel [3]. Therefore, it is necessary to take into account the behaviour of the vapour-gas channel, forming during laser radiation absorption by the base metal.

In work [4] the dynamics of weld pool behaviour at laser welding of aluminium alloys of different series is considered. Experiment results showed that at laser irradiation the metal evaporates with formation of a vapour-gas channel. This is followed by gradual melting of the metal, surrounding the vapour-gas channel, under the impact of heat evolving in it. The rate of increase of channel depth is directly proportional to overall content of elements with a low boiling temperature. At the stationary stage of the penetration process the channel depth and diameter are stabilized. In the longitudinal direction the melt pool area is inversely proportional to aluminium alloy heat conductivity. The rate of laser radiation absorption changes depending on the ratio of vapour-gas channel depth to its diameter and reaches the largest value of 58 %. In the case, if the surface tension and recoil pressure of the metal vapours are balanced, abrupt changes of the channel shape can be avoided.

In addition to vapour-gas channel behaviour, the metallurgical aspects also influence the weldability of high-strength light alloys. The main difficulties in welding these alloys are hot cracking, pore formation, cracking on defects (pores), lowering of ductility in the welds and HAZ. The following measures can be used to solve these problems [5]: control of Fe/Al ratio in the base metal to lower the hot cracking susceptibility, minimizing the content of oxides and initial grain size to limit crack formation on the defects and to increase the ductility, as well as selection of the process of welding and optimization of its parameters.

To reduce hot cracking of welded joints, it is rational to optimize such mode parameters as laser radiation power, welding speed, specific power and focal position [6]. This approach allows minimizing the welding heat input. Addition of filler metal of another chemical composition also promotes lowering of cracking sensitivity. This way it is possible to improve the joint ductility that promotes crack elimination [7]. In order to reduce porosity and improve the weld strength, it is necessary to avoid penetration of oxide film ( $\text{Al}_2\text{O}_3$  and/or BeO) into the weld pool [8]. For this purpose, it is rational to remove this film from the surfaces being welded directly before welding.

Note that filler material application in welding beryllium alloys is not always possible. So, in manufacture of some specialized beryllium parts for space satellites (for instance, cylindrical cases of energy source elements, operating at temperatures higher than 600 °C) penetration of extraneous chemical elements into the welded joints is inadmissible that does not allow applying welding filler materials or replacing welding by brazing [9]. It makes application of laser welding without filler desirable.

In manufacture of a range of aerospace engineering items using welding, the problem of sealing the inner cavities and compartments, containing electronics components, is solved. In these cases, it is necessary to both ensure sealing of such compartments and to avoid residual deformations and stresses in the structure. For this purpose, it is necessary to use welding technologies, which ensure producing relatively narrow welds with local heat input. Total heating of the item after welding should not be higher than 100–120 °C. Such a problem is readily solved by laser welding application.

Thus, at selection of the parameters of laser welding of light alloys by a sealing weld, it is rational to focus on producing nonthrough thickness penetration of a shape close to a triangular one. Here, the weld should be made with minimum heat input without filler material application.

## RESEARCH GOALS AND OBJECTIVES

The objective of the study is preliminary determination of the parameters of laser welding by a sealing weld with nonthrough thickness penetration of thin-walled flanges of cylindrical parts and boxlike items from light metals and alloys based on Be and Al, taking into account the postweld heating temperature.

The following problems are solved to achieve the defined goal:

- calculation-based determination of mode parameters of laser welding of light alloys based on Be and Al with a nonthrough thickness penetration;
- calculation-based determination of heating temperatures for small-sized laser-welded items based on Be and Al;
- experimental verification of the selected mode parameters of laser welding of samples from an aluminium alloy and their heating temperatures.

## PREDICTION OF MODE PARAMETERS OF LASER WELDING OF HIGH-STRENGTH LIGHT ALLOYS

When producing thin-walled items by sealing welds, disc-shaped or rectangular flanges may be welded to cylindrical or boxlike structures from light alloys. The main parameters of these structures are given in



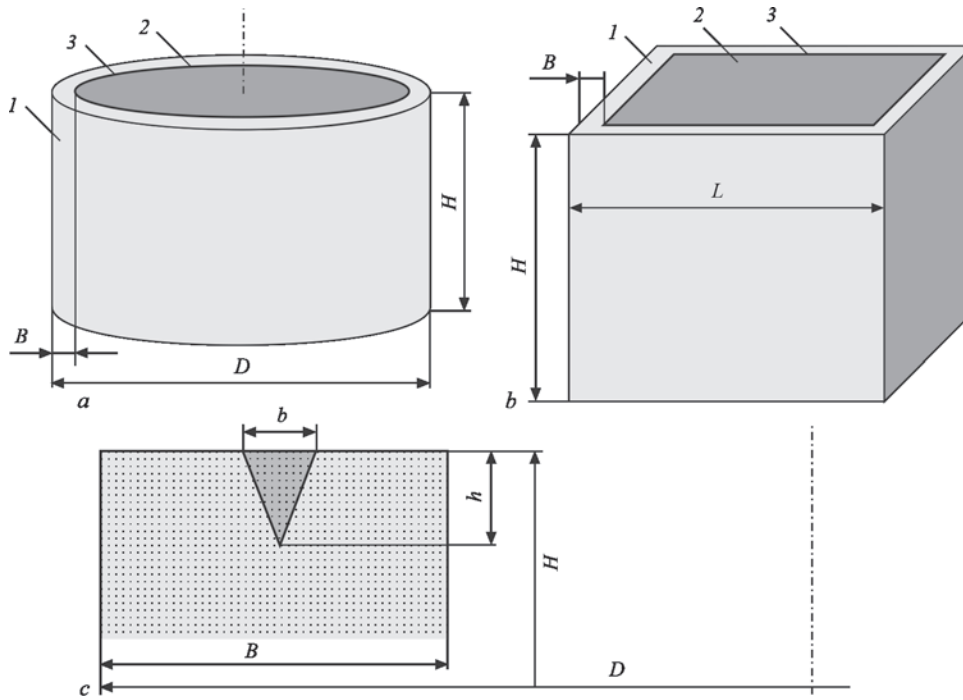


**Figure 1.** Geometrical parameters of the parts being welded and laser penetration (dark triangular region): 1 — case; 2 — flange being welded; 3 — weld

Figure 1. Let us consider two cases. In the first case, a disc flange of close thickness is welded to a cylindrical case of diameter  $D$ , height  $H$ , and wall thickness  $B$  (Figure 1, *a*). In the second case, a rectangular flange of a close thickness is welded to a boxlike structure of width  $L$  and height  $H$  ( $L = H$  variant) with walls of thickness  $B$  (Figure 1, *b*). In both the cases, the weld (simplified) has the form of a triangle with base  $b$ , which is the weld width, and height  $h$ , which is the penetration depth (Figure 1, *c*). To simplify the problem being solved we assume that:  $D = L = H = 40\text{--}50\text{ mm}$ ,  $B = 1.5\text{ mm}$ .

To reduce the risk of appearance of residual deformations and hot cracking susceptibility, it is desirable to avoid increase of the temperature of part being welded above  $100\text{--}120\text{ }^{\circ}\text{C}$ . That is why we will divide the definition and solution of the thermal problem of welding the flange of a part from a beryllium (aluminium) alloy into two related, but rather autonomous tasks:

- selection of technological parameters of welding (heat source power, welding speed), proceeding from the geometrical dimensions of the weld;
- determination of temperature parameters of the part after welding.

#### SELECTION OF TECHNOLOGICAL MODE PARAMETERS IN LASER WELDING OF HIGH-STRENGTH LIGHT ALLOYS

At determination of laser welding parameters we will proceed from the fact that the masses of the cylindrical and boxlike parts are approximately the same. The parts are hollow in both the cases. Then, the mass of

the part being welded, which is a hollow cylinder of diameter  $D$  with wall thickness  $B$ , is equal to:

$$m_{\text{piece}} = \frac{\pi}{4} \gamma H \left[ D^2 - (D - 2B)^2 \right], \quad (1)$$

while the weld mass

$$m_w = \pi \gamma (D - B) S_w, \quad (2)$$

where  $\gamma$  is the density of metal (beryllium or aluminium).

Figure 2 shows the dependencies of specific heat values of beryllium and aluminium on temperature  $T$  [10]. It should be noted that beryllium has the highest heat capacity among metals, which strongly depends on temperature. As one can see from Figure 2, *a*, the heat capacity values at room temperature and at melting temperature differ by approximately three times (area  $c_{\text{solid}}$ ). Moreover, a jumplike decrease in heat capacity occurs at melting. Heat capacity of liquid beryllium is little studied; it is constant at temperatures a little higher than the melting temperature [10], i.e. it does not depend on temperature (area  $c_{\text{liquid}}$ ). We will take it into account in the heat balance, by which we will describe the laser welding process.

All the energy, given off by laser radiation to the metal being welded, is spent for its heating up to the melting temperature, melting proper, liquid metal heating up to boiling temperature and partial evaporation of metal. The heat balance equation has the following form:

$$(1 - \beta) P_L = \gamma v S_w \times \left[ \int_{T_0}^{T_m} c_{\text{solid}}(T) dT + q_m + \int_{T_m}^{T_{\text{max}}} c_{\text{liquid}}(T) dT + \xi q_{\text{ev}} \right], \quad (3)$$

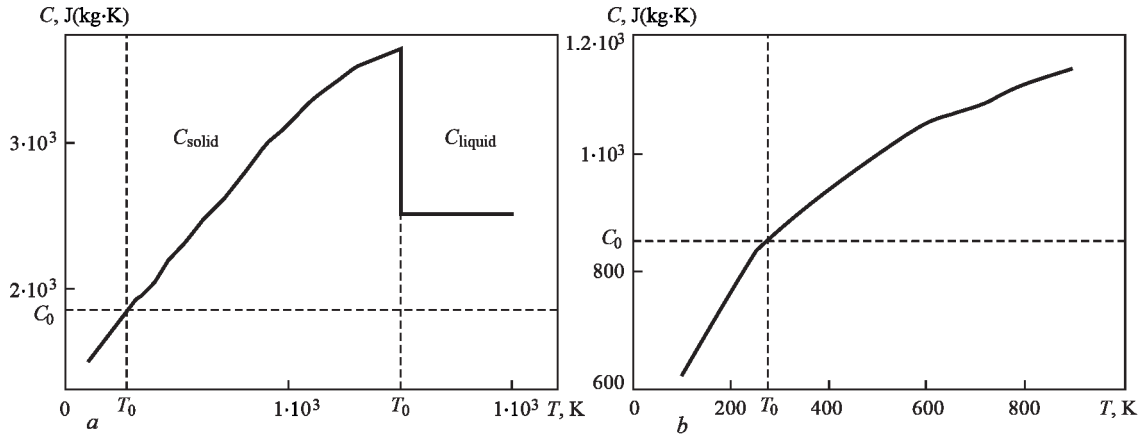


**Figure 2.** Dependencies of specific heat conductivity of beryllium (*b*) and aluminium (*a*) on temperature *T*:  $T_0$  — ambient temperature;  $T_m$  — melting temperature;  $c_0$  — specific heat under normal conditions, given in reference sources [10]

where  $P_L$  is the laser radiation power;  $\beta$  is the metal reflectivity;  $v$  is the welding speed;  $q_m$  and  $q_{ev}$  is the latent heat of melting and vaporization;  $\xi$  is the fraction of metal, which evaporated (usually, it is 3–5 %);  $T_{max}$  is the maximum temperature of metal heating.

Equation (3) was written for laser welding with a vapour-gas channel. Here, maximum temperature  $T_{max}$  is higher than the metal boiling temperature  $T_b$  by several degrees.

Using the heat balance equation (3), we can determine the technological parameters of welding, depending on the required weld dimensions. For instance, welding speed is determined by penetration depth and power of the laser, which is used

$$v = \frac{(1-\beta)P_L}{\gamma S_w \left[ \int_{T_0}^{T_m} c_{solid}(T) dT + q_m + \int_{T_m}^{T_{max}} c_{liquid}(T) dT + \xi q_{ev} \right]} \cdot (4)$$

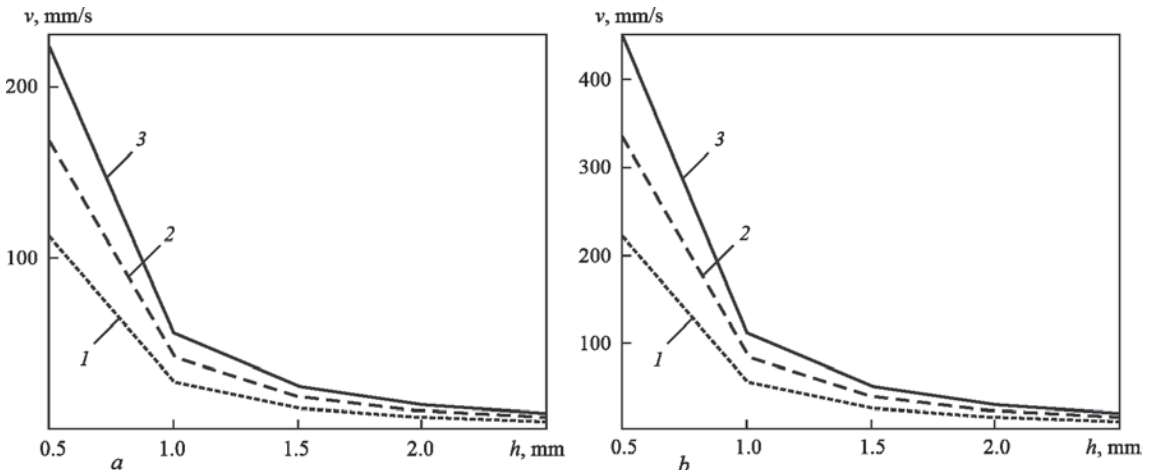
Formula (4) was used to calculate the dependencies of laser radiation speed on penetration depth at different power of laser radiation (Figure 3). They make it easy

to select such an important technological parameter, as welding speed, to ensure the required penetration depth. Here, it is necessary to consider some limitations. So, at low speeds, the weld width can become greater than the item wall thickness, which is inadmissible. At high speeds, weld formation defects of the type of undercuts and lacks-of-fusion, may appear.

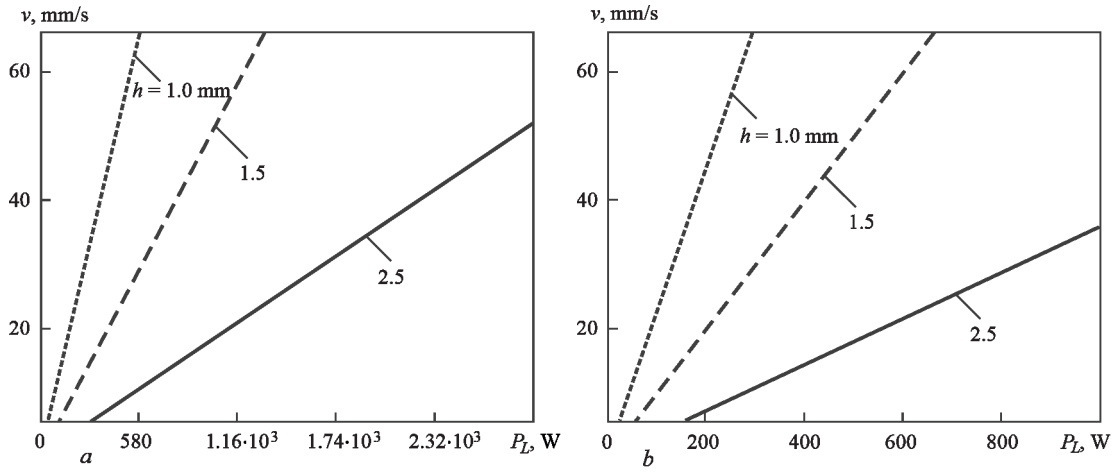
Figure 4 presents the dependence of laser welding speed on laser power at different penetration depths. The data in Figures 3 and 4 can be used to select the welding speed and radiation power, which allow achieving the required penetration depth, when ensuring the respective quality and tightness of the item.

Figure 4 shows the attractiveness of application of the technological modes of welding, with which the speed varies in the range from 30 to 70 mm/s, and laser power — from 500 to 2000 W for beryllium and from 300 to 1000 W for aluminium. Here, the process of laser welding is ensured without application of any additional technological measures or equipment.

Equation (3) allows determination of laser power, necessary to achieve the required penetration depth. Obviously, it is also determined by welding speed:



**Figure 3.** Dependence of speed  $v$  of laser welding of beryllium (*a*) and aluminium (*b*) on penetration depth  $h$  at different laser power  $P_L$ : 1 —  $P = 500$  W; 2 — 750; 3 — 1000



**Figure 4.** Dependence of speed  $v$  of laser welding of beryllium (a) and aluminium (b) on laser power  $P_L$  at different penetration depths  $h$

$$P_L = \frac{\gamma v S_w}{1 - \beta} \times \left[ \int_{T_0}^{T_m} c_{solid}(T) dT + q_m + \int_{T_m}^{T_{max}} c_{liquid}(T) dT + \xi q_{ev} \right]. \quad (5)$$

Figure 5 shows the dependencies of laser power on laser welding speed at different penetration depth. These dependencies allow determination of the ranges of radiation power, required for welding on flanges of  $\delta \sim 1.5$  mm thickness with nonthrough thickness penetration to cases with a not smaller wall thickness. For the case of welding beryllium alloys this is the range of 800–1200 W, for the case of welding aluminium alloys this is 400–800 W. Such power ranges allow welding at acceptable speeds, as well as covering rather wide ranges of penetration depths.

Figure 6 shows the dependencies of laser power on penetration depth at different laser welding speeds. These dependencies demonstrate that it is enough to apply an 800–1600 W laser for beryllium alloys and 400–1000 W laser for aluminium alloys, in order to ensure penetration with a guaranteed depth of 1.0–1.5 mm.

Thus, the proposed procedure allows making preliminary assessment of the technological parameters of the welding process, as well as selecting equipment (in particular, technological laser), which is necessary for realization of the process.

#### CALCULATION OF AVERAGE TEMPERATURE OF THE ITEM AFTER LOCAL HEATING DURING WELDING

In order to determine the part temperature after welding, we will proceed from the fact that the temperature of local heating of the item in the weld zone (dark triangular area in Figure 1) is much higher than that of the item. When the weld cools down its temperature and that of the item are equalized. If we denote average temperature as  $T_x$ , then the equation of energy balance has the following form:

$$m_w \left[ \int_{T_x}^{T_m} c_{solid}(T) dT + q_m + \int_{T_m}^{T_{max}} c_{liquid}(T) dT \right] = m_{piece} \int_{T_0}^{T_x} c_{solid}(T) dT. \quad (6)$$

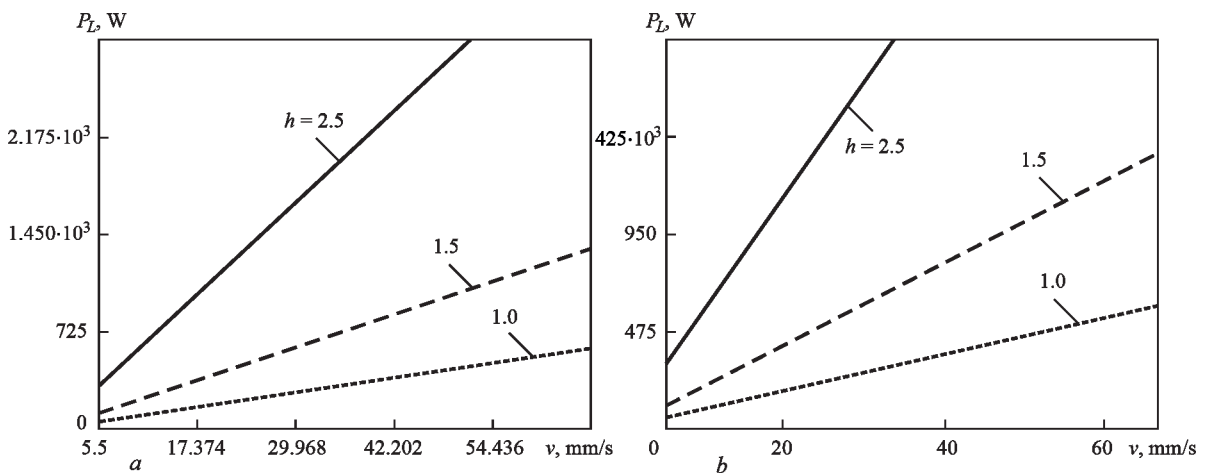


**Figure 5.** Dependence of laser power  $P_L$  on speed  $v$  of welding beryllium (a) and aluminium (b) at different penetration depths  $h$



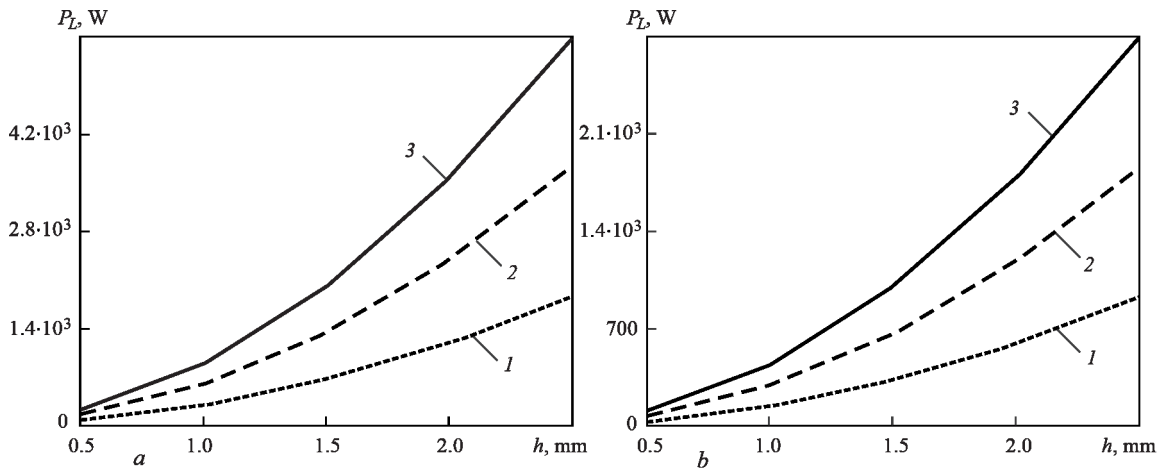


**Figure 6.** Dependence of laser power  $P_L$  on penetration depth  $h$  at different speeds  $v$  of laser welding of beryllium (a) and aluminium (b): 1 —  $v = 16.67$ ; 2 —  $33.3$ ; 3 —  $50$  mm/s

In other words, the energy, evolving at cooling both of the liquid metal and the solidifying metal, together with the latent heat of melting, is consumed for heating the rest of the item from ambient temperature  $T_0$  up to temperature  $T_x$ .

Equation (5) is nonlinear with the special feature that the unknown is included into it as the limit of integration of the determined integrals.

There are still no established procedures to solve such equations. Therefore, we modified the known methods of numerical solution of nonlinear equations. One of the problems arising when solving equation (6), was that of significant time losses at calculations. This was explained by the need to numerically determine the values of two integrals with a changing boundary at each iteration step. The situation was made more complicated by that the functions that are under the integral sign, were assigned by the table, i.e. by points. To achieve an acceptable accuracy, it was necessary to use cubic spline interpolation.

Therefore, calculations yielded a not very large data file (Tables 1 and 2), which are still enough for preliminary evaluation conclusions. Numerical experiments were conducted at the following constant parameters: part outer diameter  $D = 40$  mm; part height  $H = 50$  mm; ambient temperature  $T_0 = 27$  °C; for Table 2 wall thickness  $B = 1.5$  mm.

Analysis of the obtained results showed that it is possible to select the welding process parameters, which ensure such weld dimensions, at which item overheating above 100 °C is not reached. So, in welding thin-walled items ( $B = 1.5$  mm) it is desirable for weld width not to exceed 1.5 mm.

Item wall thickness  $B$  and weld width  $b$  have the greatest influence on item heating. At selection of mode parameters, it should be taken into account that welding at higher speeds promotes reduction of weld width. Therefore, application of high-speed modes to reduce the average temperature of the item is promising.

### EXPERIMENTAL VERIFICATION OF THE SELECTED PARAMETERS OF LASER WELDING

A laboratory set-up based on fiber laser of MFSC 2000W model (MAX Company, China) of up to 2000 W power was developed to perform experimental check-up. Radiation of this laser was focused by a welding head shown in Figure 7 into a spot of approximately 0.2 mm diameter by optics with 200 mm focal distance. Welding was performed with argon shielding with flow rate of 8–10 l/min. Only aluminium alloys were used in the experiments, to avoid the danger of poisoning by welding fumes. Aluminium alloys 7005 (1915) and 7075 of Al–Zn–Mg–Cu system were selected as sample materials. By their physico-mechanical characteristics these alloys are the closest to commercial beryllium-aluminium alloys of Be–Al–Mg system (Tables 3, 4). Flat and cylindrical samples with wall thickness  $B = 1.5$  mm were made from these alloys. Flat samples of  $50 \times 50 \times 1.5$  mm size were welded by

**Table 1.** Dependence of average temperature  $T_x$  of the item on thickness  $B$  of its wall (weld width  $b = 1.0$  mm)

Item wall thickness $B$ , mm	Average temperature $T_x$ (Be alloy), °C	Average temperature $T_x$ (Al alloy), °C
1.0	88	83
1.2	80	77
1.5	74	71
2.5	63	61
3.0	61	59

**Table 2.** Dependence of item average temperature  $T_x$  on weld width  $b$  (item wall thickness  $B = 1.5$  mm)

Weld width $b$ , mm	Average temperature $T_x$ (Be alloy), °C	Average temperature $T_x$ (Al alloy), °C
0.5	54	53
1.0	74	71
1.2	85	81
1.5	106	100
2.5	203	186



**Figure 7.** Laboratory stand for conducting experiments on laser welding of flanges by sealing welds with nonthrough thickness penetration of the thin-walled cylindrical item from an aluminium alloy linear fillet welds, cylindrical samples of 40×50 mm size were joined by circumferential welds.

Welding of samples was performed using calculated parameters of the modes (Figures 3–6). So, in order to obtain joints with penetration depth  $h \sim 0.6$  mm, in keeping with the data in Figure 3,  $b$ , it is recommended to select welding speed of 150 mm/s at laser radiation power  $P_L = 500$  W. By the data of Figure 5,  $b$  a speed of 66.7 mm/s will be required at radiation power

of up to 400 W. By the data of Figure 6,  $b$  at welding speed of 50 mm/s, the radiation power should be in the range of  $P_L = 350 - 400$  W. Power  $P_L = 400$  W and speed  $v = 66.7$  mm/s were selected during experiment performance. A weld of depth  $h \sim 0.6$  mm and width  $b \sim 0.6$  mm was produced as a result (Table 5).

Thus, in keeping with Figures 3,  $b$ –6,  $b$  a number of mode parameters were selected, which were used to conduct experiments on laser welding. The modes and the obtained results (in the form of transverse macrosections of the welds) are given in Table 5.

Measurements of sample heating temperature were performed during performance of experiments on welding in the modes, given in Table 5 (Figure 8). Here, an infrared pyrometer of GM320 model (Bene-tech Shenzhen Jumaoyuan Science and Technology Co., Ltd., Shenzhen, PRC) with measurement range of  $-50$ – $+380$  °C and up to 1.5 °C error was used. Temperature measurements were conducted in the zone of welded structure side surface closest to the weld directly after completion of the welding process. Measurement distance was  $Y = 300$ – $500$  mm.

For instance, to produce welds with penetration depth  $h \sim 1.0$  mm, in keeping with the data of Table 5, welding was performed at speed  $v = 58$  mm/s at 500 W radiation power. After welding, an optical pyrometer was used to measure the welded sample temperature. Performed measurements showed that temperature is within 70–75 °C that corresponds to the data of Tables 1 and 2 with up to 6 % error. Further experiments showed that the discrepancy between the calculated and experimental data on welded sample heating is not greater than 10 %.

Comparison of such calculated and experimentally established mode parameters, as power  $P_L$  and welding speed  $v$ , as well as penetration depth  $h$ , allows us to say that in keeping with the proposed calculation procedure the mode parameters of laser welding of light alloys can

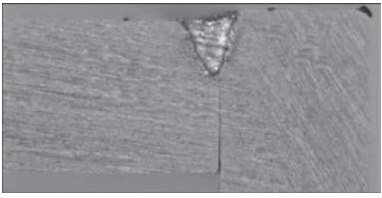
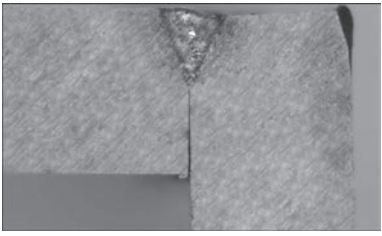
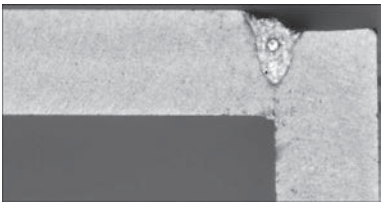
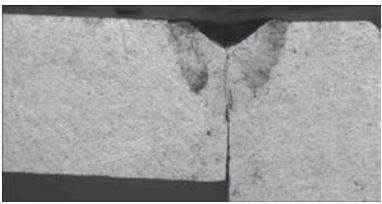
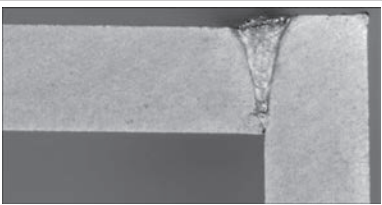
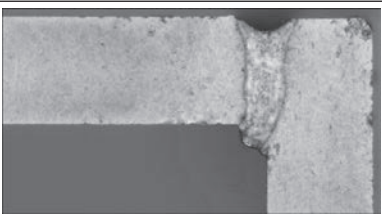
**Table 3.** Content of chemical elements (wt.%), used when studying the aluminium alloys and the examined beryllium alloy

Alloy grade	Al	Be	Si	Fe	Cu	Mn	Mg	Cr	Zn	Ti	Other
7005 (1915)	Base	–	Up to 0.35	Up to 0.40	Up to 0.10	0.2–0.7	1.0–1.8	0.06–0.2	4–5	0.01–0.06	Zr 0.08–0.2; other up to 0.15
7075	Same	–	Up to 0.40	Up to 0.50	1.2–2.0	Up to 0.30	2.1–2.9	0.18–0.28	5.1–6.1	Up to 0.20	Up to 0.15
Lx-59-3	38	59	–	–	–	–	3	–	–	–	–
Lx-40-3	57	40	–	–	–	–	3	–	–	–	–

**Table 4.** Main physico-mechanical characteristics of the considered aluminium and beryllium-aluminium alloys (at normal temperature)

Alloy grade	Yield limit $\sigma_y$ , MPa	Ultimate strength $\sigma_t$ , MPa	Relative elongation, %	Young’s modulus $E$ , GPa	Density $\rho$ , kg/m <sup>3</sup>	Hardness $HB$ , MPa
7005 (1915)	245–290	355–400	8–12	72	2770	90–95
7075	450–500	510–570	3–11	71.7	2810	150–160
Lx-59-3	280–480	220–490	1–9	175–200	2100	250
Lx-40-3	350–490	250–530	1–9	180–200	2100	250

**Table 5.** Comparison of calculated parameters of the modes with experimental results of laser welding of 7075 alloy

No.	Variants of calculated parameters of the mode /h	Experimentally established mode parameters /h, b	Error (by h parameter), %	Result (×30)
1	1) $P_L = 300$ W, $v = 67$ mm/s; 2) $P_L = 500$ W, $v = 200$ mm/s /h = 0.5–0.53 mm	$P_L = 350$ W, $v = 67$ mm/s /h = 0.51 mm; b = 0.5 mm	2–4	
2	1) $P_L = 350$ W, $v = 67$ mm/s; 2) $P_L = 500$ W, $v = 150$ mm/s /h = 0.55–0.6 mm	$P_L = 400$ W, $v = 67$ mm/s /h = 0.63 mm; b = 0.62 mm	5–15	
3	1) $P_L = 500$ W, $v = 50$ mm/s; 2) $P_L = 750$ W, $v = 80$ mm/s /h = 1.0 mm	$P_L = 500$ W, $v = 58$ mm/s /h = 1.1 mm; b = 0.86 mm	10	
4	1) $P_L = 500$ W, $v = 42$ mm/s; 2) $P_L = 750$ W, $v = 66$ mm/s /h = 1.2–1.3 mm	$P_L = 500$ W, $v = 50$ mm/s /h = 1.18 mm; b = 1.28 mm	2–9	
5	1) $P_L = 500$ W, $v = 28$ mm/s; 2) $P_L = 750$ W, $v = 33$ mm/s /h = 1.3–1.5 mm	$P_L = 600$ W, $v = 50$ mm/s /h = 1.34 mm; b = 0.86 mm	3–11	
6	1) $P_L = 500$ W, $v = 25$ mm/s; 2) $P_L = 750$ W, $v = 37$ mm/s /h = 1.5–1.6 mm	$P_L = 650$ W, $v = 33$ mm/s /h = 1.5 mm; b = 0.77 mm	2.5	

be determined with an up to 15 % error. Such an accuracy is acceptable in technological calculations.

### DISCUSSION OF THE RESULTS OF FORMING LIGHT ALLOY JOINTS BY LASER WELDING

Conducted technological studies showed an acceptable level of error for the proposed calculation procedure. It can be assumed that the discrepancy between the calculated and experimental results is associated, in particular, with allowing for the base metal reflectivity  $\beta$ . This value depends both on metal heating temperature [11],

and on the presence of an oxide film on the edges being welded, which absorbs the laser radiation much better than pure aluminium does [12]. Penetration of depth  $h \sim 1.18$  mm (Table 5, item 4) is an example of it. In this case, a considerable increase of the remelted metal volume was observed, which is reflected in the weld widening without any significant increase in radiation power. Such an effect is attributable to lowering of radiation losses ( $\beta$  coefficient), because of penetration of  $Al_2O_3$  oxide film into the weld pool.

Studies of welds made on 7005 and 7075 alloys showed that inner pores and cracks are the character-





**Figure 8.** Scheme of measurement of sample heating temperature after welding by manual infrared pyrometer (dashed line visualizes the laser sight)

istic defects of their formation. Pores formed not in all the welds, but just in certain cases (for instance, Table 5, items 2 and 3). Their size is within 0.05–0.2 mm, and they are located mostly in the middle part of the weld. Pore location along the weld is irregular, and their spacing varies from 2.5 up to 50 mm and more (Figure 9). However, their formation sites predominantly coincide with the rolling bands of the welded sheets. We can assume that these pore formation are associated with penetration of fine particles of  $\text{Al}_2\text{O}_3$  oxide film, as well as air, into the weld pool. The latter also comes in from the lower side of the butt being welded, which does not have gas protection. Cracks formed, predominantly at nonthrough thickness welding of 7075 alloy in the weld root part (see Table 5, item 4). The susceptibility to their formation becomes higher with increase of weld width. It is probable that the partial-penetration butt joint acts as a stress raiser that, combined with the residual stresses, promotes crack formation.

Rather accurate (with up to 10 % error) determination of the temperature of postweld heating of thin-walled items of the above-mentioned dimensions can be regarded as another confirmation of the acceptability of the proposed procedure. Comparison of the calculated results with some literature data was conducted to check the acceptability of the calculation procedure in welding beryllium alloys.

So, the data of welding 0.35 mm thick beryllium by pulsed Nd:YAG laser are given in work [13]. Welding was performed at the speed of 3.3 mm/s at radiation power density of 260 W/mm<sup>2</sup>. For our case (fiber laser radiation which is focused into a 0.2 mm diameter spot), it corresponds to the power of ~ 10 W (taking into account the losses). It can be assumed that for welding 0.35 mm beryllium by radiation of power  $P_L \sim 100$  W the welding speed is close to 33.33 mm/s, and for a thickness of 0.7 mm,  $P_L \sim 300$  W and  $v = 66.67$  mm/s will be required. It follows from the graph in Figure 4, *a* that a speed of  $v \sim 66.67$  mm/s is required for achieving a penetration of the order of 0.7 mm at power  $P_L \sim 300$  W. From the graph in

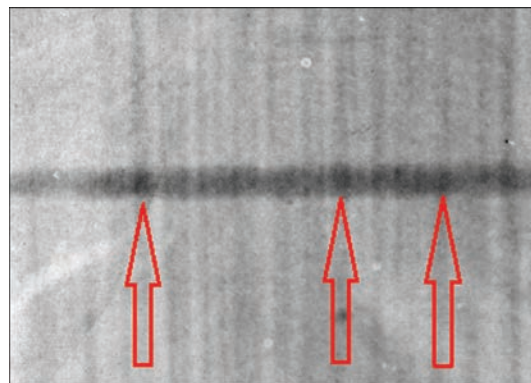


**Figure 9.** Detection of pores in welds by the results of radiographic testing (penetration in 7075 alloy sheet, made in the mode of item 3, Table 5)

Figure 5, *a* one can see that power  $P_L \sim 300$  W is necessary to produce a penetration depth of the order of 0.7 mm at speed  $v = 55$  mm/s. Thus, the discrepancy between the experimental and calculated values is less than 20 %.

Work [14] describes welding of beryllium alloys by electron beam process. Owing to a difference in pressure at electron beam and laser welding, their comparison is not quite correct. So, at laser welding the influence of low pressure atmosphere leads to increase of penetration depth by 10–20 % [15]. However, we will make such a comparison to obtain evaluation results. The following welding mode parameters were selected for electron beam welding of 1.5 mm plates: accelerating voltage  $U = 100$  kV, beam current  $I = 7$  mA, welding speed  $v = 8.5$  mm/s. Here, the electron beam power density is  $\sim 14 \cdot 10^4$  W/cm<sup>2</sup> that corresponds to laser beam power of ~ 300 W. It can be assumed that at equivalent laser power of 600 W, the welding speed will be ~ 17 mm/s. We obtain similar data from the graph in Figure 6, *a*. Allowing for the difference in pressures, it can be assumed that the discrepancy between the experimental and calculated values is up to 20 %.

## CONCLUSIONS

1. A procedure of calculation-based determination of the parameters of laser welding of thin-walled (up to 2.5 mm thick) items from high-strength light metals and alloys was proposed. Experimental verification on samples from aluminium alloys of 7xxx series of Al–Zn–Mg–Cu system and comparison with published data on beryllium alloy welding showed that the error of the proposed procedure is up to 15–20 %.

2. This procedure was used to select the main parameters of laser welding of a structure from 7075 alloy with 1.5 mm wall thickness by welds of 0.5–1.5 mm depth and 0.5–1.5 mm width. It was found that in welding by radiation of a fiber laser of up to 650 W power at not less than 33.3 mm/s speeds, minimal bulk heating of the items not higher than 100 °C is ensured.

3. Solving a nonlinear equation of heat balance allowed determination of the item postweld heating temperature with up to 10 % error.

4. Experimental studies showed that the characteristic defects of laser welding of aluminium alloys of Al–Zn–Mg–Cu-system are inner pores of 0.05–0.2 mm diameter and cracks in the weld root part at their formation with incomplete penetration. Pore formation may be related to air ingress into the weld pool from the side of the butt, and cracks can be associated with the butt acting as the notch — stress raiser, which promotes crack formation under the impact of residual stresses.

*DEDICATION. The authors dedicate this study to the memory of Prof. V.M. Sydorets, Dr. of Science (Eng.) (PWI), owing to those works it was performed.*

*The work was performed with the support of the following projects:*

1. *The National Key Research and Development Program of China — in the framework of the strategy “One Belt — One Road” (grant number 2020YFE0205300);*

2. *Strategic project of the Academy of Sciences of Guangdong Province (GDAS “Project of Science and Technology Development, 2020GDASYL-202030100), China;*

3. *Project of the Guangdong Economic and Technological Development Zone 2019GH19, China.*

## REFERENCES

- Bunaziv, I., Akselsen, O.M., Ren, X. et al. (2021) A review on laser-assisted joining of aluminium alloys to other metals. *Metals*, 1680(11), 1–40. DOI: <https://doi.org/10.3390/met11111680>
- Criss, E.M. (2015) *Surrogacy of beryllium welds and heat transfer in metals*: Dissertation for the degree Dr. of Philosophy (Mechanical Engineering), University of California, San Diego (USA) Permalink: <http://escholarship.org/uc/item/8sx939v4>
- Zhao, T., Sato, Y.S., Xiao, R. et al. (2020) Laser pressure welding of Al–Li alloy 2198: Effect of welding parameters on fusion zone characteristics associated with mechanical properties. *High Temperature Materials and Processes*, 39(1), 146–156. DOI: <https://doi.org/10.1515/htmp-2020-0047>
- Miyagi, M., Wang, H., Yoshida, R. et al. (2018). Effect of alloy element on weld pool dynamics in laser welding of aluminium alloys. *Scientific Reports*, 12944(8), 1–10. DOI: <https://doi.org/10.1038/s41598-018-31350-4>
- Hill, M., Damkroger, B.K., Dixon, R.D., Robertson, E. (1990) *Beryllium weldability*. Los Alamos National Laboratory, Materials Weldability Symposium, ASM Materials Week. Detroit, Michigan (USA). Permalink, <https://www.researchgate.net/publication/236557474>
- Ahn, J., Chen, L., He, E. et al. (2018) Optimisation of process parameters and weld shape of high power Yb-fibre laser welded 2024-T3 aluminium alloy. *J. of Manufacturing Processes*, 34, Pt A, 70–85. DOI: <https://doi.org/10.1016/j.jmapro.2018.05.028>
- Veness, R., Simmons, G., Dorn, C. (2011) *Development of beryllium vacuum chamber technology for the LHC*. In: *Proc of IPAC2011*, San Sebastián, Spain, TUPS024, 1578–1580.
- Doshi, S.J., Gohi, A.V., Mehta, N.D., Vaghasiya, S.R. (2018) Challenges in fusion welding of al alloy for body in white, *Materials Today: Proceedings*, 5(2), Pt 1, 6370–6375. DOI: <https://doi.org/10.1016/j.matpr.2017.12.247>
- Hanafee, J.E., Ramos, T.J. (1995) Laser Fabrication of Beryllium Components. In: *Proc. of 2<sup>nd</sup> Int. Energy Agency Inter. Workshop on Beryllium Technology for Fusion*. Moran, Wyoming, USA, September 6–8, 1995.
- Chirkin, V.S. (1968) *Thermophysical properties of materials of nuclear engineering*: Handbook. Moscow, Atomizdat [in Russian].
- Khaskin, V.Yu., Korzhik, V.N., Sydorets, V.N. et al. (2015) Improving the efficiency of hybrid welding of aluminum alloys. *The Paton Welding J.*, 12, 14–18. DOI: <https://doi.org/10.15407/tpwj2015.12.03>
- Miller, E., Liu, S. (2018) *Laser welding of aluminum alloys*. ASM Handbook Online. DOI: <https://doi.org/10.31399/asm.hb.v02a.a0006502>
- Hanafee, J.E., Ramos, T.J. (1995) Laser Fabrication of Beryllium Components. In: *Proc. of 2<sup>nd</sup> Int. Energy Agency Inter. Workshop on Beryllium Technology for Fusion*. Moran, Wyoming, USA, September 6–8, 1995.
- Campbell, R.P., Dixon, R.D., Liby, A.L. (1978) *Electron-beam fusion welding of beryllium*. Rockwell Int. (USA), RFP-2621, January 1.
- Khaskin, V.Yu., Shulym, V.F., Bernatsky, A.V. et al. (2012) Laser welding in low pressure atmosphere. *Visnyk NUK*, 5, 167–169 [in Russian].

## ORCID

V.M. Korzhik: 0000-0001-9106-8593,  
V.Yu. Khaskin: 0000-0003-3072-6761,  
S.I. Peleshenko: 0000-0001-6828-2110,  
A.A. Grynyuk: 0000-0002-6088-7980,  
Dong Chunlin: 0000-0003-2672-5985,  
E.V. Ilyashenko: 0000-0001-9876-0320,  
Yuhui Yao: 0000-0001-7196-1317

## CONFLICT OF INTEREST

The Authors declare no conflict of interest

## CORRESPONDING AUTHOR

V.M. Korzhik  
E.O. Paton Electric Welding Institute of the NASU  
11 Kazymyr Malevych Str., 03150, Kyiv, Ukraine.  
E-mail: [vnkorzhik@gmail.com](mailto:vnkorzhik@gmail.com)

## SUGGESTED CITATION

V.M. Korzhik, V.Yu. Khaskin, S.I. Peleshenko, A.A. Grynyuk, Dong Chunlin, E.V. Ilyashenko, Yuhui Yao (2022) Selection of parameters of laser welding of thin-walled items from light alloys with nonthrough thickness penetration. *The Paton Welding J.*, 5, 16–25.

## JOURNAL HOME PAGE

<https://pwj.com.ua/en>

Received: 14.04.2022

Accepted: 08.08.2022

<https://doi.org/10.37434/tpwj2022.05.04>

# ARGON-ARC WELDING OF HIGH-TEMPERATURE TITANIUM ALLOY DOPED BY SILICON

S.V. Akhonin, V.Yu. Bilous, R.V. Selin, I.K. Petrychenko, L.M. Radchenko, S.B. Rukhanskyi

E.O. Paton Electric Welding Institute of the NASU  
11 Kazymyr Malevych Str., 03150, Kyiv, Ukraine

## ABSTRACT

Welding of titanium alloys doped by silicon requires application of additional technological operations, such as local heat treatment and preheating. In view of the fact that tungsten electrode argon-arc welding became widely applied in industry, the possibility of application of preheating for argon-arc welding of high-temperature pseudo- $\alpha$  titanium alloy of Ti–5.6Al–2.2Sn–3.5Zr–0.4Mo–1.0V–0.6Si system was studied. In the work, preheating of the joints to the temperatures of 200 and 400 °C was used. The temperature of preheating before welding in the range of 200–400 °C does not influence the final microstructure of the produced welded joints. AAW-joints of high-temperature pseudo- $\alpha$  Ti–5.6Al–2.2Sn–3.5Zr–0.4Mo–1.0V–0.6Si alloy, produced with the preheating to 400 °C, have the highest ultimate tensile strength on the level of  $\sigma_t = 1160.1$  MPa, impact toughness values of samples with a sharp notch are on the level of 8.3 J/cm<sup>2</sup>.

**KEYWORDS:** titanium, titanium alloys, dispersion hardening, high-temperature pseudo- $\alpha$  titanium alloy, argon-arc welding, structure, properties, strength

## INTRODUCTION

Alloys based on titanium have a high specific strength in the temperature range of up to 400 °C. Titanium alloys intended for use at elevated temperatures, such as VT3, VT9, VT8, belong to the group of pseudo- $\alpha$  alloys. In recent years, investigations are carried out in two directions — development of two-phase high-temperature ( $\alpha + \beta$ )-titanium alloys, and a further improvement of the properties of existing pseudo- $\alpha$  alloys [1]. For example, the new high-temperature VT25U alloy [2] has the value of indices  $\sigma_t = 1080$  MPa at 20 °C and  $\sigma_y = 784$  MPa at 550 °C [3]. One of the ways of a further increase in the operating temperature of pseudo- $\alpha$  titanium alloys is additional doped by silicon [4, 5]. A significant disadvantage of titanium alloys doped by silicon is the difficulty of their welding, which is predetermined by the formation of cold cracks in welded joints. Therefore, welding of such alloys requires the use of additional technological operations, such as local heat treatment and preheating, and it is recommended to perform welding with an electron beam (EBW) [6].

Argon-arc welding with a tungsten electrode (AAW) or TIG-welding has become the most widely

used in industry due to the fact that this method of welding is cheap and versatile [7]. The advantage of AAW over MIG welding is that the process can be performed without the use of filler metal [8], as well as by through penetration [9]. Since it was shown in [10] that in the case of EBW of alloys doped by silicon, the best set of properties is in the joints produced with the preheating and therefore, it is advisable to investigate the possibility of AAW with the use of preheating of high-temperature alloys doped by silicon, and compare the properties of joints produced by AAW and EBW.

The aim of the work is to determine the effect of preheating on the structure and properties of welded joints produced by argon-arc welding with a tungsten electrode (AAW) using preheating to 200 and 400 °C of an experimental high-temperature pseudo- $\alpha$  titanium alloy doped by silicon.

## MATERIAL AND PROCEDURE OF INVESTIGATIONS

The structure and properties of welded joints produced by AAW of pseudo- $\alpha$  titanium alloy of Ti–5.6Al–2.2Sn–3.5Zr–0.4Mo–1.0V–0.6Si system were studied. In this work, preheating of joints to the temperatures of 200 and 400 °C was used. A temperature of 400 °C is the limit temperature at which oxidation of parts of high-temperature titanium alloys does not occur.

Melting of the ingot was carried out in the ISV-004 electron-beam equipment [11]. The chemical composition of the alloy is given in Table 1. The alloy has a  $\beta$ -phase stabilization coefficient  $K_\beta = 0.1$ . The produced ingot was rolled to a thickness of 13 mm. After rolling, to stabilize the structure and relieve stresses,

**Table 1.** Chemical composition of a high-temperature pseudo- $\alpha$  titanium alloy

Content of alloying elements, wt. %						Content of impurities, wt. %		$K_\beta$
Al	Sn	Zr	Mo	V	Si	[O]	[N]	
5.64	2.20	3.53	0.43	0.95	0.56	0.09	0.02	0.6



**Table 2.** Modes of one-sided AAW with through penetration of a high-temperature pseudo- $\alpha$  titanium Ti–5.6Al–2.2Sn–3.5Zr–0.4Mo–1.0V–0.6Si alloy

Mode number	Welding current, $I_w$ , A	Arc voltage, $U_a$ , V	Welding speed, $v_w$ , m/g	Length of the arc is preset, $L_a$ , mm	Preheating temperature $T_{pr}$ , °C
1	330	12	8	2	200
2	320	12	8	2	400
3 (over the flux)	400	12	16	2	200

**Table 3.** Parameters of welds of 8 mm thick samples of a high-temperature pseudo- $\alpha$  titanium Ti–5.6Al–2.2Sn–3.5Zr–0.4Mo–1.0V–0.6Si alloy, produced by AAW

Mode number	Width of the weld at the top, mm	Width of the weld at the bottom, mm	Weld area, mm <sup>2</sup>	HAZ width, mm	Weld + HAZ area, mm <sup>2</sup>
1	15.8	4.6	80.4	21.4	176.5
2	20.9	1.6	81.1	26.1	227.4
3 (over the flux)	8.8	3.5	55.6	14.7	113.2

the plates were subjected to annealing at a temperature of 800 °C for 1 h.

The annealed plates were treated in order to remove the oxidized layer to a thickness of 8 mm. AAW of samples with a total size of 150×80×8 mm was performed. Welding was carried out on one side in a one pass by through penetration without filler wire. Preheating during welding was performed by tungsten spirals fixed on a protective backup plate on the reverse side of the samples. A protective backup plate also performs the function of protecting the reverse side of the joint during welding and cooling of the weld metal. With this purpose, a heated shielding gas — argon is supplied to a backup plate during welding. The control of preheating temperature was carried out with the use of thermocouples attached to the facial side of the joint. The modes of one-sided argon-arc welding with a tungsten electrode by through penetration of a high-temperature titanium pseudo- $\alpha$  Ti–5.6Al–2.2Sn–3.5Zr–0.4Mo–1.0V–0.6Si alloy are given in Table 2.

## EXPERIMENTAL STUDIES

The complete welding of 8 mm thick samples occurs during AAW without the flux by through penetration at a welding current of 320–330 A and a welding speed of 8 m/h (see Table 2). Welding with the preheating provides a slight reduction in welding current to 320A. AAW over the flux (mode No. 3) by means of constriction of the argon arc provides a significant reduction in heat input of welding and increases the welding speed while providing a full penetration of 8 mm thick metal.

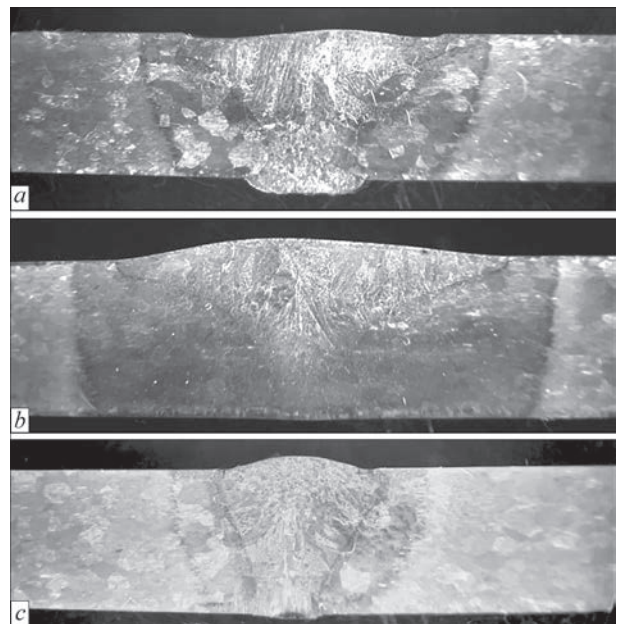
Transverse macrosections of welded joints of a high-temperature pseudo- $\alpha$  titanium alloy with dispersion hardening, performed by AAW with the preheating to 200 and 400 °C, are shown in Figure 1.

The parameters of the produced welds are given in Table 3. The weld area in AAW over the flux is

by 30 % lower than in AAW by through penetration. Thus, AAW over the flux allows performing welding of the titanium pseudo- $\alpha$  Ti–5.6Al–2.2Sn–3.5Zr–0.4Mo–1.0V–0.6Si alloy on the modes with a minimum heat input and transverse area of the weld and HAZ metal.

## RESULTS OF INVESTIGATIONS

The study of the microstructure of the produced welded joints produced made it possible to establish that in the state after rolling, the base metal of the alloy has a lamellar structure (Figure 2, *a, b*), consists of coarse primary grains (Figure 2, *a*) with a fringe fragmented during rolling, in which, after cooling of a rolled metal to the temperatures below  $T_{pr}$ , the  $\beta$ -phase de-


**Figure 1.** Transverse macrosections of welded joints of 8 mm thickness of a high-temperature pseudo- $\alpha$  titanium Ti–5.6Al–2.2Sn–3.5Zr–0.4Mo–1.0V–0.6Si alloy: *a* — AAW with the preheating to 200 °C (mode No. 1); *b* — AAW with the preheating to 400 °C (mode No. 2); *c* — AAW over the flux with the preheating to 200 °C (mode No. 3)



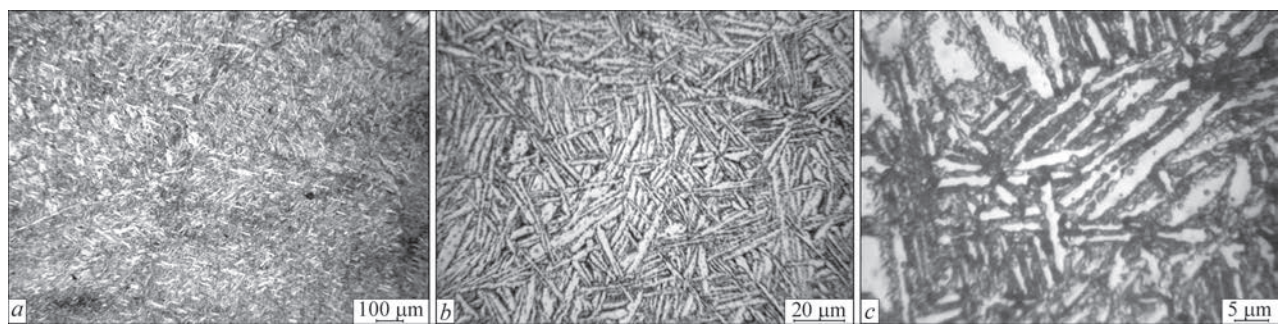


**Figure 2.** Microstructure of base metal of a high-temperature pseudo- $\alpha$  titanium Ti-5.6Al-2.2Sn-3.5Zr-0.4Mo-1.0V-0.6Si alloy (description *a-c* see in the text)

cay occurred with the formation of  $\alpha$ -phase plates, which form a basket-weave structure (Figure 2, *b*). The length of the plates is 5–30  $\mu\text{m}$ , the thickness is 1–5  $\mu\text{m}$ . At a higher magnification, it is seen that within the boundaries of  $\alpha$ -plates (Figure 2, *c*) and within the boundaries of primary grains, a precipitation of a large amount of dispersed particles of up to 1  $\mu\text{m}$  in size occurs. These dispersed particles are titanium silicide  $(\text{Ti}, \text{Zr})_5\text{Si}_3$ , since the content of silicon in the alloy exceeds the limit of its solubility in  $\alpha$ -titanium, which amounts to 0.12–0.45 % of silicon [12]. The particles of silicides are located relatively

uniformly within the boundaries of primary  $\beta$ -grains (Figure 2, *c*).

Dispersed particles of silicides are located rather uniformly and do not form a visible pattern. On the distribution maps, the elements are also located rather uniformly without a visible pattern (Figure 3, *a-g*). However, on the spectra obtained when the microprobe is passing along the line through the particles, it is seen that at the places of the particle location, the concentration of silicon and zirconium grows (Figure 4, *a-c*) and the concentration of aluminium, tin, molybdenum and vanadium decreases (Figure 4, *d-f*). This again

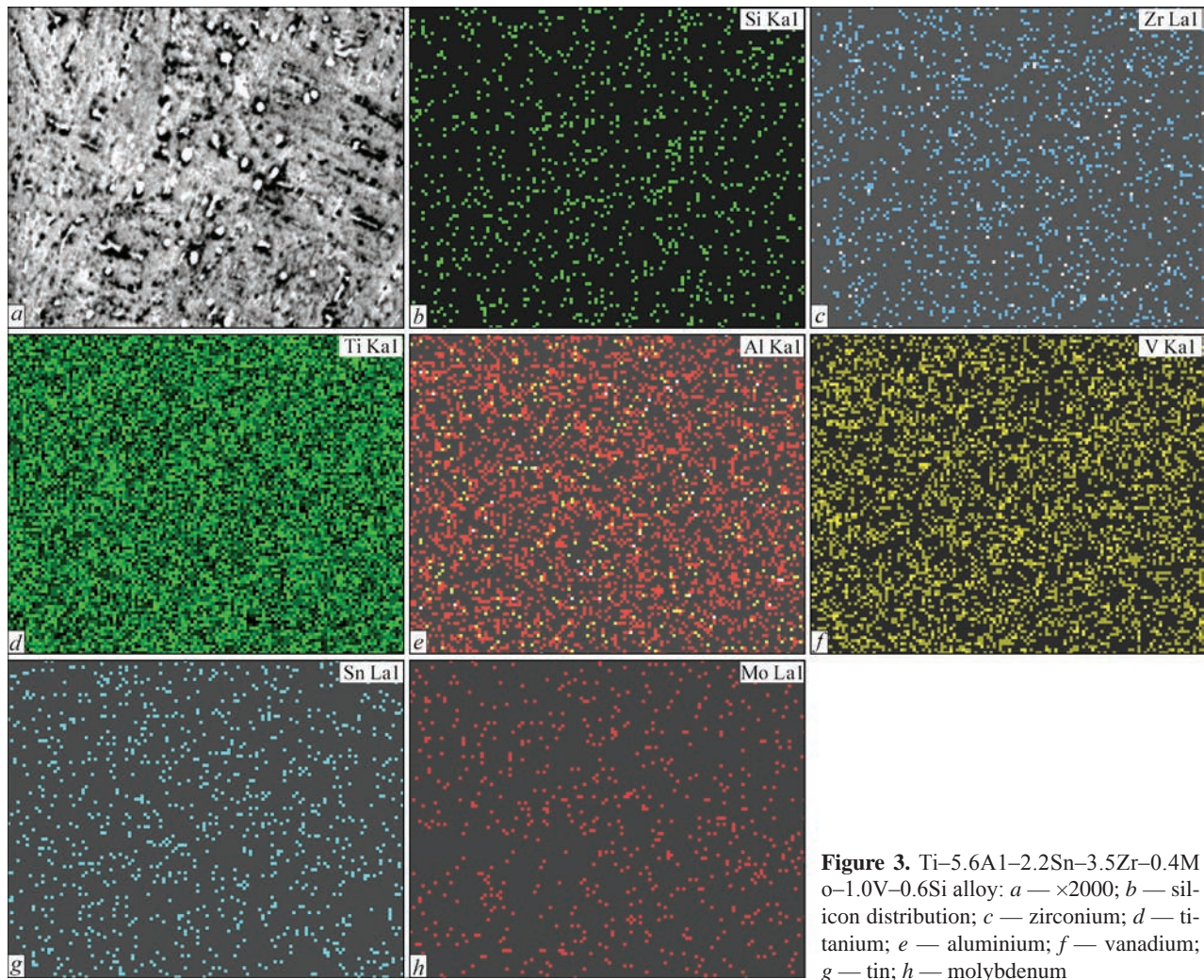


**Figure 3.** Ti-5.6Al-2.2Sn-3.5Zr-0.4Mo-1.0V-0.6Si alloy: *a* —  $\times 2000$ ; *b* — silicon distribution; *c* — zirconium; *d* — titanium; *e* — aluminium; *f* — vanadium; *g* — tin; *h* — molybdenum



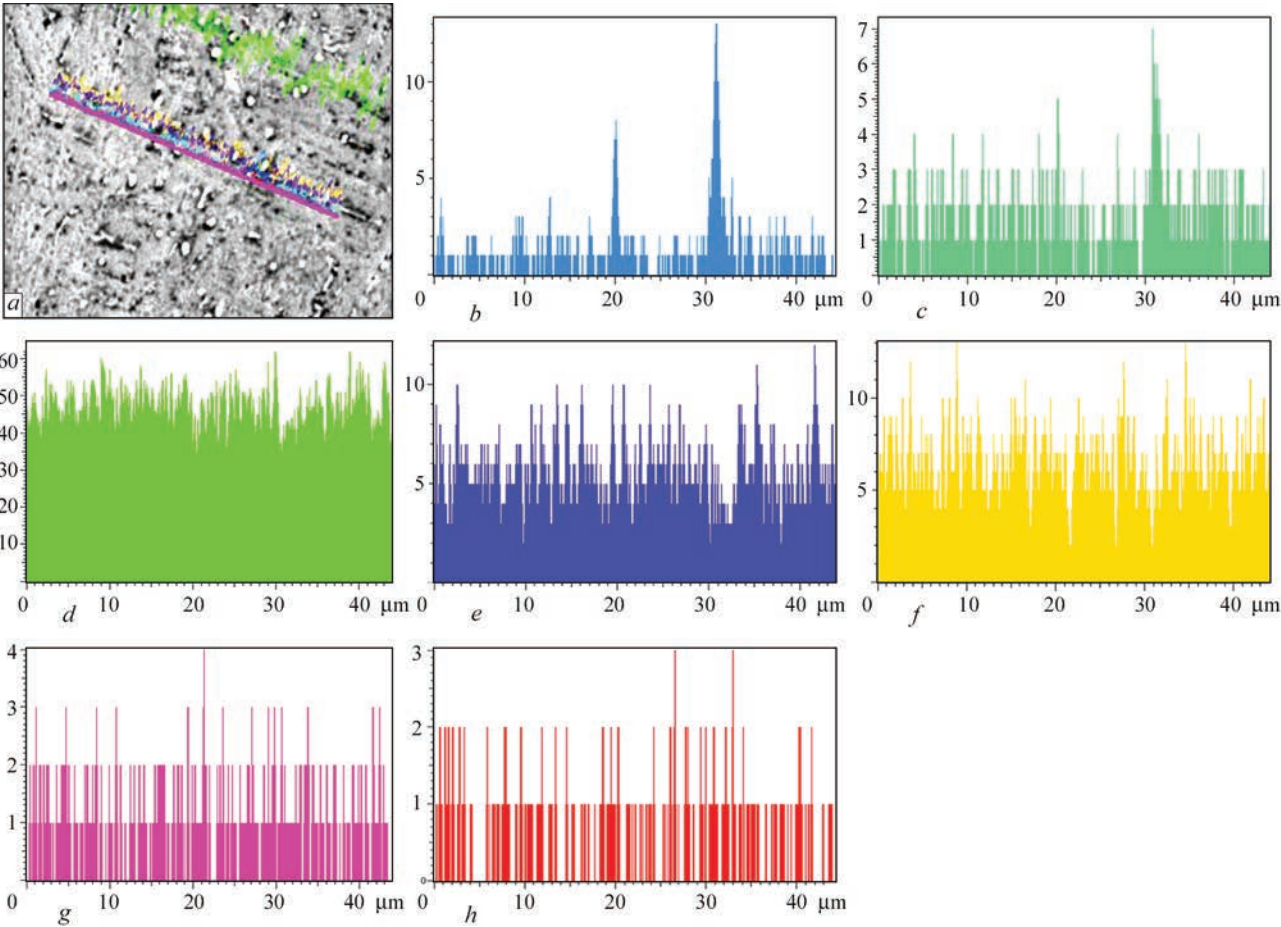


**Figure 4.** Ti-5.6Al-2.2Sn-3.5Zr-0.4Mo-1.0V-0.6Si alloy: *a* —  $\times 2000$ ; *b* — spectrum of silicon; *c* — zirconium; *d* — titanium; *e* — aluminium; *f* — vanadium; *g* — tin; *h* — molybdenum

indicates that this alloy should contain complex compounds of the type  $(\text{TiZr})_5\text{Si}_3$  or  $(\text{TiZr})_6\text{Si}_3$ .

The weld metal of the welded joint produced by AAW with the preheating to 400 °C consists of pri-

mary grains elongated in the direction of heat removal (Figure 5, *a*). The intragranular microstructure of the weld metal belongs to the same type as the microstructure of BM. The difference is in the size of

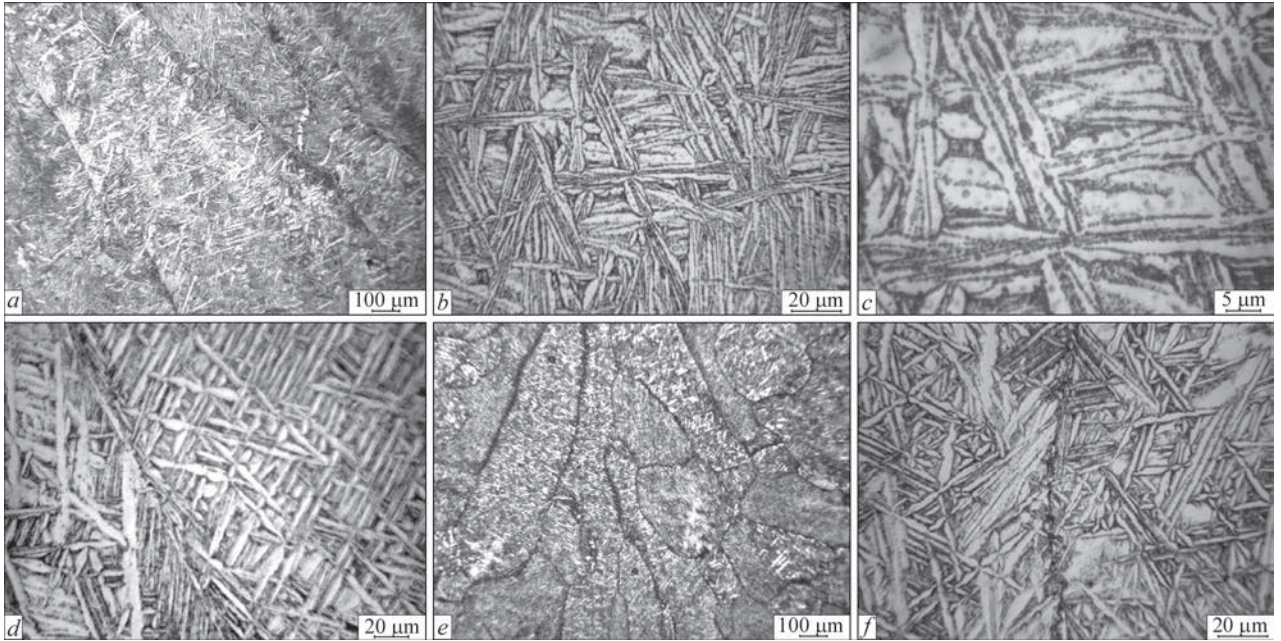


**Figure 5.** Microstructure of weld metal of joints of a high-temperature pseudo- $\alpha$  titanium Ti-5.6Al-2.2Sn-3.5Zr-0.4Mo-1.0V-0.6Si alloy, produced by AAW in the state after welding: *a-c* — mode No. 2 (400 °C); *d* — No. 1 (200 °C); *e, f* — No. 3 over the flux (200 °C)



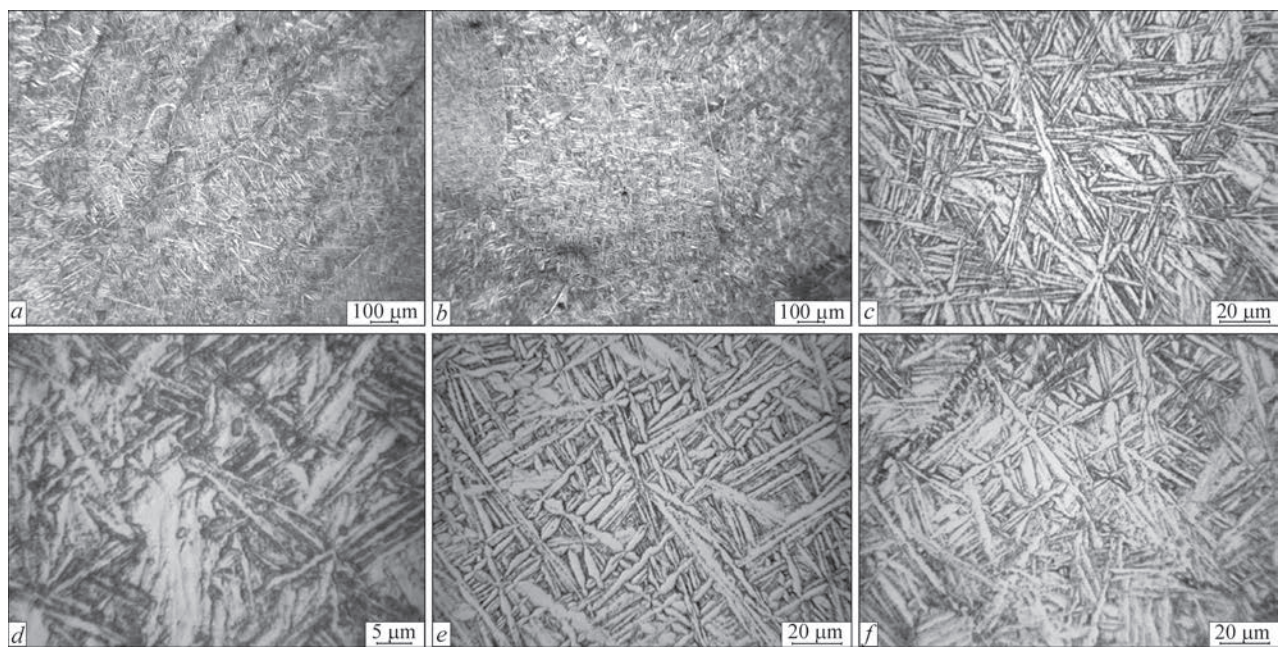


**Figure 6.** Microstructure of metal of HAZ joints of a high-temperature pseudo- $\alpha$  titanium Ti-5.6Al-2.2Sn-3.5Zr-0.4Mo-1.0V-0.6Si alloy, produced by AAW in the state after welding: *a–c* — mode No. 3 (400 °C); *d, e* — No. 2 (200 °C); *f* — No. 4 over the flux (200 °C)

the formed  $\alpha$ -plates, their length in the weld metal is somewhat larger, it is mainly 5–60  $\mu\text{m}$  (Figure 5, *b, c*), although certain plates can be found, whose length exceeds 100  $\mu\text{m}$ . Dispersed particles, which are titanium silicide, are also localized in the weld metal at the boundaries of grains and plates (Figure 5, *c*),  $\beta$ - or  $\alpha$ -phase of other degree of alloying present in the pseudo- $\alpha$  alloys is also localized there.

The microstructure of the weld metal of the welded joint produced by AAW with the preheating to 200 °C is identical to the microstructure of the weld metal produced with the preheating to 400 °C. The basket-weave structure in the weld metal produced on the mode No. 1 is formed by  $\alpha$ -plates, the length and thickness of which correspond to these parameters in the weld metal produced on the mode No. 2. The plates of a large length exceeding 100  $\mu\text{m}$  are observed here (Figure 5, *d*). The distribution and sizes of dispersed particles of  $\text{Ti}_5\text{Si}_3$  titanium silicide in the weld metal are similar to those in the weld of the joint considered above.

The microstructure of the weld metal of the joint produced by AAW over the flux with the preheating to 200 °C is shown in Figure 5, *e, f*. As is seen on the abovementioned images, the type of intragranular microstructure of the weld metal of this joint, parameters and nature of the distribution of structural components coincide with the corresponding structural elements of the weld metal produced by AAW without application of fluxes. Therefore, the use of a flux in the welding process did not affect the intragranular microstructure of the weld metal of a high-temperature pseudo- $\alpha$  titanium Ti-5.6Al-2.2Sn-3.5Zr-0.4Mo-1.0V-0.6Si alloy. Obviously, the use of a flux only affected the size of the zones in the welded joint.

In the fusion zone of the joints produced by AAW with the preheating to 400 °C, it can be seen how the large equilibrium grains of the HAZ near-weld zone are replaced by the elongated grains of the weld metal (Figure 6 *a, b*); the intragranular structure of the near-weld zone, BM and weld metal are similar. The length of the plates is 5–30  $\mu\text{m}$ , the thickness is 1–5  $\mu\text{m}$  (Figure 6, *c*). The distribution of dispersed particles and

**Table 4.** Mechanical properties of joints of a high-temperature pseudo- $\alpha$  titanium Ti-5.6Al-2.2Sn-3.5Zr-0.4Mo-1.0V-0.6Si alloy, produced by AAW and EBW with the preheating

Mode number	Preheating temperature, °C	Ultimate tensile strength $\sigma_t$ , MPa	Yield strength $\sigma_y$ , MPa	Relative elongation $\delta_s$ , %	Impact toughness KCV, J/cm <sup>2</sup>	Notes
Base metal	—	1208.2	1106.4	—	9.05	—
AAW mode No. 1	200	778.4	564.1	15.2	7.2	Fracture of MI12 samples over the weld
AAW mode No. 2	400	1160.1	—	—	8.3	Same
EBW	200	1187.6	—	—	5.4	—
EBW	400	1192.0	—	—	4.4	—

its sizes correspond to those in BM and the weld (Figure 6, *d*). In general, the microstructure of the metal of the near-weld zone of the welded joint, produced by AAW with the preheating to 200 °C (Figure 6, *e*), and welding over the flux (Figure 6, *f*), are completely identical to the microstructure of the near-weld zone of the welded joint, produced by AAW with the preheating to 400 °C.

The determination of mechanical properties of the produced welded joints allowed making a conclusion that the highest strength is in the joints produced with the preheating to 400 °C (Table 4) and is at the level of 96 % of the strength of the base metal.

The strength of the welded joints of Ti–5.6Al–2.2Sn–3.5Zr–0.4Mo–1.0V–0.6Si alloy, produced by AAW with the preheating to 200 °C is lower than the strength of the joints made with the preheating to 400 °C and amounts to 64 % of the strength of the base metal with almost equal impact toughness of the samples with a sharp notch. An increase in the preheating temperature from 200 to 400 °C has a favourable effect on the properties of the welded joints and leads to a slight increase in the impact toughness of the joints. It should be noted that the fracture of the samples of the type MI-12 at static tension occurred over the weld metal.

## DISCUSSION OF INVESTIGATION RESULTS

It is necessary to note the similarity of intragranular microstructures of different zones, such as base metal, weld metal and HAZ metal of each of the considered welded joints. A uniform homogeneous structure should guarantee close properties not only of different zones of one and the same area of a welded joint, but also of all the three considered welded joints. Thus, the analysis of the microstructure of all zones of welded joints allows making a conclusion that the preheating temperature before welding in the range of 200–400 °C does not affect the final microstructure of welded joints of a high-temperature pseudo- $\alpha$  Ti–5.6Al–2.2Sn–3.5Zr–0.4Mo–1.0V–0.6Si alloy after welding.

If we compare the joints produced by AAW with the joints produced by EBW with the preheating [10], it can be concluded that the strength of the welded joints of Ti–5.6Al–2.2Sn–3.5Zr–0.4Mo–1.0V–0.6Si alloy produced by AAW with the preheating to 400 °C, amounts to 97 % of the strength of the joints made by EBW with the preheating to 400 °C [10]. However, the impact toughness of the samples with a sharp notch of the joints produced by AAW is almost twice higher and amounts to 8.3 J/cm<sup>2</sup> (Table 4).

For the welded joints of Ti–5.6Al–2.2Sn–3.5Zr–0.4Mo–1.0V–0.6Si alloy, produced by EBW, an increase in the preheating temperature from 200 to 400 °C

has no favourable effect on the properties of welded joints and leads to a decrease in the impact toughness of the joints of both alloys. For the joints of this alloy produced by AAW, an increase in the preheating temperature from 200 to 400 °C leads to an increase in the strength and impact toughness.

The conducted investigations made it possible to conclude that for AAW of a high-temperature pseudo- $\alpha$  Ti–5.6Al–2.2Sn–3.5Zr–0.4Mo–1.0V–0.6Si alloy, the optimum preheating temperature is 400 °C. In this case, the strength of welded joints is not less than 90 % of the strength of the base metal. The values of the impact toughness of the samples with a sharp notch (8.3 J/cm<sup>2</sup>) are close to the indices for the base metal (9.0 J/cm<sup>2</sup>).

## CONCLUSIONS

1. The weld metal of a high-temperature pseudo- $\alpha$  Ti–5.6Al–2.2Sn–3.5Zr–0.4Mo–1.0V–0.6Si alloy after welding has a basket-weave structure from the plates of  $\alpha$ -phase, the length of plates is 5–30  $\mu$ m, the thickness is 1–5  $\mu$ m, and dispersed particles of titanium silicide and  $\beta$ -phase are localized on the boundaries of grains and plates.

2. The preheating temperature before welding in the range of 200–400 °C does not affect the final microstructure of welded joints of a high-temperature pseudo- $\alpha$  Ti–5.6Al–2.2Sn–3.5Zr–0.4Mo–1.0V–0.6Si alloy produced by AAW in the state after welding.

3. The highest ultimate strength is in the AAW-joints of a high-temperature pseudo- $\alpha$  Ti–5.6Al–2.2Sn–3.5Zr–0.4Mo–1.0V–0.6Si alloy, produced with the preheating to 400 °C, which is on the level  $\sigma_t = 1160.1$  MPa and corresponds to 96 % of the strength of the base metal and 97 % of the strength of the joints made by EBW with the preheating to 400 °C, the index of impact toughness of the samples with a sharp notch of the joints produced by AAW is twice higher and amounts to 8.3 J/cm<sup>2</sup>.

## REFERENCES

1. Mukhin, V.S. (2007) *Fundamentals of mechanical engineering technology (aircraft engine building)*. Ufa, UGATU [in Russian].
2. Iliencko, V.M., Shalin, R.E. (1995) Titanium alloys for aircraft gas turbine engines. *Titan (VILS)*, 1–2 [in Russian].
3. Iliin, A.A., Kolachev, B.A., Polkin, I.S. (2009) *Titanium alloys. Composition, structure, properties*: Handbook. Moscow, VILS MATI [in Russian].
4. Ivanov, V.I., Yasinsky, K.K. (1996) Efficiency of application of high-temperature alloys based on intermetallics Ti<sub>3</sub>Al and TiAl for operation at 600–800 °C temperatures in aerospace engineering. *Tekhnologiya Lyogkikh Splavov*, 3.
5. Solonina, O.P., Glazunov, S.G. (1996) *High-temperature titanium alloys*: Handbook. Moscow, Metallurgiya [in Russian].
6. Makarov, E.L. (1981) *Cold cracks in welding of alloyed steels*. Moscow, Mashinostroenie [in Russian].

7. Akhonin, S.V., Belous, V.Yu. (2017) Argon-arc welding of titanium and its alloys using fluxes (Review). *The Paton Welding J.*, **2**, 7–12. DOI: <https://doi.org/10.15407/tpwj2017.02.02>
8. Guseva, E.A., Klimychev, A.I. (1997) Through penetration argon-arc welding of titanium alloys. *Svarochn. Proizvodstvo*, **2**, 15–16 [in Russian].
9. Gurevich, S.M. (1990) *Handbook on welding of nonferrous metals*. Kyiv, Naukova Dumka [in Russian].
10. Akhonin, S.V., Vrzhezhevsky, E.L., Belous, V.Yu., Petrichenko, I.K. (2017) Influence of preheating parameters and local heat treatment on structure and properties of dispersion-strengthened joints of silicon-containing titanium alloys made by electron beam welding. *The Paton Welding J.*, **7**, 43–47. DOI: <https://doi.org/10.15407/tpwj2017.07.09>
11. Levitsky, N.I., Matvinets, E.A., Lapshuk, T.V. et al. (2012) Producing of complex titanium alloys by method of electron beam skull melting. *Metall i Litio Ukrainy*, **4**, 6–9 [in Russian].
12. Anoshkin, N.F., Sigalov, Yu.M. (2002) Titanium alloys with higher heat resistance. *Tekhnologiya Lyogkikh Splavov*, **1**, 38–50 [in Russian].

## ORCID

S.V. Akhonin:0000-0002-7746-2946,

V.Yu. Bilous:0000-0002-0082-8030,  
R.V. Selin: 0000-0002-2990-1131,  
I.K. Petrychenko: 0000-0002-0476-3983

## CONFLICT OF INTEREST

The Authors declare no conflict of interest

## CORRESPONDING AUTHOR

S.V. Akhonin

E.O. Paton Electric Welding Institute of the NASU  
11 Kazymyr Malevych Str., 03150, Kyiv, Ukraine.

E-mail: akhonin.sv@gmail.com

## SUGGESTED CITATION

S.V. Akhonin, V.Yu. Bilous, R.V. Selin,  
I.K. Petrychenko, L.M. Radchenko,  
S.B. Rukhanskyi (2022) Argon-arc welding of  
high-temperature titanium alloy doped by silicon.  
*The Paton Welding J.*, **5**, 26–32.

## JOURNAL HOME PAGE

<https://pwj.com.ua/en>

Received: 15.04.2022

Accepted: 08.08.2022



## FEATURES OF THE STRUCTURE OF MOLYBDENUM–KOVAR BRAZED JOINTS

S.V. Maksymova, P.V. Kovalchuk, V.V. Voronov

E.O. Paton Electric Welding Institute of the NASU

11 Kazymyr Malevych Str., 03150, Kyiv, Ukraine

### ABSTRACT

The work presents the results of metallographic and X-ray microspectral studies of molybdenum–Kovar overlap joints, which were produced by vacuum brazing with application of brazing filler metal based on Cu–Mn–Co system. The influence of soaking at brazing temperature on brazed seam structure formation was studied. Local X-ray microspectral analysis was used to determine the number of structural components of the brazed seam: copper-based solid solution, individual single iron-based grains, reaction layer in the form of a continuous band on molybdenum–brazing filler metal interface. It was found that longer soaking at the brazing temperature promotes an increase of the reaction layer width from 1 to 3  $\mu\text{m}$  and leads to formation of a faceted morphology from the brazed seam side and to microcracks initiation in it, but it does not affect molybdenum concentration, which at different soaking (1–15 min) is in the range of 55.81–59.05 wt.%. In the solid solution (matrix) manganese concentration decreases with longer soaking, copper concentration rises, but the quantity of iron practically does not change, and it is in the range of 4.52–4.95 wt.%. In single grains of the dark phase, observed near the interface with Kovar, longer soaking promotes an increase of iron and nickel concentration and lowering of manganese and copper content.

**KEYWORDS:** Kovar, molybdenum, vacuum brazing, brazing filler metal, structure, brazed seam, soaking, reaction layer, X-ray microspectral analysis

### INTRODUCTION

Under the conditions of modern industry, alloys with specified physical characteristics have become widely applied as individual brazed assemblies, which are the components of different structures. Special attention is attracted by dissimilar brazed joints, for instance, molybdenum–Kovar pair. Molybdenum is an important structural material of electrovacuum, rocket, aviation, and nuclear power engineering. A successful combination of a complex of valuable physico-mechanical and corrosion properties makes this metal one of the main high-tech structural materials [1–3]. It is rather difficult to join molybdenum and Kovar, because of the difference in their chemical composition and physico-mechanical properties. As is known, there exist different methods of joining this pair of materials: diffusion, electron beam and laser welding [3–5], but the technology of joining these materials by vacuum brazing became the most widely applied.

Molybdenum brazing runs into problems, because of its high affinity to oxygen, as well as its proneness to grain growth at high temperature. Molybdenum recrystallization temperature (850–1220  $^{\circ}\text{C}$ ) depends on many factors and, primarily, on the purity and degree of deformation. At transition through the recrystallization threshold, molybdenum becomes brittle, which should be taken into account at selection of the filler metal for its brazing. In addition, molybdenum has a small temperature coefficient of linear expansion ( $\alpha = 5.6 \cdot 10^{-6} \text{ }^{\circ}\text{C}^{-1}$ ) which distinguishes it from

metals and alloys, with which it is usually joined at brazing (copper, nickel, iron, etc.) [6].

Considerable problems arise at brazing of dissimilar materials [7, 8]. At their brazing copper [2], copper–titanium [9] and ductile silver brazing filler metals [10] are used as brazing materials.

At brazing temperature the brazing filler metal should wet both the base materials equally well, otherwise it will spread over the surface of one of the materials, which is better wetted, instead of filling the brazing gaps. Molybdenum and iron (which is a Kovar component) have considerable areas of solubility at high temperature, but at temperature lowering these areas quickly become narrower and at room temperature the mutual solubility is practically absent [11]. Between the considered elements, there is a number of intermetallic phases, which have a negative role, leading to brittleness of both the welded and brazed joints [5, 8]. Therefore, studying structure formation on molybdenum–brazing filler metal–Kovar interface is highly important when producing molybdenum–Kovar dissimilar permanent joints.

The objective of this work is studying the influence of soaking time on brazed seam structure formation and reaction layer width at brazing of molybdenum–Kovar dissimilar joints (with application of a brazing filler metal of copper–manganese system) in vacuum.

### EXPERIMENTAL PART

Used as base metal were plates of 12Kh18N10 stainless steel (Fe–(17–18)Cr–(8.0–10)Ni– $\leq 2.0\text{Mn}$ – $\leq$

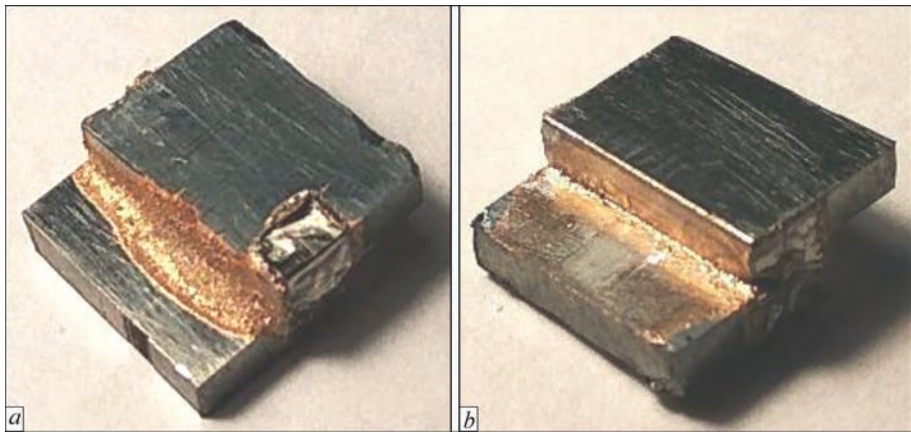


**Figure 1.** Appearance of dissimilar molybdenum–Kovar brazed joint at 15 min soaking: straight (*a*) and reverse fillets (*b*)

$\leq 0.8\text{Si}$ – $\leq 0.12\text{C}$ ), characterized by high anti-corrosion properties, precision Kovar alloy of 29NK grade (Fe–29Ni–17Co) and brazing filler metal of copper–manganese system (Cu–Mn–4.5Co) with the structure of solid solution. The latter was obtained by melting in a laboratory installation in a shielding atmosphere of argon, and it was used in the cast state in the form of pieces (of not more than 2 mm size). Before brazing the surfaces of materials to be joined were ground on a diamond disc with 125  $\mu\text{m}$  granularity.

Brazing dissimilar overlap joints (with a capillary gap) was conducted in a vacuum furnace with radiation heating at a temperature exceeding the liquidus temperature ( $T_l = 966\text{ }^\circ\text{C}$ ) of the brazing filler metal by 30  $^\circ\text{C}$ , soaking time was 1, 3 and 15 min. Obtained samples were cut normal to the plate surface, macro-sections were prepared by a standard procedure and chemical inhomogeneity was studied in a scanning electron microscope TescanMira 3 LMU. Micro-X-ray spectral studies and determination of local distribution of elements in the individual phases were conducted with application of energy-dispersive spectrometer “Oxford Instruments X-max 80 mm<sup>2</sup>”, fitted with INCA software. Microsections were examined without chemical etching [12]. Hardness was studied

using PMT-3 microhardness meter with loading  $P = 50\text{ g}$  ( $\tau = 0.15\text{ min}$ ).

**EXPERIMENTAL RESULTS AND THEIR ANALYSIS**

Dense brazed lines (Figure 1, *a*) and reverse fillet areas (Figure 1, *b*) form at brazing overlap dissimilar molybdenum–Kovar joints.

The brazing filler metal spreads readily over the base metal and flows into the capillary gap [13]. Results of metallographic studies and X-ray microspectral analysis of molybdenum–Kovar brazed joints ( $\tau = 1\text{ min}$ ) showed that the welds are characterized by a homogeneous structure (Figure 2, *a, b*).

The brazed seam structure is represented by solid solution based on copper–manganese–nickel–cobalt system, containing a small quantity of iron (4.52 %), and it is the matrix. Moreover, individual iron-based dark grains are observed against the background of this matrix, which are weakly visualized (Table 1, spectrum 1, Figure 2, *c*).

It can be assumed that diffusion processes (or Kovar dispersion) run at brazing, and individual base metal grains (Table 1, spectrum 1, Figure 2, *c*) in the form of dark grains precipitate against the background of matrix–solid solution. With greater distance from

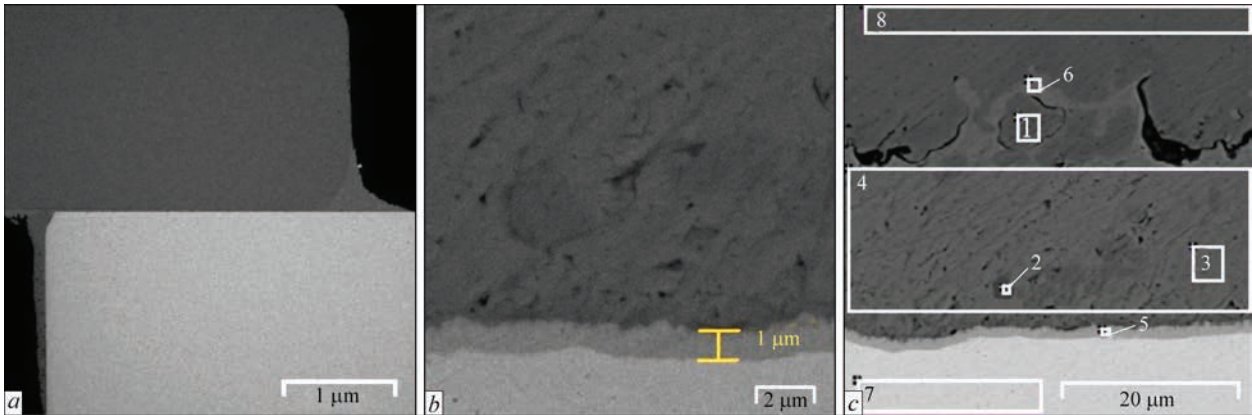


**Figure 2.** Appearance (*a*), reaction layer (*b*) and areas (*c*), where chemical heterogeneity of Mo–Kovar brazed joint ( $\tau = 1\text{ min}$ ) was determined

**Table 1.** Chemical heterogeneity of Mo–Kovar brazed joint ( $\tau = 1$  min)

Spectrum number	Chemical elements, wt.%					
	Mn	Fe	Co	Ni	Cu	Mo
1	22.12	39.49	17.62	13.50	6.42	0.85
2	29.99	28.25	21.43	5.06	10.07	5.21
3	26.53	4.52	4.41	5.37	59.17	–
4	26.33	5.71	5.02	5.15	57.79	–
5	10.25	18.26	11.80	0.69	2.57	56.42
6	24.06	8.87	5.62	9.15	52.30	–
7	–	–	–	–	0.48	99.52
8	0.69	52.79	17.75	28.77	–	–

**Table 2.** Chemical heterogeneity of Mo–Kovar brazed joint

Spectrum number	Chemical elements, wt.%					
	Mn	Fe	Co	Ni	Cu	Mo
1	–	–	–	–	–	100.00
2	8.64	19.78	11.08	1.29	2.78	56.43
3	26.51	30.35	20.89	5.62	1.06	5.56
4	26.54	28.36	18.20	7.17	19.73	–
7	24.01	4.43	3.16	5.19	63.21	–
8	23.68	10.09	6.48	6.14	52.24	1.39
9	7.76	19.97	10.98	1.17	1.07	59.05

them to Kovar, the nickel and iron concentration in these grains is reduced, and that of manganese, cobalt and copper becomes higher (Table 1, spectrum 2, Figure 2, *c*) that is indicative of their saturation by the constituent chemical elements of the brazing filler metal (or partial dissolution in the liquid brazing filler metal at brazing). It should be noted that iron concentration in the solid solution of the brazed seam, adjacent to molybdenum, does not change, remaining on the level of 4.52 %. A higher concentration of iron of 5.71 % was found, when studying the chemical composition of the solid solution in the areas which are located closer to Kovar.

From the side of molybdenum, bordering on the weld metal, a molybdenum-based layer with 56.42Mo–18.26Fe–11.80Co–10.25Mn 1μm wide is formed, which contains a small amount of copper and

nickel (Figure 2, *a–c*, Table 1, spectrum 5). Increase of soaking time at vacuum brazing from one up to three minutes leads to a light increase of its width up to 1.25–2.0 μm (Figure 3, Table 2, spectrum 2), but molybdenum concentration remains on the same level (Table 2, spectrum 2, Figure 3, *b*).

In keeping with binary constitutional diagram of Fe–Mo (Figure 4), iron and molybdenum have limited solubility and form several intermetallic phases: more stable FeMo ( $\alpha$ -phase) and  $\text{Mo}_{38}\text{Fe}_{62}$  intermetallic phases form at high temperature; two more intermetallic phases, namely  $\text{Fe}_2\text{Mo}$  and  $\text{Fe}_7\text{Mo}_6$ , form in the solid state by the peritectic reactions. A feature of high-temperature phases FeMo ( $\sigma$ -phases) and  $\text{Mo}_{38}\text{Fe}_{62}$  (R-phases) is the fact that as a result of temperature lowering they transform into  $\mu$ -phase, whose

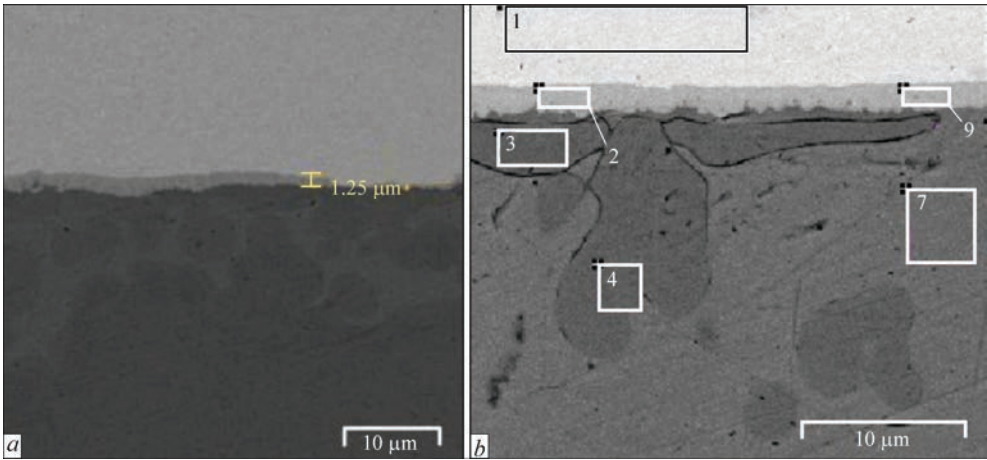


**Figure 3.** Microstructure (*a*) and electronic image (*b*) of Mo–Kovar brazed joint ( $\tau = 3$  min)



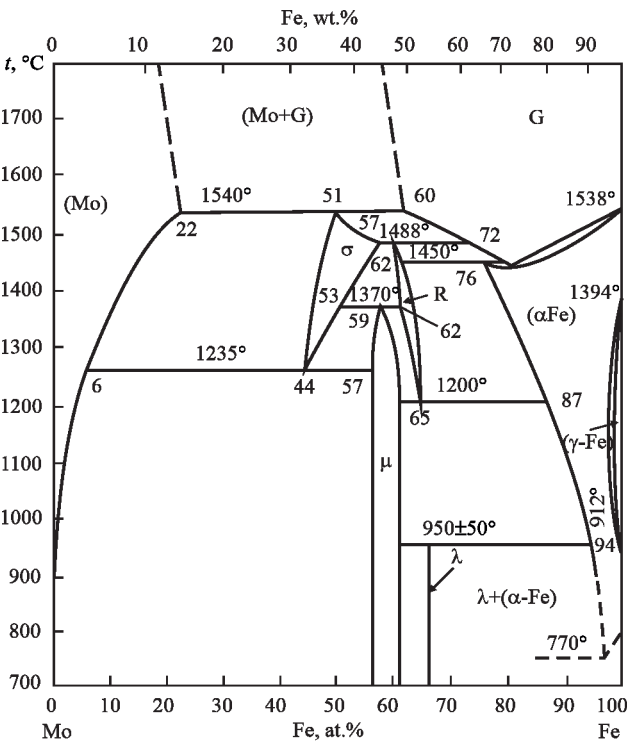


Figure 4. Binary constitutional diagram of Fe–Mo metallic system

homogeneity region is 44–58 at.% and into Mo- and  $\alpha$ Fe-based solid solutions (respectively) [11].

MoFe<sub>2</sub> compound (Laves phase) with homogeneity region of  $66.3 \pm 0.2$  at.% (at the temperature of  $950 \pm 50$  °C) forms by the peritectic reaction. Such a phase composition is characteristic for binary alloys of this system that were brought into the equilibrium state by heat treatment [11].

It should be noted that solidification of brazed seam metal runs under nonequilibrium conditions in the presence of diffusion processes and concentration gradient on base metal–brazing filler metal interface that influences the chemical composition of the brazed seam and its morphology [14]. Proceeding from the obtained results of local X-ray microspectral analysis, it can be assumed that such conditions of solidification of brazed seam metal promote formation of a complex molybdenum-based intermetallic phase of Mo<sub>56</sub>(Fe, Co, Mn, Cu, Ni)<sub>44</sub>, which is observed in the form of a continuous band — reaction layer along the brazed seam, and contains other constituent elements of the brazing filler metal and base metal, in addition to iron and molybdenum. A continuous series of solid solutions are formed by  $\gamma$ -iron and  $\alpha$ -cobalt

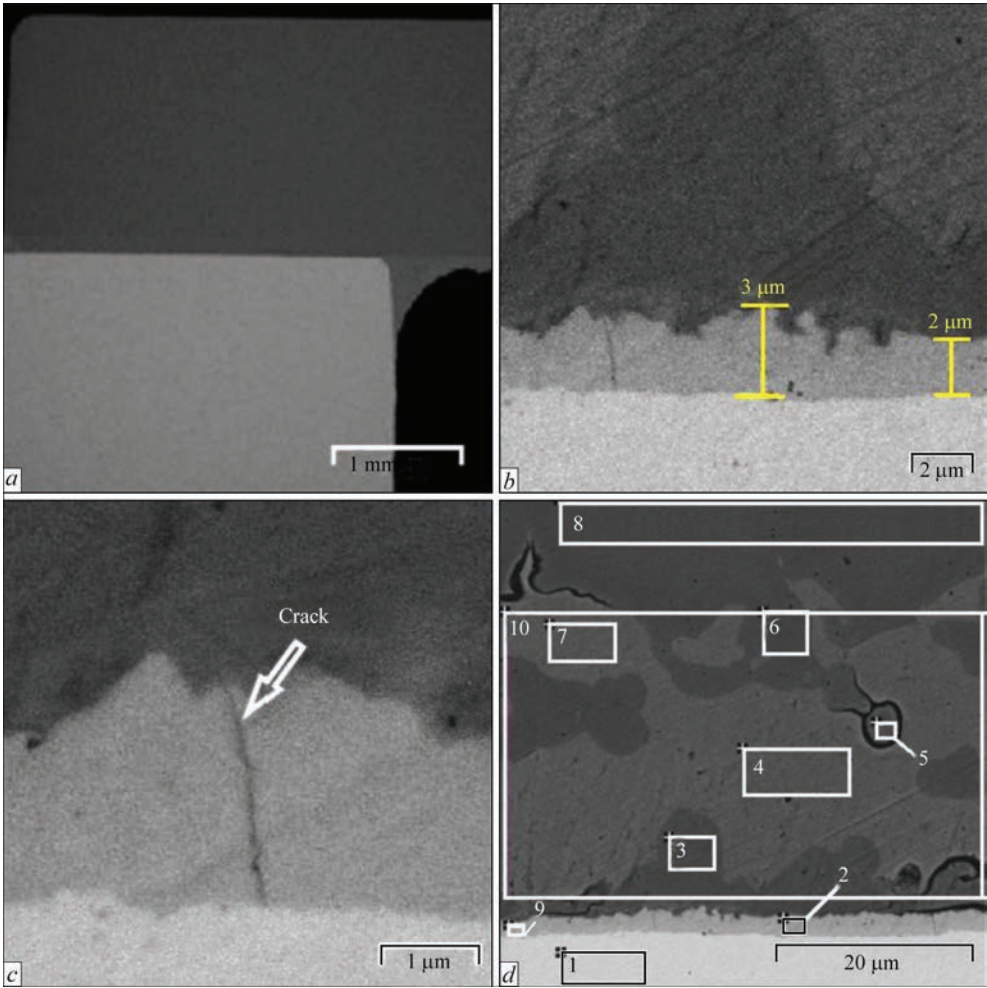


Figure 5. Appearance (a), reaction layer (b, c) and electronic image (d) of Mo–Kovar brazed joint microstructure ( $\tau = 15$  min)

**Table 3.** Chemical heterogeneity of Mo–Kovar brazed joint ( $\tau = 15$  min)

Spectrum number	Chemical elements, wt. %					
	Mn	Fe	Co	Ni	Cu	Mo
1	0.00	0.19	0.00	0.00	0.00	99.81
2	7.00	22.47	12.58	1.79	0.00	56.16
3	21.03	31.97	17.42	8.31	17.18	4.10
4	19.11	4.95	3.71	6.21	66.01	0.00
5	20.36	31.69	16.14	10.58	18.39	2.85
6	9.15	47.56	16.34	24.07	2.41	0.47
7	18.71	6.15	4.14	6.45	64.36	0.19
8	4.44	48.94	16.63	24.78	5.20	0.00
9	6.57	21.92	12.63	1.76	1.31	55.81
10	17.24	12.60	6.60	6.90	55.98	0.69

between high-temperature modifications, similar to the high-temperature region of iron-manganese binary system [11]. As to copper and nickel concentration, it is negligible in this phase and cannot have any significant influence on its properties.

Further increase of soaking time up to 15 min leads to increase of the reaction layer width within 2–3  $\mu\text{m}$  (Figure 5).

Molybdenum concentration practically does not change and remains on the same level as in the previous samples (Table 3, spectra No. 2 and No. 9). In individual areas of the reaction layer (from the brazing filler metal side) its morphology undergoes changes and it is transformed into the faceted surface (Figure 5, *b, c*).

More over, increase of soaking time leads not only to increase of its width but also to initiation of micro-cracks which propagate only in some regions of this reaction layer in the direction normal to its surface (Figure 5, *b, c*) that is indicative of its brittleness.

Concentration of constituent elements of individual phases of the brazed seam also changes (Table 3). In the solid solution manganese concentration is equal to 18.71–19.11 wt.% that is much smaller, compared to previous samples. It is obvious that at increase of the temperature of soaking at brazing temperature the high manganese vapour pressure results in its partial evaporation that leads to lowering of its concentration in the brazed seam metal (brazing filler metal).

In the dark phase iron concentration increases slightly, and it is in the range of 31.69–47.56 %, while cobalt concentration is equal to 16.34–17.42 % (Table 3). X-ray microspectral analysis proved that increase of soaking from one up to 15 min at brazing temperature of Mo–Kovar samples promotes an increase of iron, and nickel concentration and lowering of manganese and copper content in the dark phase grains located near Kovar (Figure 6).

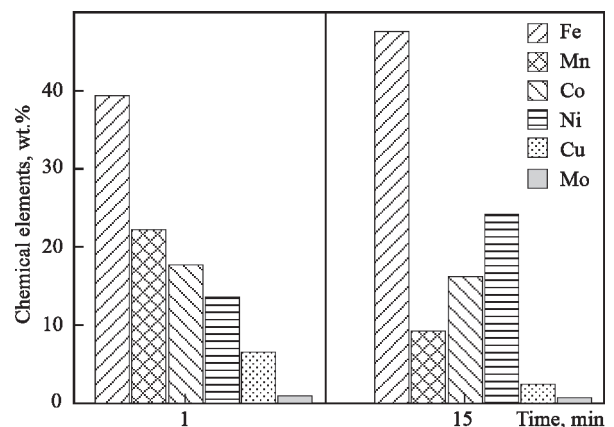
More over, it should be noted that increase of iron concentration is manifested to a greater extent in the grains of this phase, which are located closest to Ko-

var. In the grains located in the weld central zone an increase of iron concentration is also observed but it is less pronounced.

Analysis of the obtained results of X-ray microspectral analysis shows that increase of soaking time at brazing of dissimilar molybdenum–Kovar joints promotes increase of copper concentration in the solid solution–matrix of brazed seam metal, but the quantity of iron practically does not change and it is in the range of 4.52–4.95 % (Figure 7, *a*). Cobalt and nickel concentration practically does not change, and that of manganese is considerably reduced.

It follows from the conducted studies that with increase of soaking time from 1 up to 15 min the width of the reaction layer is increased (molybdenum-based phase), but molybdenum concentration remains on the same level, as at soaking for 1, 3 and 15 min (Figure 7, *b*). A slight reduction of manganese concentration with a simultaneous increase of iron concentration is observed. Such features of structure formation are due to the pattern of binary constitutional diagrams of metal systems [11] and high elasticity of manganese vapours.

Obtained data correlate well with the results of studying element distribution in the Mo–Kovar brazed joint ( $\tau = 15$  min) that are determined by scan-


**Figure 6.** Dependence of chemical element content in iron-based phase on soaking time at brazing dissimilar Mo–Kovar joints

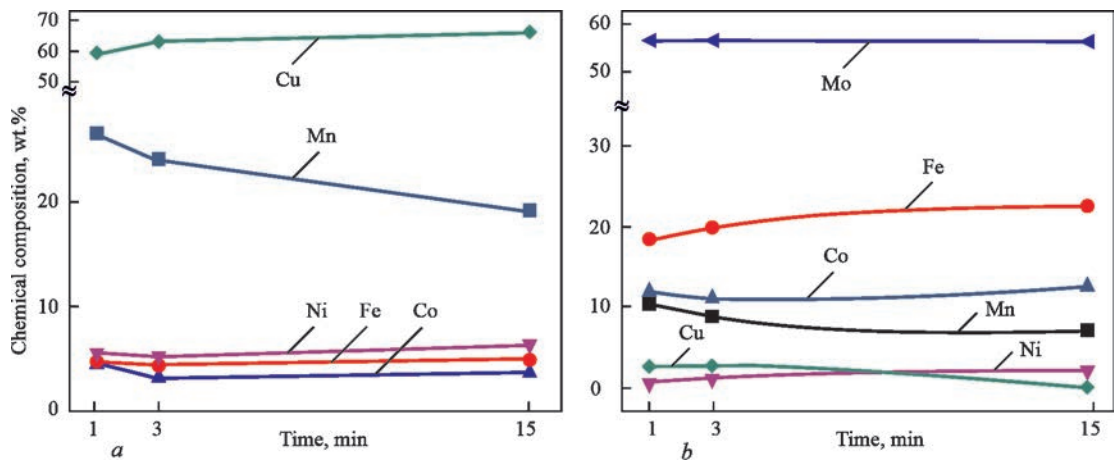


**Figure 7.** Influence of soaking time on chemical element concentration in the following phases: in the solid solution (*a*); in the reaction layer — molybdenum-based phase (*b*) at brazing dissimilar Mo–Kovar joints

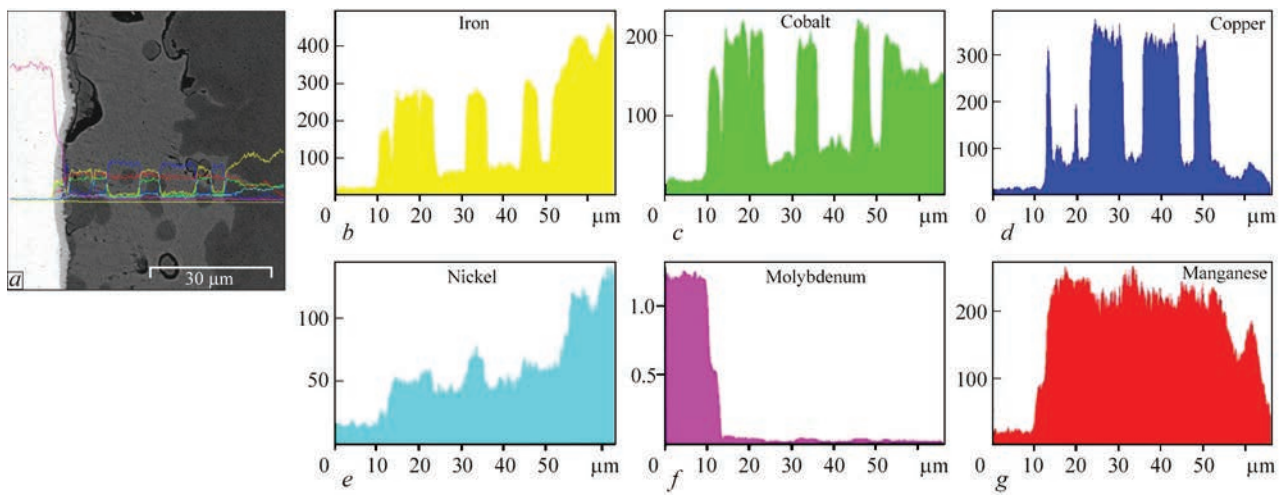


**Figure 8.** Electronic image (*a*) and qualitative distribution of elements: iron (*b*), cobalt (*c*), copper (*d*), nickel (*e*), molybdenum (*f*) and manganese (*g*) in a brazed seam of a dissimilar joint at application of brazing filler metal of Cu–Mn–4.5Co system

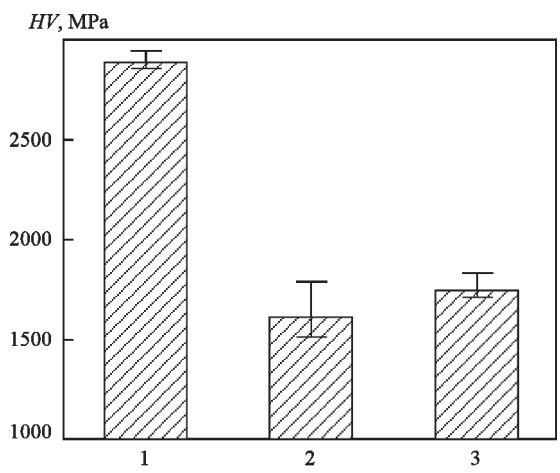


**Figure 9.** Microhardness of dissimilar molybdenum–Kovar joint: 1 — molybdenum; 2 — seam; 3 — Kovar

ning of the brazed seam cross-section by the electron beam. Presence in the weld central part of a phase based on Fe–Co–Mn system and molybdenum-based phase, which solidifies in the form of a continuous band along the brazing filler metal–molybdenum interphase, is confirmed (Figure 8).

Results of studying the brazed joints ( $\tau = 3$  min) showed that the brazed seam microhardness is characterized by essentially lower values, compared to those for molybdenum, but differs only slightly from these values for Kovar (Figure 9).

The obtained data lead to the conclusion that microhardness (*HV*) of the brazed seam (1513–1791 MPa) and Kovar (1678–1831 MPa) is in close ranges, which it can have a positive influence on the mechanical properties and relaxation of stresses, arising at brazing the dissimilar joints.

### CONCLUSIONS

X-ray microspectral studies showed that the main phase (matrix) of the brazed seam in molybdenum–Kovar joints is a copper-based solid solution, in which up to 4.95 % is dissolved. A molybdenum-based phase in the form of a continuous (reaction) layer forms along the brazing filler metal–molybdenum interphase. Moreover, individual single iron-based grains are observed, which solidify against the background of the matrix–solid solution. Increase of soaking from



1 up to 15 min promotes an increase of the concentration of iron and nickel (in the dark phase grains located near Kovar) and lowering of manganese and copper content.

In the solid solution (matrix) of brazed seam metal manganese concentration decreases with longer soaking, that of copper becomes higher, but the amount of iron practically does not change and is in the range of 4.52–4.95 %.

Local X-ray microspectral analysis proved that increase of soaking time from 1 up to 15 min at brazing molybdenum–Kovar joints promotes an increase of the width of the reaction layer, forming on molybdenum–seam metal interface, from 1 up to 3  $\mu\text{m}$ , but it does not influence its chemical composition. Molybdenum concentration at different soaking (1, 3, 15 min) is within 55.81–59.05 %. Widening of the molybdenum-based reaction layer (up to 3  $\mu\text{m}$ ) leads to formation of a faceted morphology from the side of brazed seam metal and to appearance of microcracks in it.

## REFERENCES

1. Zelikman, A.N. (1970) *Molybdenum*. Moscow, Metallurgiya [in Russian].
2. Kumar, S., Upadhyay, A., Dinesh Kumar, P., Agarwal, A. (2015) Vacuum brazing of molybdenum–Kovar and evaluation of its joint strength. *Mat. Sci. Forum*, **830–831**, 282–285. doi:10.4028/www.scientific.net/msf.830-831.282
3. Chen, G., Yin, Q., Guo, C. et al. (2019) Beam deflection effects on the microstructure and defect creation on electron beam welding of molybdenum to Kovar. *J. of Materials Proc. Technology*, **267**, 280–288. DOI: <https://doi.org/10.1016/j.jmatprotec.2018.12.017>
4. Kazakov, N.F. (1986) *Diffusion welding of materials*. Moscow, Mashinostroenie [in Russian].
5. Guoqing, C., Qianxing, Y., Zhibo, D. et al. (2021) Microstructure evolution analysis for the reaction interface between molybdenum and Kovar acquired by electron beam welding-brazing. *Materials Characterization*, **171**, 110781. DOI: <https://doi.org/10.1016/j.matchar.2020.110781>
6. Petrunin, I.E. (2003) *Handbook on brazing*. 3<sup>rd</sup> Ed. Moscow, Mashinostroenie [in Russian].
7. (2006) *Mechanical engineering. Encyclopedia: Technology of welding, brazing and cutting*. Vol. 111–4. Ed. by B.E. Paton. Moscow, Mashinostroenie [in Russian].
8. Yermolayev, G.V., Kvasnytskyi, V.V., Kvasnytskyi V.F. et al. (2015) *Soldering of materials: Manual*. Mykolaiv, NUK [in Ukrainian].
9. Kostin, A.M., Labartkava, A.I.V., Martynenko, V.A. (2014) Study of processes of interaction of titanium-containing brazing filler metals with oxide ceramics and Kovar. *Metallofiz. Noveishie Tekhnol. J.*, **36(6)**, 815–827 [in Russian].
10. Singh, M., Asthana, R., Sobczak, N. (2020) Active brazing of SiC-base ceramics to high-temperature alloys. *J. of Mater. Eng. and Perform.*, **29**, 4898–4912. DOI: <https://doi.org/10.1007/s11665-020-04934-3>
11. Lyakishev, N.P. (1997) *State diagrams of binary metallic systems: Handbook*. In: 3 Vol. Vol. 2, Moscow, Mashinostroenie [in Russian].
12. Maksymova, S.V., Voronov, V.V., Kovalchuk, P.V., Larionov, A.V. (2017) Producing dissimilar joints of molybdenum–stainless steel using vacuum brazing. *The Paton Welding J.*, **2**, 13–18. DOI: <https://doi.org/10.15407/tpwj2017.02.03>
13. Maksymova, S.V., Kovalchuk, P.V., Voronov, V.V. (2021) Vacuum brazing of Kovar–molybdenum dissimilar joints. *The Paton Welding J.*, **7**, 13–18. DOI: <https://doi.org/10.37434/tpwj2017.02.03/>
14. Maksymova S.V., Voronov V.V., Kovalchuk P.V., Larionov A.V. (2017) Influence of temperature of the brazing on structure of brazed heterogeneous molybdenum–stainless steel joints. *Metallofiz. Noveishie Tekhnol. J.*, **39(9)**, 1227–1237 [in Russian]. DOI: <https://doi.org/10.15407/mfint.39.09.1227>

## ORCID

S.V. Maksymova: 0000-0003-0158-5760,  
P.V. Kovalchuk: 0000-0002-2313-5982,  
V.V. Voronov: 0000-0002-0410-1154

## CONFLICT OF INTEREST

The Authors declare no conflict of interest

## CORRESPONDING AUTHOR

S.V. Maksymova  
E.O. Paton Electric Welding Institute of the NASU  
11 Kazymyr Malevych Str., 03150, Kyiv, Ukraine.  
E-mail: maksymova@paton.kiev.ua

## SUGGESTED CITATION

S.V. Maksymova, P.V. Kovalchuk, V.V. Voronov (2022) Features of the structure of molybdenum–kovar brazed joints. *The Paton Welding J.*, **5**, 33–39.

## JOURNAL HOME PAGE

<https://pwj.com.ua/en>

Received: 07.04.2022

Accepted: 08.08.2022

# STRUCTURE AND PROPERTIES OF ELECTROSLAG WELDED JOINTS OF VT6 TITANIUM ALLOY

**I.V. Protokovilov, V.O. Shapovalov, V.B. Porokhonko, S.G. Hrygorenko**

E.O. Paton Electric Welding Institute of the NASU  
11 Kazymyr Malevych Str., 03150, Kyiv, Ukraine

## ABSTRACT

The paper presents the results of investigations of the quality of electroslag welded joints of 100 mm plates from VT6 titanium alloy. Investigations included X-ray inspection, chemical and gas analysis, optical metallography, mechanical tensile and impact toughness tests, as well as fractographic analysis. X-ray inspection and optical metallography of the welded joint showed absence of surface and inner defects in the weld metal and HAZ. Gas analysis of the weld metal demonstrated its correspondence to standard requirements to VT6 alloy. Ultimate strength of weld metal was equal on average to 90 % of base metal strength, and impact toughness (KCU) was 1.6 times higher than in the base metal. Fractures of metal of the weld and HAZ were of transcrystalline mode of a mixed type, with areas of both ductile and brittle fracture. It is shown that the welded joint mechanical properties are determined, primarily, by the size of grains and microstructure of the weld metal and HAZ, forming under the conditions of a low cooling rate and a high heat input, characteristic for electroslag welding process.

**KEYWORDS:** VT6 titanium alloy; electroslag welding; welded joint; structure; mechanical properties; fracture mode

## INTRODUCTION

Electroslag welding (ESW) is an effective method of joining thick-walled products from different metals and alloys [1–5]. One of the main advantages of ESW is high efficiency and the ability to join products of super-large thicknesses (up to 500 mm or more) in a one pass without edge preparation.

ESW is most widely used during joining of ferrous metallurgy products. However, ESW can also be effective in joining thick-walled components of titanium alloys, including high-strength ( $\alpha+\beta$ )-alloys [6–9]. In this case, an important task is to provide the necessary properties of welded joint.

Among the basic requirements for the quality of ESW of titanium alloys are the absence of critical surface and inner defects, the required gas composition of the weld metal and mechanical properties of the joint, which are determined by both the conditions of structure formation

of weld metal as well as conditions of structure transformations in the heat-affected zone (HAZ) under the action of thermal cycle of welding.

The aim of the work was to investigate the properties of the welded joint of plates of VT6 titanium alloy with a thickness of 100 mm, made by the ESW method.

## EXPERIMENTAL PART

The primary billets for welding were plates of VT6 alloy of 100×150×150 mm in the annealed state (Figure 1). ESW was carried out by a fusible nozzle of VT6 alloy with the use of welding wire of SPT2 alloy. The chemical composition of the used materials is given in Table 1.

The welded joints were subjected to X-ray inspection in the RAP 150/300 device. The transmission parameters were the following: anode voltage is 250 kV, anode current is 10 mA, exposure time is 8.5 min, distance is 500 mm and sensitivity of X-ray inspection is 1 mm.

The chemical composition of the metal was determined by the ICP-spectrometry method. The studies of mechanical properties included tensile and impact toughness (KCU) tests at room temperature. After the test on impact toughness, the specimens were subjected to fractographic analysis. The Brinell hardness was determined using a ball with a diameter of 10 mm at a load of 3 t. The Vickers microhardness tests were performed at a load of 100 g. Metallographic examinations were performed using the Neophot 32 microscope. To detect the structure, the specimens were etched in a solution containing  $\text{HF} + \text{HNO}_3 + \text{H}_2\text{O}$  in

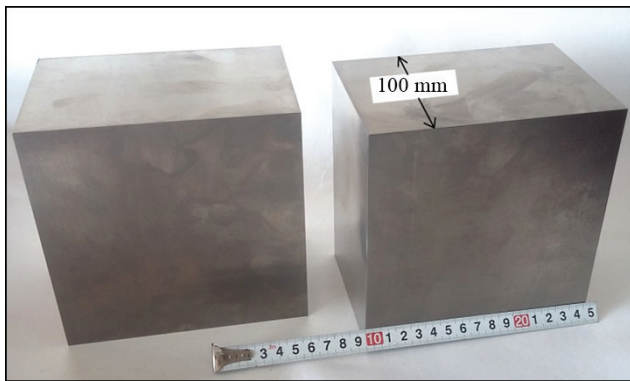


**Figure 1.** Appearance of billets from VT6 alloy

**Table 1.** Chemical composition of the used materials, wt. %

Material	Ti	Al	V	Zr	Fe	Si	O	N	H
Base metal	89.68	6.11	3.65	0.010	0.15	0.042	0.18	0.008	0.0022
Consumable nozzle	89.59	5.49	4.17	0.003	0.06	0.115	0.09	0.005	0.0029
Welding wire	90.93	3.99	3.02	1.550	0.07	0.083	0.05	0.018	0.0022

**Table 2.** Chemical composition of weld metal of VT6 alloy, wt. %

Material	Ti	Al	V	Zr	Fe	Si	O	N	H
Weld metal	90.07	5.32	3.55	0.54	0.11	0.022	0.14	0.009	0.0024
Technical requirements	–	–	–	–	–	–	≤0.2	≤0.05	≤0.015

equal proportions. In all cases, the studies were performed on the metal of three main zones of the welded joint: base metal (BM), HAZ and weld metal (WM).

**RESULTS OF EXPERIMENTS  
AND THEIR DISCUSSION**

The appearance of the welded joints is shown in Figure 2. The surface of the weld is formed well, it has a silver colour without oxidized areas. Defects on the weld surface in the form of pores, lacks of fusion, undercuts and cracks were not detected. The absence of angular deformation in the welded plates should also be emphasized.

X-ray analysis showed absence of inner defects in the weld metal and HAZ.

The results of chemical analysis of the weld metal are given in Table 2. The obtained data show that the content of Al and V in the weld metal corresponds to the values of Table for VT6 alloy (5.3–6.8 % Al and 3.5–5.3 % V). In addition, the weld metal contains 0.54 % of Zr, which is associated with the presence of this element in the welding wire (Table 1).

It should be noted that the gas composition of the weld metal fully meets the requirements of the standard for the VT6 alloy (Table 2). This indicates that the developed method of ESW and the taken techno-

logical measures provide a reliable protection of the weld metal from interaction with atmospheric gases.

The macrostructure of the cross-section of the welded joint is shown in Figure 3. On the macrosection, structural zones of the welded joint are clearly visible: base metal; HAZ, where structural transformations under the effect of the welding thermal cycle occurred (areas of coarse and small grains, as well as the area of partial recrystallization); fusion line; weld metal.

The weld metal is characterized by a columnar structure with rather large crystallites, which diverge from the weld axis to the fusion line in the direction of heat removal. Such structure is typical for cast metal and is formed in the conditions of a high heat input and a relatively low cooling rate that are characteristic to ESW process.

The fusion line is blurred with a smooth transition from polyhedral equilibrium grains of HAZ metal to columnar crystallites of a weld metal (Figure 4).

In general, the macrostructure of the metal is dense, without pores, slag inclusions and other defects.

The study of the distribution of Brinell hardness showed that the highest hardness (*HB*) is in HAZ (285–295), the medium is in the base metal (277–282) and the lowest is in the weld metal (272–280) (Figure 5). Obviously, this is predetermined by a structur-



**Figure 2.** Appearance of welded joints (a) and weld surface (b): 1 — base metal; 2 — weld; 3, 4 — technological straps





**Figure 3.** Macrostructure of welded joint (cross-section): 1 — BM; 2 — weld; 3 — HAZ

al factor and to a lesser extent by the chemical composition of the mentioned zones.

Microstructure of the welded joint zones is shown in Figure 6.

Microstructure of the base metal (Figure 6, a) was characterized by the equiaxial ( $\alpha+\beta$ )-structure with the Vickers hardness of the  $\alpha$ -phase being 3360–3540 and of the  $\beta$ -phase being 3300–3540 MPa. The grain size was 10–15  $\mu\text{m}$ .

The microstructure of the HAZ metal (Figure 6, b–d) consisted of polyhedral grains of ( $\alpha+\beta$ )-structure, and in some areas it had an acicular structure. The plates of the  $\alpha$ -phase were directed in parallel to each other, and also at the angles of 60 and 90° to each other. Their Vickers hardness was 3500–3800 MPa. The hardness of an acicular structure is 3850–3900 MPa. The average grains size of the HAZ metal was significantly larger than the size of the base metal grains and was 300–640  $\mu\text{m}$ .

The weld metal had a two-phase ( $\alpha+\beta$ )-structure with the  $\alpha$ -phase in the form of plates and lamellas, separated by the  $\beta$ -phase interlayers (Figure 6, e, f). On the boundaries of cast crystallites, precipitations of the  $\alpha$ -phase in the form of separate intermittent areas, as well as thin solid precipitations were observed.

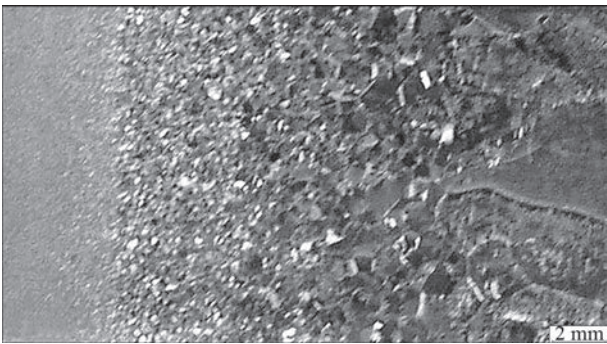


**Figure 4.** Structure of fusion zone

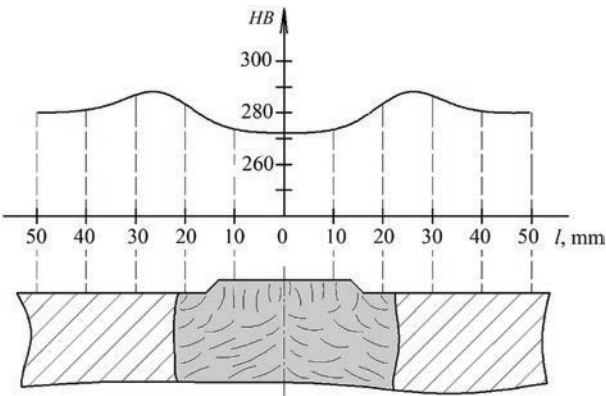


**Figure 5.** Distribution of hardness (HB) in the cross-section of welded joint

The width of grain boundaries ranged from 2.5 to 5.0  $\mu\text{m}$ . The Vickers hardness of the  $\alpha$ -phase was 3100–3700 MPa. It should be noted that near the fusion line, an acicular structure areas with a high hardness of up to 3900 MPa as compared to the hardness of adjacent plates at the level of 3300–3660 MPa occurred. In addition, the weld metal had areas of irregular shape that had a dispersed structure and an increased hardness of up to 4090 MPa. The size of the grains of the weld metal was the largest and amounted to 2–9 mm.

In general, except for the areas with acicular structure and clusters of the  $\beta$ -phase, Vickers hardness in the base metal, HAZ and weld metal was similar and ranged from 3200 to 3800 MPa.

The results of mechanical tests of the welded joint are given in Table 3 and in Figure 7.

The highest values of the yield and tensile strength were observed in the base metal, and the lowest were in the weld metal. In average, the strength of the weld metal amounted to about 90 % of the strength of the base metal. The strength of HAZ was slightly higher than in the weld metal but lower than the strength of the base metal. It can be assumed that a decrease in the strength of the weld metal is associated with a lower content of gas impurities (O, N, H) and also alloying elements (Al, V) with respect to the base metal, which contribute to an increase in titanium strength (Tables 1, 2). However, relative elongation and reduction in area of the weld metal were also lower than those in the base metal. This indicates that reducing the mechanical characteristics of the welded joint during

**Table 3.** Mechanical properties of welded joint of VT6 alloy

Material	$\sigma_y$ , MPa	$\sigma_t$ , MPa	$\delta$ , %	$\psi$ , %	KCU, J/cm <sup>2</sup>
BM	929.9	971.4	16.9	44.1	38.7
WM	806.4	874.7	10.6	34.2	61.9
HAZ	817.2	878.0	9.3	23.4	55.9

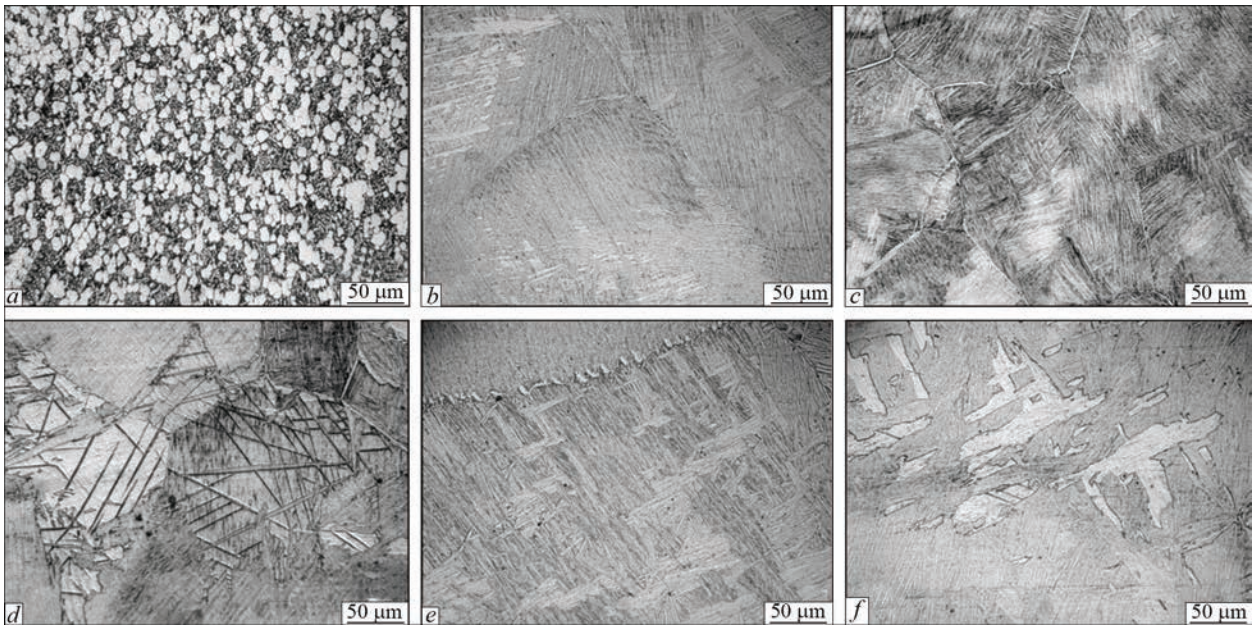


**Figure 6.** Microstructure of welded joints: *a* — base metal; *b–d* — HAZ; *e, f* — weld metal

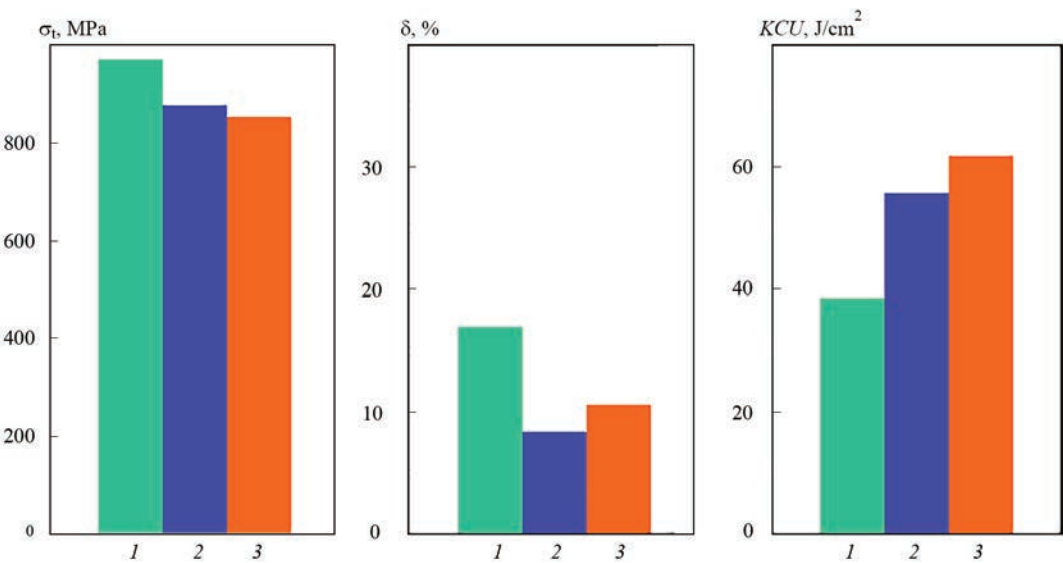
tensile tests is mainly associated with the structural factors and the size of the weld metal grains.

Another picture was obtained during the tests on impact toughness. In this case, the weld metal had the values of impact toughness 1.6 times higher than those in the base metal. This is probably associated with the extremely large size of crystallites of the weld metal (up to 9 mm), which could cause the fact that only a few crystals crossed the plane of the notch of the specimens where the fracture occurred. In turn, this led to a transcrystalline mode of fracture and an increase in impact toughness of the weld metal. In addition, an increase in impact toughness may be associated with a low content of impurities on the boundaries of grains in the weld metal.

Thus, the mechanical properties of the welded joint, which are determined by the properties of the

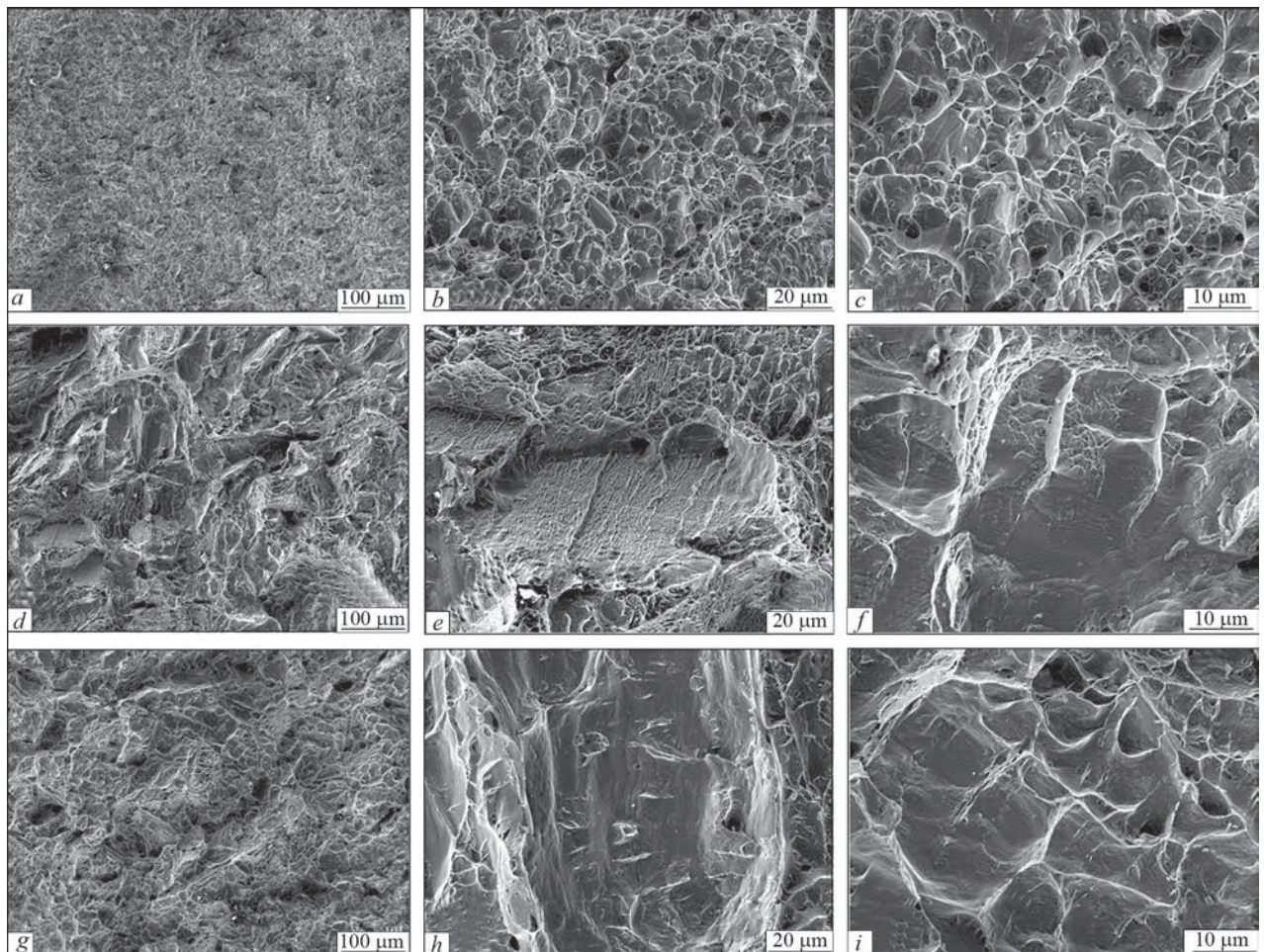
weld metal and HAZ, are associated primarily with the size of grains and microstructure, and secondly, with the chemical composition and content of harmful impurities. Large transverse size of grains and unfavourable acicular ( $\alpha+\beta$ )-microstructure in the weld metal and HAZ most negatively affect the tensile strength and ductility (relative elongation and reduction in area) of electroslag welds.

Figure 8 shows the fractograms of the specimens after the tests on impact toughness. The inspection of the fracture surfaces at a small magnification ( $\times 100$ ) showed the following: the fracture mode of the base metal is transcrystalline (Figure 8, *a*); the fracture surface is matt; the main crack propagates strictly perpendicularly to the applied load (mainly on the grain body); the fracture mode of the weld metal and HAZ is transcrystalline of a mixed type (Figure 8, *d, g*); the



**Figure 7.** Mechanical properties of welded joint: *1* — base metal; *2* — HAZ; *3* — weld metal





**Figure 8.** Fractograms of specimens after tests on impact toughness: *a–c* — base metal; *d–f* — HAZ; *g–h* — weld metal

surfaces of fractures are matt and shining, but more matt component is observed; the main crack changes its direction in the process of propagation.

The further studies were performed at increased magnifications. It was found that the fracture mode of the base metal is transcrystalline, ductile, with a pit surface (Figure 8, *b, c*). The weld metal and HAZ are characterized by transcrystalline fracture of a mixed type with the areas of both ductile (pit) as well as brittle (spalling facets, quasi-spalling) fractures (Figure 8, *e–h*). But it should be noted that as compared to HAZ, the surface of the fracture of the weld metal had pits and facets of a larger size, which indicates a significant growth of grains in this area.

In general, it can be suggested that branching of cracks in the weld metal and in HAZ contributed to the fact that their propagation requires more energy, as a result of which the impact toughness increased as compared to the base metal, where the fracture occurred without branching.

## CONCLUSIONS

1. ESW of plates of titanium VT6 alloy of 100 mm thickness was performed.

2. X-ray analysis and optical metallography showed absence of pores, cracks, slag inclusions, lacks of fusion and other inner defects of the welded joint on macro- and microlevels.

3. The gas composition of the weld metal meets the technical requirements for VT6 alloy, which indicates a reliable protection of the welding pool metal from interaction with atmospheric gases.

4. The tensile strength of the weld metal is about 90 % of the strength of the base metal, but the impact toughness of the weld metal is 1.6 times higher than the impact toughness of the base metal.

5. The fracture mode of the weld metal and HAZ is transcrystalline of a mixed type with the presence of both brittle as well as ductile areas on the fracture surface. The fracture surface of the weld metal is characterized by the most considerable relief that indicates a significant growth of grains in the area.

6. The mechanical properties of the welded joint, first of all, are associated with the size of the grains and microstructure of the weld metal and HAZ, which are formed in the conditions of low cooling rate and high heat input, which is characteristic of ESW.



## REFERENCES

1. Paton, B.E., Yushchenko, K.A., Kozulin, S.M., Lychko, I.I. (2019) Electroslag welding process. Analysis of the state and tendencies of development (Review). *The Paton Welding J.*, **10**, 33–40. DOI: <https://doi.org/10.15407/tpwj2019.10.05>
2. Yushchenko, K.A., Lychko, I.I., Kozulin, S.M. et al. (2018) Application of welding in construction. *The Paton Welding J.*, **9**, 23–27. <https://doi.org/10.15407/tpwj2018.09.05>
3. Kaluc, E., Taban, E., Dhoogev, A. (2006) Electroslag welding process and industrial applications. *Metal Dunyasi*, **152(13)**, 100–104.
4. Yushchenko, K.A., Kozulin, S.M., Lychko, I.I., Kozulin, M.G. (2014) Joining of thick metal by multipass electroslag welding. *Ibid.*, **9**, 30–33. <https://doi.org/10.15407/tpwj2014.09.04>
5. Paton, B., Dudko, D., Palti, A. et al. (1999) Electroslag welding (Prospects of development). *Avtomatich. Svarka*, **9**, 4–6 [in Russian].
6. Shcherbinin, E., Kompan, Ya. (2005) MHD Technologies of Electroslag welding and melting of Titanium alloys for aerospace industry. *Proc. of 15<sup>th</sup> Riga and 6<sup>th</sup> Pamir Conf. on Fundamental and Applied MHD*, 287–290.
7. Devletian, J., Chen, S.J., Wood, W. et al. (1990) Fundamental aspects of electroslag welding of titanium alloys. Recent trends in welding science and technology. *ASM Intern.*, 419–424.
8. Chen, S.J., Devletian, J.B. (1990) Microstructure and mechanical properties of electroslag welds in Ti–6Al–4V alloy. *Weld. J.*, **69(9)**, 319–324.
9. Protokovilov, I.V., Porokhonko, V.B., Petrov, D.A. (2013) Technological peculiarities of electroslag narrow-gap welding of titanium. *The Paton Welding J.*, **1**, 34–38.

## ORCID

I.V. Protokovilov: 0000-0002-5926-4049,  
V.O. Shapovalov: 0000-0003-1339-3088,  
V.B. Porokhonko: 0000-0002-6490-7221,  
S.G. Hrygorenko: 0000-0003-0625-7010

## CONFLICT OF INTEREST

The Authors declare no conflict of interest

## CORRESPONDING AUTHOR

I.V. Protokovilov

E.O. Paton Electric Welding Institute of the NASU  
11 Kazymyr Malevych Str., 03150, Kyiv, Ukraine.  
E-mail: lab38@paton.kiev.ua

## SUGGESTED CITATION

I.V. Protokovilov, V.O. Shapovalov,  
V.B. Porokhonko, S.G. Hrygorenko (2022) Structure  
and properties of electroslag welded joints of VT6  
titanium alloy. *The Paton Welding J.*, **5**, 40–45.

## JOURNAL HOME PAGE

<https://pwj.com.ua/en>

Received: 21.04.2022

Accepted: 08.08.2022

# STUDY OF EDDY CURRENT FLAW DETECTOR BASED ON DOUBLE-CIRCUIT SELF-GENERATOR OPERATED IN INTERMITTENT OSCILLATING MODE

**V.M. Uchanin**

G.V. Karpenko Physico-Mechanical Institute of NASU  
5 Naukova Str., 79060, Lviv, Ukraine

## ABSTRACT

Timely application of nondestructive methods for testing critical structures of modern engineering is an important factor ensuring their safe and trouble-free operation. Eddy current testing means have no alternative for contactless detection of cracks in aircraft structures. In order to detect surface cracks (also through a layer of dielectric coating), self-generator eddy current flaw detectors are used, working at operating frequencies above 1 MHz. To develop such flaw detectors, it is promising to use double-circuit self-generator oscillatory system, operating in intermittent oscillatory mode. This work is a study of new technical solutions, in particular self-generator circuit based on a field transistor with insulated gate, circuit of controlling the generation frequency and circuit of regeneration of self-generator oscillations. Their advantages in terms of sensitivity are shown, compared to traditional circuits. The analyzed engineering solutions were used to develop self-generator eddy current flaw detectors of VD 3.03N, VD 3.02N, VD 4.01N and VD 4.03N type for surface crack detection, which have passed state testing and are widely used, in particular for maintenance of SC “Antonov” aircraft and SC “Ivchenko-Progress” and PJSC “Motor-Sich” aircraft engines. It is intended to apply these engineering solutions in the new self-generator flaw detector with functions of automatic adjustment for the level of sensitivity and its indication set by the specified procedure.

**KEYWORDS:** eddy current nondestructive testing, self-generator eddy current flaw detector, surface cracks, intermittent generation, double-circuit, oscillation regeneration

## INTRODUCTION

Reliability and safety of critical structures and components of modern engineering largely depends on timely application of nondestructive testing (NDT) means during their fabrication and operation, which is particularly important under the conditions of extension of service life and operating loads, influence of aggressive media, etc. Means of eddy current NDT using more than 1 MHz operational frequencies have traditionally been used for contactless detection of shallow cracks in metal structures [1, 2]. At the same time, eddy current method has a considerable sensitivity to a range of factors (alongside defects), which influence the eddy current probe (ECP) output signal. Among such factors we will note changes in specific electric conductivity (SEC) and magnetic permeability of the material of the tested object (TO), influence of the edge of the tested object, variation of the geometrical parameters and gap between the ECP and tested object (TO) surface (lift-off effect). Changes of the lift-off and ECP inclination during manual testing are considered to be the most harmful sources of erroneous operation of the testing instrumentation. Changes in the lift-off, caused by different roughness of TO surface or variations of the thickness of the dielectric coating, can also lead to erroneous operation of eddy current flaw detector (ECFD). Therefore, in order to obtain valid results, it is important to ensure

a high level of attenuation of the lift-off effect and simple interpretation of testing results.

ECFD of self-generator type are widely used for eddy current flaw detection in structures and components in different industries [1–8]. A common feature of such ECFD is connection of single-coil ECP as an element of oscillatory circuit of self-generator (SG), which is a nonlinear resonance amplifier, included into a feedback loop [9]. Flaw detectors of this type were introduced already in mid-50s of the previous century, which was related to mastering the production of heavy aircraft and powerful aircraft engines [1]. At the end of 80s of the previous century self-generator ECFD of PROBA-5 and TVD-A type were serially produced, and are still operating successfully in some enterprises [1, 3, 4]. Self-generator ECFD are characterized by a high sensitivity to surface-breaking defects, possibility to suppress the lift-off influence, autonomous power supply, small dimensions and weight. Many variants of construction of self-generator ECFD have been proposed, each of which has its shortcomings and advantages. Comparative analysis of different variants of construction and classification of self-generator ECFD is given in work [10].

Oscillatory system of self-generator used in ECFD may consist of one or two resonance circuits. Single-circuit SG were built by the scheme with a common base and capacitive feedback. Double-circuit self-generator have better metrological characteristics due to a more

flexible readjustment into different modes. An important difference of double-circuit ECFD is the dependence of feedback coefficient on frequency that may be used to attenuate the lift-off influence [1, 8, 10, 11]. An important feature of self-generator ECFD also is the type of oscillations produced by the self-generator. In some ECFD models, for instance VD-22N (PROBA-5), permanent continuous oscillations are used [3]. Application of intermittent oscillations looks promising. They are formed under the condition, when the time constant of the automatic bias circuit  $\tau_b = R_r \cdot C_s$  ( $R_r$  and  $C_s$  are the resistor resistance and separating capacitance in the gate circuit) will be greater than the time constant of the working oscillation regeneration  $\tau_{osc} = 2L/R$  ( $L$  and  $R$  are the inductance and resistance of ECP winding), i.e. under the condition of  $\tau_b \gg \tau_{osc}$  [1, 4, 8, 10]. An additional advantage of such ECFD is the possibility of construction a sound change-tone indication without application of voltage-controlled low-frequency generators. More over, ECFD with intermittent oscillations allow controlling exceeding of the ECP lift-off by ear, due to change-tone indication [4]. The frequency of passage of a series of high-frequency oscillations changes at the change of introduced resistance of ECP, as ECP parameters influence the time constant of the working circuit. Selection of the value of time constant of the automatic bias circuit allows setting the frequency of passage of a series of high-frequency oscillations in the sound range. An additional advantage of ECFD with intermittent oscillations is its cost-effectiveness, as the active element does not consume energy during interrupted generation that is important for ECFD with autonomous power supply. The method to obtain intermittent oscillations is determined by selection of values of  $RC$ -elements of automatic bias in the transistor gate (base) circuit [1]. The given short overview highlighted the effectiveness of construction of self-generator ECFD on the base of application of double-circuit scheme operated in intermittent oscillating mode [8, 10, 11].

The **objective** of this study is analysis of engineering solutions, invented during development of portable self-generator ECFD of VD 3.03N, VD 3.02N, VD 4.01N and VD 4.03N type (Leotest VD). We are talking about an improved SG scheme, self-generator frequency control circuit (SFCC) and self-generator oscillation regeneration circuit (SORC).

## 1. DEVELOPMENT AND INVESTIGATION OF AN IMPROVED SELF-GENERATOR SCHEME

Bipolar transistors or field transistors with a closed  $p$ - $n$ -junction are most often used as an active element in many known self-generator ECFD. Conducted analysis showed that an effective circuit of self-generator ECFD can be based on insulated-gate field transistors,

in which the feedback circuit is practically not loaded by active element input resistance (Uchanin V.M., Cherlenskiy V.V. Eddy current flaw detector. Patent of Ukraine 39207, 2009, Bul. No. 3). The proposed scheme (Figure 1) consists of a double-circuit SG 1, having working loop 2 with connected into it ECP 3 of parametric (single-coil) type and reference loop 7. Self-generator 1 is based on insulated-gate field-effect transistor 9, with diode 6 additionally connected into its automatic bias circuit in parallel to resistor 8. SORC 10 is additionally connected between SG 1 output and power block 12. Sound indication block 11 is connected to the output of SG 1. Varicap 4 can be connected into SG working circuit, its controlled input being connected to power block 10 through a block of controlled constant voltage, made in the form of potentiometer 5.

Investigations of the signals of the proposed scheme for conformity to intermittent generation mode were conducted using digital oscillograph TDS 1012 with communication module with a computer of TDS 2CMA type [12]. The signals were registered in the drain of field transistor VT1 (Figure 1) at connection of single-coil ECP into the working circuit [11]. Standard specimen (SS) of SOP 5-1 type from aluminium alloy with an artificial defect of 2 mm length, 0.5 mm depth and 0.1 mm opening was used. Figure 2 shows signals, obtained when placing ECP at a distance from SS (in "air") (Figure 2, *a*) and in SS defect-free zone (Figure 2, *b*), with scanning time of 2.5 ms/div. ECFD was first set to maximum sensitivity to defects in the studied material. As we can see, the nature of the signal does not change, when ECP is placed in "air" and on SS surface. Here, when ECP is placed in "air", the period of repetition of series of high-frequency oscillations is 2 ms (frequency  $F = 500$  Hz), and when ECP is installed on SS the period of repetition of series of high-frequency oscillations is reduced two times to 1 ms (frequency  $F = 1$  kHz). Signal am-

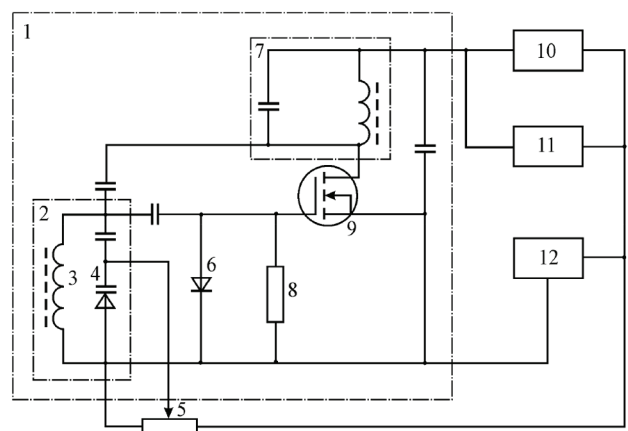


**Figure 1.** Circuit of self-generator ECFD based on field transistor with insulated-gate



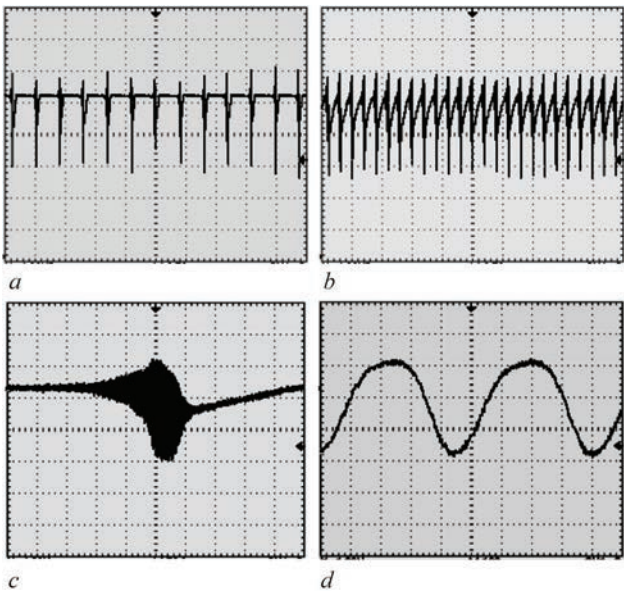


**Figure 2.** Signals in the drain of field transistor when ECP is placed in “air” (a) and in SS defect-free zone at scanning time of 2.5 ms/div (b), 50 μs/div (c), and 100 ns/div (d)

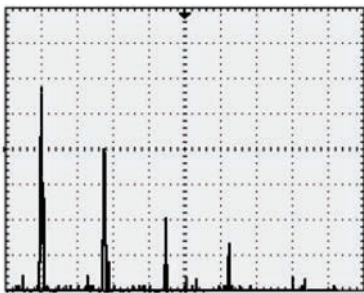


**Figure 3.** Signal spectrum in the drain of field transistor when ECP is placed in “air”

plitude when ECP is installed on SS is only slightly increased. Let us consider in greater detail the signal structure, when the oscillograph scan time in case of placing ECP in “air”, was reduced from 2 ms/div (Figure 2, a) to 50 μs/div and 100 ns/div (Figure 2, d), i.e. the image was “stretched” on the time scale by 40 and 20000 times, respectively. High-frequency filling of the pulse of SG intermittent generation (Figure 2,

a) can be seen in greater detail at reduction of scan time to 100 ns (Figure 2, d). The filling signals have a shape close to the sinusoidal one of 2.2 MHz frequency (Figure 2, d).

Figure 3 shows the spectrum of the signal, given above in Figure 2, which was obtained using digital oscillograph TDS 1012, which allows realization of the operation of fast Fourier transform [12]. The signal spectrum shows the components decreasing in amplitude, the distance between which is 2.2. MHz on the frequency axis, that corresponds to the frequency of high-frequency filling of the pulse in Figure 2, d.

Let us consider the dependencies of bias voltage  $U_b$  and frequency  $F$  of high-frequency oscillation series repetition on frequency  $f$  of SG high-frequency oscillations (Figure 2). Frequency  $f$  and frequency  $F$  of high-frequency oscillation series repetition were measured by digital oscillograph of TDS 1012 type by connection to the drain of transistor VT1 through 1:10 voltage divider. Bias voltage  $U_b$  was measured on the gate of transistor VT1 (Figure 1) by digital multimeter M890F with internal resistance of 20 MOhm/V, which was connected via 1 MOhm resistor to eliminate the influence of parasitic capacitance. Frequency  $f$  was changed by adjustment of SG working circuit. Investigations were conducted when positioning ECP in “air”, as well as after installing ECP on SS from a nonferromagnetic alloy with SEC from 0.54 to 51.9 MS/m and on SS from ferromagnetic steel 45 for two control modes which correspond to highly conductive (aluminium alloys) and low conductive (titanium alloys, steels) materials. Generation suppression point (GSP in Figures 4, 5) was determined for each studied material and SG setting mode.

Analysis of the dependencies in Figures 4, 5 shows that suppression of SG oscillations for SS with different SEC for each mode of SG setting (and material group) is found at the same operational frequency  $f$  and bias voltage  $U_b$ . In modes of testing low conductive and highly conductive materials SG generates stable

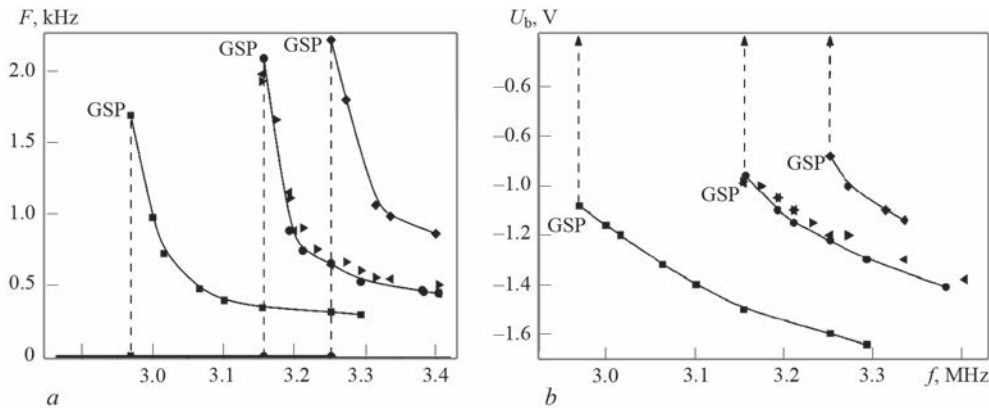


**Figure 4.** Dependence of frequency  $F$  of repetition of a series of high-frequency oscillations (a) and bias voltage  $U_b$  (b) of SG in the range of testing low-conductive materials on operational frequency  $f$ , when ECP is placed in “air” (■) and on SS with SEC of 0.54 MS/m (◄); 0.4 MS/m (►); 2.05 MS/m (●) and steel 45 (◆)

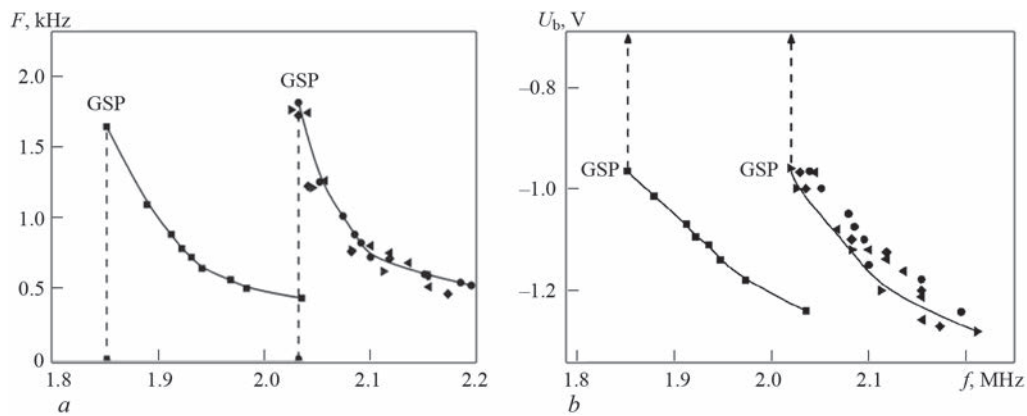


**Figure 5.** Dependence of frequency  $F$  of repetition of a series of high-frequency oscillations (*a*) and bias voltage  $U_b$  (*b*) of SG in the range of testing highly conducting materials on working frequency  $f$  when ECP is placed in “air” (■) and on SS with SEC of 11.0 MS/m (●); 14.8 MS/m (◄); 30.4 MS/m (►) and 51.8 MS/m (◆)

high-frequency oscillations in operational frequencies of 3.4 and 2.2 MHz that corresponds to the start of the studied frequency ranges. At reduction of frequency  $f$  (operational frequency) and respective increase of the difference in resonance frequencies of working and reference circuits  $\Delta f$ , the generation conditions deteriorate. It leads first to gradual increase of pulse repetition frequency  $F$  and generation suppression (GSP), which is shown in Figures 4, *a* and 5, *a* by a vertical dashed line. Steepness of the dependencies becomes greater, when moving closer to generation suppression point that confirms the high sensitivity of self-generator when setting it up into a mode close to this point (GSP in Figures 4, 5). At lowering of operational frequency  $f$  due to deterioration of generation conditions and reduction of high-frequency oscillation amplitude, bias voltage  $U_b$  decreases, until it reaches a certain value, at which generation suppression takes place. In the absence of high-frequency oscillations after oscillation suppression, bias voltage  $U_b$  decreases abruptly (vertical dashed line in Figures 4, *b* and 5, *b*) to zero.

Effectiveness of the developed SG circuit was studied experimentally by comparing the sensitivity of self-generator ECFD based on field transistors 2P303 (with closed  $p$ - $n$ -transition) and 2P305 (with insulated gate). Change of the frequency of repetition of high-frequency oscillation series in intermittent generation mode at introduction of additional resistance of 47 kOhms into the working loop, was taken as the sensitivity criterion (Table 1). Before that, ECP was mounted on the defectfree part of SS from an aluminium alloy (SOP 5-1), titanium alloy (SOP 5-2) and ferromagnetic steel (SOP 5-3).

Presented results indicate that the sensitivity of the proposed ECFD circuit with SG based on a transistor with an insulated gate is higher for all structural materials. Sensitivity increases the most (by 1.5 times) for highly conductive nonferromagnetic materials and the least (by 1.2 times) — for a ferromagnetic alloy. Selection of an insulated-gate field transistor as an SG active element allows increasing the operating reliability of self-generator ECFD, when testing materials with different electrophysical properties and different gap between ECP and TO surface, owing to better technical characteristics of such a transistor, in particular, high input resistance, limit frequency and transient slope.

## 2. IMPROVEMENT AND INVESTIGATION OF SELF-GENERATOR FREQUENCY CONTROL CIRCUIT

To set ECFD to the mode of maximum sensitivity, when testing materials with different electrophysical properties, the resonance frequency of SG working loop should be readjusted, for which purpose variable capacitance capacitors are used. In outdated self-generator ECFD adjustment of frequency is performed using variable capacitors with air or solid dielectric, which have a significant drawback of large overall dimensions and low reliability. More promising is the electronic method of readjustment, using semiconductor diodes (varicaps), the capacitance of which depends on reverse (cut-off) voltage applied to the  $p$ - $n$ -junction. Small dimensions of varicaps allow placing them near SG active element. The length of contact leads to control the varicap capacitance is not

**Table 1.** Comparison of sensitivity of ECFD with SG based on transistors of different types

Transistor type	ECP on SOP-5-1			ECP on SOP 5-2			ECP on SOP 5-3		
	$F_1$	$F_2$	$\Delta F$	$F_1$	$F_2$	$\Delta F$	$F_1$	$F_2$	$\Delta F$
2P 303	2.38	2.22	0.16	3.23	2.71	0.52	3.23	2.63	0.60
2P 305	1.59	1.35	0.24	2.33	1.70	0.63	2.50	1.72	0.78

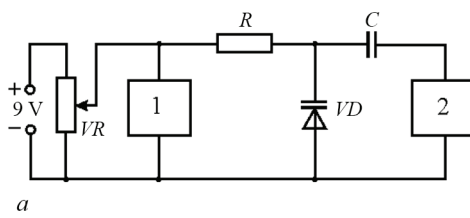
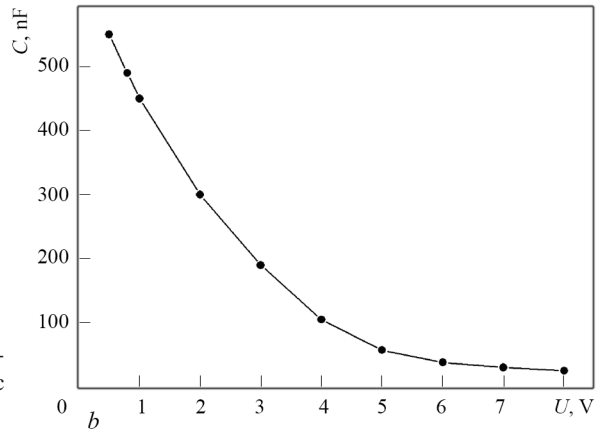


**Figure 6.** Circuit for studying the volt-farad characteristics of varicaps (a) and volt-farad characteristic of varicap of VV 112 type (b)



a critical value, as control is performed using constant voltage. Smoothness of adjustment using a potentiometer is better than that of a replaceable capacitor. For instance, a replaceable resistor of SP3-33 type allows rotating the axis by an up to  $320^\circ$  angle, that is 1.8 times greater than the angle of rotation of a replaceable capacitor. Varicaps have been known for a longtime, but the industry has only recently mastered production of varicaps with a high  $Q$ -factor ( $Q \times 200$ ) with readjustment range by capacitance from 30 up to 600 pF and small dimensions ( $3.8 \times 1.6$  mm). Comparative analysis showed that the most promising for construction of self-generator ECFD is varicap of VV 112 type, which in addition to a high  $Q$ -factor has the best overlap ratio and temperature stability. VV 112 varicap is controlled by voltage from 0.5 up to 8.0 V that makes it applicable for instruments with autonomous power supply. It is important that VV 112 varicap has the lowest reverse current  $I_r$ , which is a constant parasitic current that flows through the varicap in the reverse direction at the set reverse voltage.

The main disadvantage of the varicaps is a low  $Q$ -factor, which even in the best varicaps is by an order of magnitude lower than that of ceramic capacitors, and by two-three orders lower than that of air capacitors. We will assess the possible influence of varicap of VV 112 type with  $Q_v = 200$  on the  $Q$ -factor of oscillatory system as a whole. For this purpose we will use the expression for equivalent factor  $Q_E$  of an oscillatory system from connected in parallel capacitor and inductance of ECP winding with  $Q_{ECP}$  factor [13], which has the form of  $Q_E = Q_{ECP} Q_v / (Q_{ECP} + Q_v)$ . For the used basic ECP,  $Q_{ECP}$  winding factor has the value from 11.0 to 24.0, depending on TO material. It is obvious that in this case the  $Q$ -factor of SG oscillatory system will be limited predominantly by  $Q$ -factor of ECP winding. Connection of varicap of VV 112 type lowers the  $Q$ -factor of SG oscillatory system by 10–12 %, which can be regarded as insignificant, considering other advantages, the more so since the conducted assessment characterizes the worst case, when

varicap  $Q$ -factor is the smallest at minimum value of control voltage  $U_{\min} = 0.5$  V.

The varicap operating mode should take into account its volt-farad characteristic, which was studied for varicap VV 112 using voltmeter of M 890 F type and CLR 2 meter of E 7-13 type (Figure 6, a). Varicap VD is connected to potentiometer VR 1 through resistor  $R = 100$  kOhm, the role of which consists in protection of varicap VD and meter CLR 2 of E 7-13 type at the lower position of mobile electrode of VR potentiometer. Voltage on resistor  $R$  must be much lower than the smallest value of control voltage  $U_{\min} = 0.5$  V. Voltage across resistor  $R$  is determined by varicap reverse current ( $I_r = 5 \cdot 10^{-8}$  A) and it is equal to  $R \cdot I_r = 5$  mV, i.e.  $R \cdot I_r \ll U_{\min}$ , that allows ignoring the influence of resistor  $R$  on measurement error. Capacitor  $C$  was introduced for protection of CLR meter of E 7-13 type from constant voltage penetration. Here, capacitance  $C = 0.1$   $\mu$ F, i.e. it is selected to be much higher than the varicap maximum capacitance ( $C_{\max} = 620$  pF) that allows ignoring its influence.

Volt-farad characteristics of VV 112 varicap (Figure 6, b) is nonlinear. Minimum and maximum values of control voltage are  $U_{\min} = 0.5$  V and  $U_{\max} = 8$  V, respectively. One can see from Figure 6, b that the change of control voltage from 6 to 8 V has little effect on varicap capacitance. Therefore, it is rational to limit the maximum value of control voltage by 6 V, at which minimum value of varicap capacitance  $C_{\min}$  is equal to 50 pF.

The effectiveness of electron control of SG frequency depends on the scheme of varicap connection into the oscillatory circuit. Traditional varicap connection to control SG frequency is given in Figure 7, a [13, 14]. With the traditional circuit of varicap VD connection at low control voltage, it begins conducting current during the negative half-wave of SG high-frequency oscillations that leads to their distortion. Moreover, the oscillatory circuit receives additional load, leading to lowering of its  $Q$ -factor and sensitivity to changes of ECP parameters. Influence of this



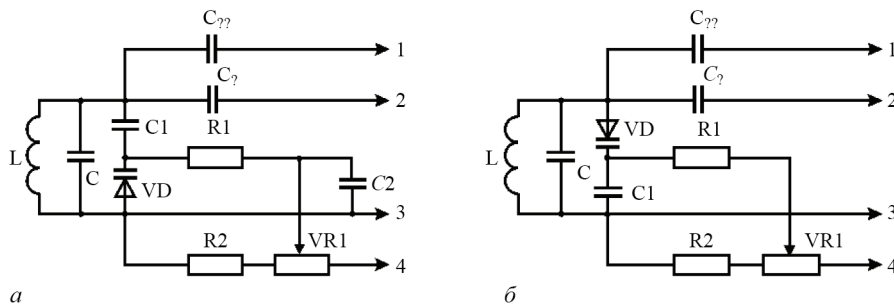


**Figure 7.** Traditional (*a*) and proposed (*b*) schemes for connection of VD varicap into SG working circuit: 1–4 — leads of SG feedback, control electrode of SG active element, common wire and supply voltage, respectively

factor was reduced in the proposed scheme of varicap connection into SG working circuit (Uchanin V.M., Cherlenezkyi V.V. Device for eddy current testing. Patent of Ukraine: 42132, 2009, Bul. No. 12). In the proposed circuit (Figure 7, *b*) at low control voltage varicap current will influence the positive half wave of high-frequency oscillations. It, however, affects the operation of automatic bias circuit, which maintains a constant level of oscillation amplitude. Moreover, in the proposed circuit the influence of noises introduced into SG working loop by mobile contacts of variable resistor VR, which may reach 15–50 mV, is reduced due to filtration by R1 and C1 elements. It allows reaching a more accurate SG setting to a mode close to generation suppression, and making full use of the high sensitivity of the circuit.

Let us consider the influence of varicap capacitance on amplitude-frequency characteristics (AFCh) of oscillatory system of self-generator ECFD (Figure 1). Here, SG was brought into the mode of high-frequency regenerative amplifier. For this purpose, generation was suppressed by reducing the active element supply voltage. ECP was connected to flaw detector SG by a coaxial cable, which is part of the oscillatory system [15]. To eliminate shunting of the working circuit by low output resistance of the generator, the outer generator signal was introduced through coupling capacitor of 10 pF capacitance, as it has to be much smaller than the minimum value of working circuit capacitance. Minimum value of working loop capacitance is equal to 150 pF, as in keeping with the above assessments, it consists of cable capacitance (100 pF) and smallest value of varicap capacitance ( $C_{\min} = 50$  pF). To eliminate the influence of elements of automatic bias circuit on oscillatory system AFCh, the voltage amplitude of external generator was selected equal to 1 V. Here, voltage amplitude in the working loop is not higher than 15 mV, i.e. it is much smaller than the voltage of 200 mV, from which diode 6 (Figure 1) of SG automatic bias circuit starts operating. Millivoltmeter was connected to drain loop of transistor 9 (Figure 1) by a high-frequency head. Investigations were conducted, placing ECP in “air” at the highest

values of varicap capacitance and in the defect-free part of SS of SOP 5-1 type (D16 aluminium alloy) at the highest and lowest values of varicap capacitance.

Each of the obtained AFCh (Figure 8) has two resonance maximums which is characteristic for SG double-circuit oscillatory system. Here, the maximum amplitude of the reference loop is greater than that of the working circuit in the entire range of varicap capacitance change that is attributable to higher  $Q$ -factor of the reference loop, compared to that of the working circuit ( $Q_{\text{ref}} \approx 90$ ,  $Q_{\text{work}} \approx 20$ ). When ECP is installed on SS the amplitude decreases in both the maximum points for all the modes that is attributable to lowering of ECP winding  $Q$ -factor at interaction with SS from an aluminium alloy. At the change of varicap capacitance from the minimum ( $C_{\min} = 50$  pF) to maximum one ( $C_{\max} = 620$  pF), the value of working circuit resonance frequency is increased by 1.3 MHz, and the loop resonance frequencies become closer. At the same time, the amplitude in the point of maximum of the working circuit characteristic is increased. Here, the resonance frequency of the reference circuit does not change noticeably, that is also attributable to higher  $Q$ -factor of the reference circuit.

The presented procedure of determination of oscillatory system AFCh was used for ECFD adjustment during their manufacture, as it allows revealing the el-

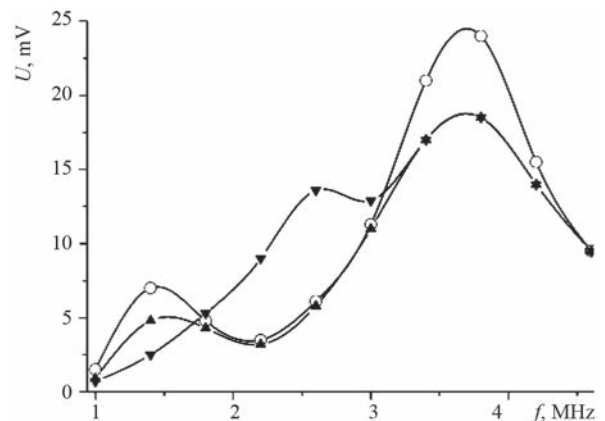


**Figure 8.** Amplitude-frequency characteristics of oscillatory system of SG: when ECP is in “air” at the highest value of varicap capacitance (○) and on defectfree part of SS from aluminium alloy at the highest (▼) and lowest (▲) values of varicap capacitance

**Table 2.** Comparison of SG sensitivity with different varicap connections

Circuit	ECP on SOP 5-1			ECP on SOP 5-2			ECP on SOP 5-3		
	$F_1$	$F_2$	$\Delta F$	$F_1$	$F_2$	$\Delta F$	$F_1$	$F_2$	$\Delta F$
Traditional (Figure 7, a)	1.59	1.35	0.24	2.33	1.70	0.63	2.50	1.72	0.78
Proposed (Figure 7, b)	1.61	1.28	0.33	2.13	1.22	0.91	2.33	1.28	1.05

ements with a low  $Q$ -factor (for instance, poor quality capacitors) and ensure ECP replaceability due to improvement of repeatability of ECFD characteristics.

Comparison of the sensitivity of self-generator ECFD with application of the traditional and new SFCC was conducted by the above procedure, where the sensitivity criterion was taken to be the change  $\Delta F = F_1 - F_2$  of the frequency of repetition of a series of high-frequency oscillations, at introduction of additional resistance of 47 kOhm into the working loop, when ECP is mounted on defect-free zone of SS from an aluminium alloy (SOP 5-1), titanium alloy (SOP 5-2) and ferromagnetic steel (SOP 5-3). All studied ECP were based on a field transistor with an insulated gate. Measurement results are given in Table 2.

Results presented in Table 2 show that the sensitivity of ECP with the proposed SFCC is higher than that of the traditional circuit by 1.38; 1.44 ad 1.35 times for aluminium and titanium alloys and ferromagnetic steels, respectively, i.e. it allows achieving a higher sensitivity during testing all structural materials.

**3. SORC IMPROVEMENT AND INVESTIGATION**

The main function of SORC is fast resumption of SG oscillations after detection of the defect, and respective generation suppression. It is achieved by improvement of oscillation generation conditions by increasing the supply voltage. In the first self-generator ECFD such circuits were absent and regeneration was performed by removing ECP from TO surface [1]. ECP lifting from TO surface improves its  $Q$ -factor and reduces the losses in the oscillatory loop. It is obvious that such a procedure of resumption of SG oscillations complicates the procedure and productivity of testing. Later on relaxation generators were used for oscillation regeneration. They were connected into the sup-

ply circuit of SG active element and were started after suppression of its generation. Periodical increase of supply voltage of self-generator active element leads to improvement of generation resumption conditions. Self-generator ECFD of TVD type, in particular, includes SORC, in which the relaxation generator consists of a current-stabilizing element, delay line based on single-junction transistor with RC-circuit, which sets the frequency of relaxation oscillations, and a key, switching of which leads to a periodical increase of supply voltage [4].

Analysis of the conditions, promoting resumption of SG oscillations, allowed suggesting a new SORC (Uchanin V.M., Cherlenskyyi V.V. Eddy current self-generator flaw detector. Patent of Ukraine, Pat. 39217, 2009, Bul. No. 3), which, owing to its fast response, allows greatly improving the testing productivity, compared to analogs, and which, in principle, can operate with SG based on different active elements. Let us consider the operation of an improved SORC (Figures 9–11). When ECP 1 is mounted on a defectfree region of TO, self-generator 2 generates intermittent oscillations near the generation suppression point (GSP in Figures 4, 5), which are heard as changed-tonal sound of sound indicator 6. When a defect arises, the  $Q$ -factor of ECP 1 decreases, leading to reduction of  $Q$ -factor of the working circuit of SG 2 and oscillation suppression. SG 2 output signal via capacitor 4 comes to limiting amplifier 5, which forms a signal of sound frequency. This signal come to sound indicator 6 and to the input of defect signal former 7, which forms a short pulse at its appearance, the amplitude of which changes from supply voltage value to zero. A short pulse comes to transistor regulator of current T2 via diode D4 of supply voltage control circuit (Figure 11). Current regulator transistor T2 opens, leading to increase of SG 2 supply voltage. As a result, intermittent oscillations of SG 2 are resumed provided ECP 1 is shifted from the defect, and SG 2 is ready for further operation. When ECP is located on the defect, the process of lowering and subsequent increase of SG 2 power supply is repeated with the frequency close to 100 Hz. The repetition frequency of these pulses is in the sound range and after amplification it is recorded by sound indicator 6. A short pulse from the output of defect signal former 7 comes

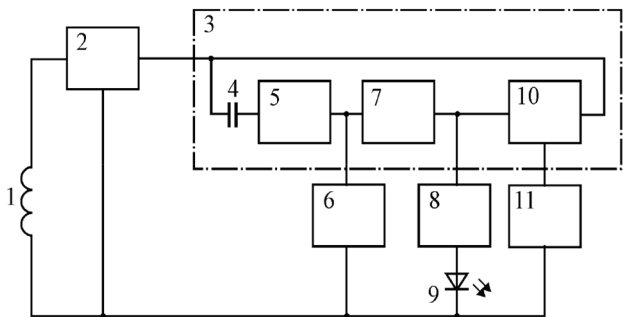


**Figure 9.** Block-diagram of ECFD with improved SORC

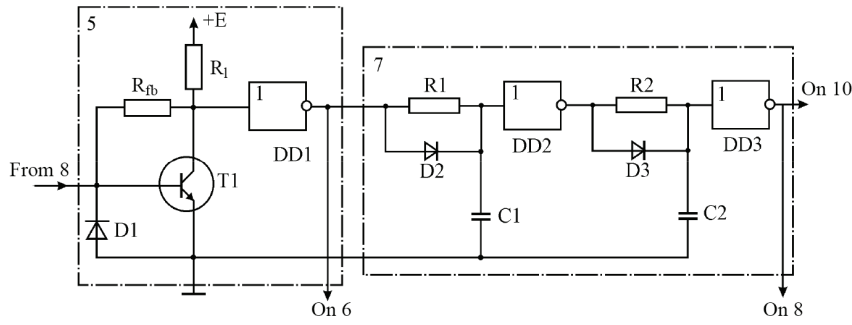


**Figure 10.** Circuit of limiting amplifier and defect signal former of SORC: D1 — diode;  $R_{fb}$  — feedback resistor; R1, R2, C1, C2, D2 and D3 — integrating diode circuits; DD1, DD2, DD3 — inverters

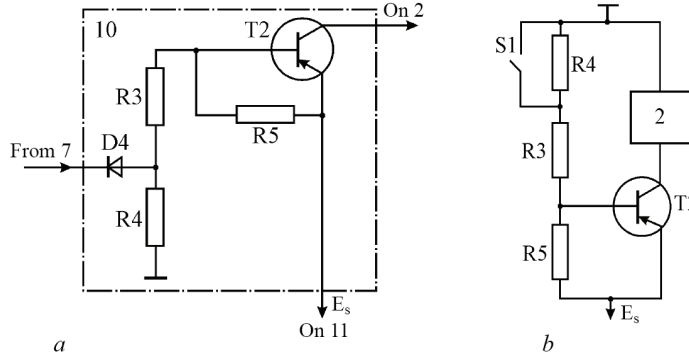


**Figure 11.** Circuit of supply voltage control (a) and its equivalent circuit (b): D4 — switching diode; R3 and R5 — supports of base voltage divider; T2 — transistor current regulator; 2 — SG; S1 — switch

to pulse expander 8, which increase the pulse length until defect light indicator 9 lights up.

Operation of SORC elements was studied, recording the signals in different SORC elements with digital oscillograph of TDS 1012 type, fitted with expansion module TDS 2CMA (see Figures 12, 13). Division value along the vertical is 1 V, along the horizontal it is 2.5 ms. In addition, the parameters of individual SORC elements are calculated below.

Limiting amplifier 5 (Figures 9, 10) is based on transistor T1, which is connected into a circuit with a common emitter with negative voltage feedback through feedback resistor  $R_{fb}$ . Isolation capacitor 4 (Figure 9) passes only the variable component of SG output voltage to the base of transistor T1. Diode D1 eliminates negative halfwave of input signal and binds it to logic zero level. Figure 12, a, b shows signals at SG output (before capacitor 4), and Figure 12, c, d — signals at the base of transistor T1 of limiting amplifier 5 in the absence of a defect and at ECP location on the defect, respectively. When ECP is located outside the defect (Figure 12, a), stable oscillations of 1 kHz frequency and amplitude close to 1 V are observed at SG output together with the constant component of supply voltage of 6 V. When the converter is positioned on the defect (Figure 12, b), suppression of oscillations is observed. Oscillatory process fades away because of the low  $Q$ -factor of ECP working loop when it is located on the defect, and supply voltage

decreases to the ground level, due to increase in SG current consumption. It leads to repeated suppression of generation, which is indicated by signal skip areas in Figure 12, b, d. While ECP is on the defect, this process is repeated with a frequency close to 100 Hz. A variable useful signal without the constant component remains after the capacitor (Figure 12, c, d), which carries information about ECP position on the surface of TE or about the defect. Transistor T1 of  $n-p-n$  type operates in the key mode and it is controlled by a signal of positive polarity: in the absence of the signal the transistor is closed, current is absent and supply voltage of 6 V is set on the collector. Amplified signal at the collector of transistor T1 (Figure 12, e, f) is limited from below by ground potential level, and from above — by the supply voltage. Time lapses in Figure 12, f, in which there is no signal, are indicative of ECP being on the defect. Transistor T1 should amplify the minimum value of SG output signal to the level of supply voltage  $E_s$ , i.e. ensure the level of logical unit with an excess. Minimum output voltage  $U_{min}$  is equal to approximately 0.2 V, and the supply voltage level is 6 V. Hence, the gain of limiting amplifier should correspond to the condition of  $K \geq E_s/U_{min} = 30$ . For the selected maximum collector current of the transistor  $I_c = 0.4$  mA, the load resistance will be  $R_l = E_s/I_c = 15$  kOhm. As amplification coefficient is equal to ratio  $K = R_{fb}/R_l$ , then to ensure the required amplification, feedback resistance  $R_{fb}$  was selected greater



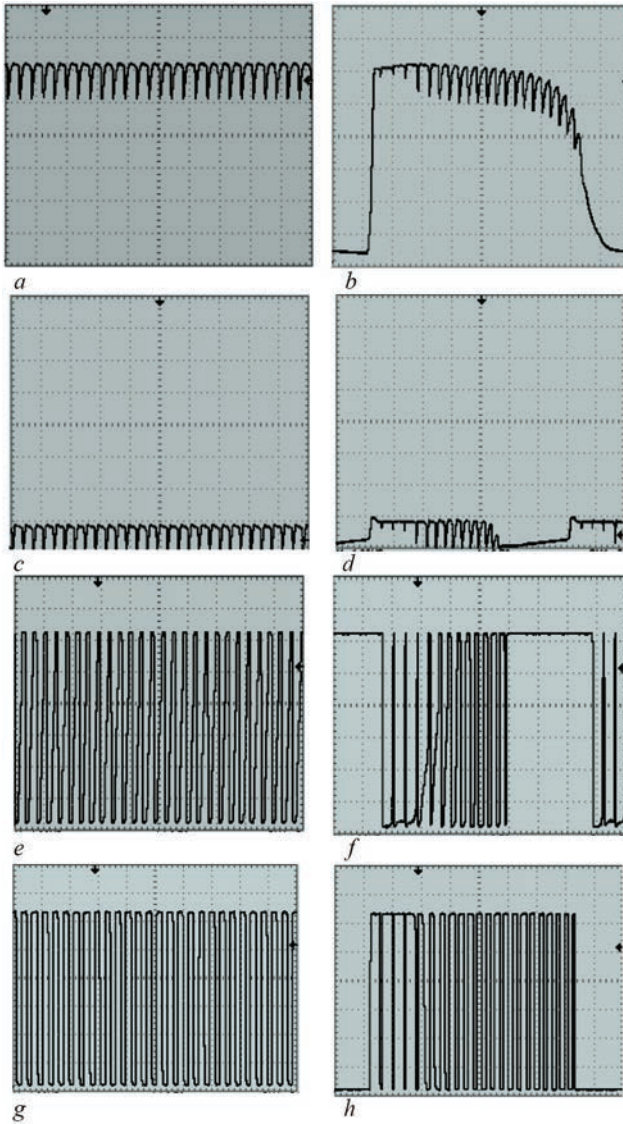


**Figure 12.** SORC signals in the absence of defect (left) and when ECP is placed on the defect (right): *a, b* — at SORC input; *c, d* — at T1 transistor base; *e, f* — at inverter input; *g, h* — at DD1 inverter output (Figure 10)

than 450 kOhm. Output signal of logic inverter DD1 forms change-tonal information about the defect and ECP position on TO surface, and comes to sound indication block 6, which consists of low-frequency amplifier and operator headphones. DD1 logic inverter performs signal inversion and additionally amplifies them to the level of supply voltage to improve the rectangular shape of the signal (Figure 12, *g, h*). DD1 logic inverter was built using MC 14069 UDP micro-circuit of Motorola Company, which has 6 separate inverters, which are also used for other SORC elements. Circuit parameters are as follows: logic zero output level  $\leq 1\% E_s$ , logic unit output level —  $9.95\% E_s$ , logic zero input level  $\leq 20\% E_s$ , logic unit input level  $\geq 80\% E_s$ . Supply voltage  $E_s$  can be selected in the range of 3–18 V.

Sound frequency signal from DD1 inverter output comes to signal former, which, in order to sharpen the

defect signal pulse, is made in the form of two integrating circuits R1–C1–D2 and R2–C2–D3, connected in series, with DD2 and DD3 inverters (Figure 10). The time constant  $\tau = R \cdot C$  of integrating circuits is selected to be such as to smooth the signal of sound frequency of 1–3 kHz, which corresponds to TO defect-free region. The integrating circuit plays the role of a filter to suppress the signal. Therefore, we define the attenuation factor as equal to  $k_{att} = U_{in}/U_{out} \geq \geq 100$ . Hence, the parameters of equivalent scheme of integrating circuit are defined by the following relationship ( $R + X_c/X_c \geq 100$  or  $R \geq 99X_c$ , where  $R$  and  $X_c$  are the resistance and reactance of the resistor and capacitor of integrating circuits (Figure 10). Capacitor capacitance was selected equal to 47 nF. Then, reactance  $X_c = 3390$  Ohm for the lowest signal frequency (1 kHz) to be suppressed. Hence, resistor resistance  $R$  should be selected greater than  $X_c = 3390$  Ohm.

In Figure 12, *a* the remains of the sound signal of approximately 1 kHz frequency are observed on the level of logic unit, which disappear after the next integrating circuits (Figure 13, *c, e, g*), and the signal in the defect-free area is smoothed. Here, the integrating circuits pass the low-frequency signal with repetition rate of pulse series close to 100 Hz, which correspond to periodical suppression of SG oscillations at ECP positioned on the defect. DD2 and DD3 inverters are used to form a short pulse (Figure 13, *h*) with steep fronts for starting the supply voltage control circuit, which also comes to pulse expander 8 (Figure 9) to form the pulse, designed for light diode operation. In Figure 13, *b* the start of formation of the pulsed signal from the defect is observed in the absence of intermittent generation, when ECP is located on the defect. Signal amplitude in  $t_2 - t_3$  time range decreases by the following exponential law  $U(t) = E_s e^{-t/\tau}$ , where  $U(t)$  is the voltage at moment of time  $t$ . Steep fronts of pulsed signal from the defect are reached by adding D2 diode, through which fast charging of C1 capacitor takes place at moment of time  $t_1$ . C1 capacitor discharges slowly through R1 resistor. Further forming of defect signal occurs similarly in the other R2C2 integrating circuit and DD3 inverter. In TO defect-free area a line is observed at logic zero level at the output of integrating circuit R2C2 (Figure 13, *e*). On the defect (Figure 13, *f*) the signal at the output of R2C2 integrating circuit increases abruptly due to C2 capacitor charging through D2 diode and decreases slowly by exponential law through its discharging to R2 resistor. A short negative pulse with steep fronts of approximately 2.5 ms duration signaling about the defect, forms at the output of DD3 inverter (Figure 13, *h*). In the absence of the defect, the signal at the output of DD3 logic inverter has only a constant component

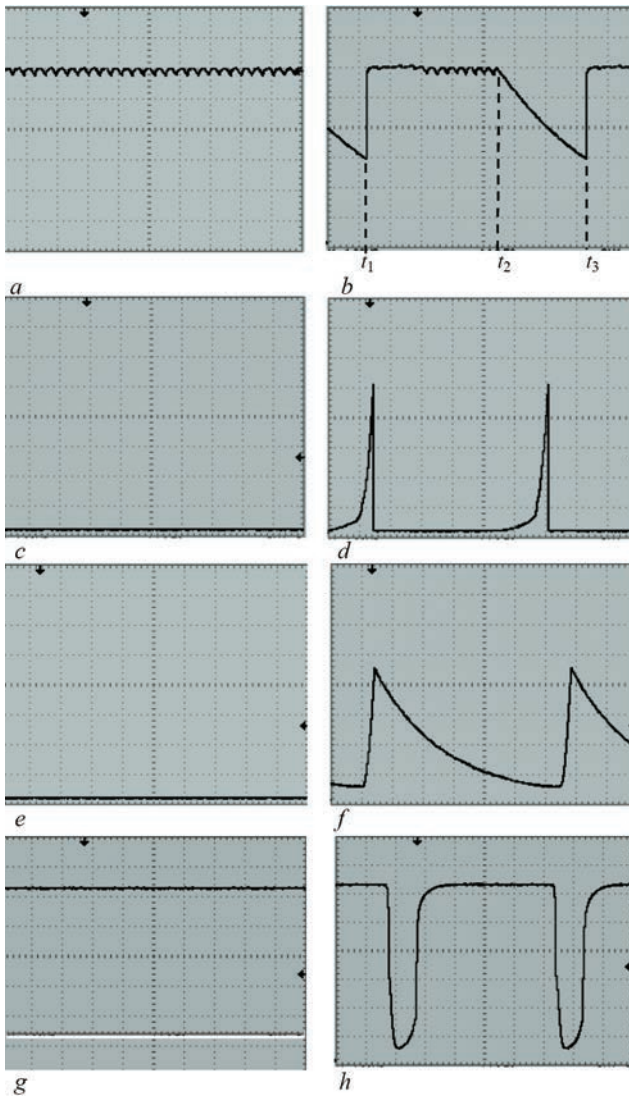


**Figure 13.** SORC signals in the absence of defects (left) and when ECP is placed on the defect (right): *a, b* — at DD2 inverter input; *c, d* — at DD2 inverter output; *e, f* — at DD3 inverter input; *g, h* — DD3 inverter output

at the level of logic unit (Figure 13, *g*). The signal from the defect (Figure 13, *h*) comes to SG supply voltage control circuit, which is a controlled current source based on T2 transistor of *p-n-p* type, connected in a circuit with a common emitter (Figure 13, *a*). In the equivalent circuit (Figure 13, *b*) electronic switch based on D4 diode is replaced by S1 switch. Supply voltage  $E_s$  is divided into collector-emitter voltage  $U_{ce}$  of T2 transistor and SG voltage  $U_{SG}$   $E_s = U_{SG} + U_{ce}$ . R3, R4 and R5 supports are part of base voltage of T2 transistor and determine its current according to  $I = E_s / (R_3 + R_4 + R_5)$  ratio. In its turn, the change of base current influences the collector current of T2 transistor, which passes through SG 2 active element. At generation suppression on the defect, a pulse forms at the output of former 7 (DD3 inverter). This pulse shorts the cathode of D4 diode to the ground for 2.5 ms, and reduces the influence of R4 resistor due to shunting. In the equivalent circuit it is modeled

by shorting S1 switch to the ground. Here, base-emitter voltage  $U_{be}$  of T2 transistor increases, reducing the equivalent resistance of T2 transistor and its  $U_{ce}$  voltage. The voltage in SG active element increases due to redistribution of stabilized voltage, leading to resumption of its generation.

The advantage of the proposed SORC consists in that, in addition to fast resumption of SG oscillations after their suppression, it also ensures convenient connection of the sound and light indicators and use of integral CMOS of logic inverters with low current consumption ( $1.5 \cdot 10^{-6}$  A) and low supply voltage.

## CONCLUSIONS

SG scheme circuit with double-circuit oscillatory system, operating in intermittent generation mode, is promising for development of self-generator ECFD. New engineering solutions were proposed and studied, in particular SG circuit based on a field transistor with an insulated gate, circuit of generation frequency control and circuit of SG oscillation regeneration. Their advantages concerned with sensitivity are shown, compared to traditional schemes. The analyzed engineering solutions were used to develop self-generator ECFD of VD 3.03N, VD 3.02N, VD 4.01N and VD 4.03N type to reveal surface cracks, which have passed state testing, and have been entered into the State Register of measuring equipment. They are used for maintenance of aircraft of SC “Antonov” and aircraft engines of SC “Ivchenko-Progress”, as well as PJSC “Motor-Sich”. The instruments have also been implemented in “International Airlines of Ukraine” Company, in Lviv and Konotop Aircraft Repair Enterprises, HPU “Lvivhasvydobyvannya”, SPC “Zond”, PJSC “Zakhidenergo”, Karpaty and Poltava ETC, etc.

Practical experience of NDT using the developed ECFD confirmed the effectiveness of engineering solutions, presented in this paper. It is envisaged to apply them in the new intellectual self-generator ECFD, which will additionally have automatic adjustment to the sensitivity level, assigned by the testing procedure and indication of sensitivity level.

The paper is devoted to the bright memory of Vsevolod Vadymovych Cherlenskyi, talented engineer, who directly participated in finding some of the engineering solutions and performing part of the measurements.

## REFERENCES

1. Dorofeev, A.L., Kazamanov, Yu.G. (1980) *Electromagnetic flaw detection*. Moscow, Mashinostroenie [in Russian].
2. Gerasimov, V.G., Pokrovsky, A.D., Sukhorukov, V.V. (1992) *Non-destructive testing*. In: 5 Books. Book 3: Electromagnetic testing. Moscow, Vysshaya Shkola [in Russian].
3. Bilik, Yu.Z., Dorofeev, A.L. (1981) Electromagnetic flaw detectors of «Proba» type. *Defektoskopiya*, **6**, 53–58 [in Russian].

4. (1989) *Eddy current flaw detector of TVD-A type. Technical description and operating instruction*. Moscow, Ministry of Civil Aviation [in Russian].
5. Arsh, E.I., Tverdostup, N.I., Khandetsky, V.S. (1981) Features of construction of self-oscillating meters on lambda-diodes. *Izmeritelnaya Tekhnika*, **1**, 53–55 [in Russian].
6. Alekseev, A.P., Sajmanin, A.E., Shaternikov, V.E. (1989) Problems of automatic design of eddy current self-oscillating flaw detectors built on lambda-diodes. *Defektoskopiya*, **12**, 51–55 [in Russian].
7. Serebrennikov, S.V., Khandetsky, V.S. (1983) *Comparative examination of metrological characteristics of self-oscillating transducers with different turn on the circuit*. In book: Instrument-making industry. Issue 34. Kyiv, Tekhnika, 35–38 [in Russian].
8. Arsh, E.I. (1976) *Self-oscillating measurements*. Moscow, Energiya [in Russian].
9. Gonorovskiy, I.S. (1977) *Radio circuits and signals*. 3<sup>rd</sup> Ed., Moscow, Sov. Radio [in Russian].
10. Uchanin, V.N. (2010) Self-oscillating eddy current flaw detectors: Main principles, classification, comparative analysis (Review). *Tech. Diagnost. and Non-Destructive Testing*, **2**, 18–23 [in Russian].
11. Uchanin, V. (2021) Enhanced eddy current techniques for detection of surface-breaking cracks in aircraft structures. *Transact. on Aerospace Research*, 262(1), 1–14. DOI: <https://doi.org/10.2478/tar-2021-0001>
12. (2002) *Distinguished Service Order of series TDS1000 and TDS2000. User manual*. USA, Tektronix Inc.
13. Shitikov, G.T. (1983) *Stable self-oscillators of meter and decimeter waves*. Moscow, Radio i Sviaz [in Russian].
14. Lenk, D. (1979) *Handbook on design of electronic circuits*. Kyiv, Tekhnika [in Russian].
15. Uchanin, V.M. (2022) Optimization of the design of eddy current probe of parametric type to detect surface cracks. *Tekh. Diahnost. ta Neruiniv. Kontrol*, **1**, 11–21 [in Ukrainian]. DOI: <https://doi.org/10.37434/tdnk2022.01.01>

#### ORCID

V.M. Uchanin: 0000-0001-9664-2101

#### CORRESPONDING AUTHOR

V.M. Uchanin

G.V. Karpenko Physico-Mechanical Institute  
of NASU

5 Naukova Str., 79060, Lviv, Ukraine.

E-mail: [vuchanin@gmail.com](mailto:vuchanin@gmail.com)

#### SUGGESTED CITATION

V.M. Uchanin (2022) Study of eddy current flaw detector based on double-circuit self-generator operated in intermittent oscillating mode. *The Paton Welding J.*, **5**, 46–56.

#### JOURNAL HOME PAGE

<https://pwj.com.ua/en>

Received: 27.03.2022

Accepted: 08.08.2022